ODESSA ASTRONOMICAL PUBLICATIONS

Volume 27 Issue 2
(2014)
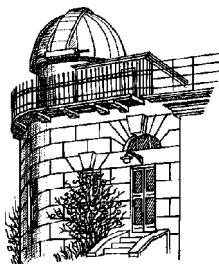
CONTENTS

THE SIMULATION OF THE ORBITAL EVOLUTION OF A PASSIVE HIGH-ORBIT FRAGMENT WITH LARGE SURFACE AREA

A.A.Bazyey

Astronomical Observatory, Odessa National University,
Shevchenko Park, Odessa 65014, Ukraine

ABSTRACT. The numerical integration of the motion equations of a passive high-orbit fragment with large surface area was performed accounting for the main gravitational perturbations of the Earth, Moon and Sun, as well as the solar radiation pressure.

Based on the numerical model of motion in the near-Earth space that accounts for only the most powerful perturbations, a new method for de-orbiting artificial celestial bodies from high altitudes is suggested.

Key words: methods: numerical – celestial mechanics.

1. Introduction

Today there are tens of thousands of artificial celestial bodies in the near-Earth space. Most of them belong to the space debris as such worn-out artificial satellites or their fragments. Such celestial bodies can remain in high orbits essentially indefinitely. Their motion is subjected to the perturbations by the Moon and Sun, as well as by the asymmetry of the Earth's gravitational field. The high-orbit objects are monitored using optical telescopes.

This paper describes a new method for de-orbiting of worn-out artificial satellites from the geostationary orbits in the near-Earth space to lower altitudes.

2. Observations

We selected fragment 43096, which was detected with the ESA Space Debris 1-m Telescope located on the island of Tenerife, Spain, by Thomas Schildknecht's team during their cooperation with the ISON project (Volvach et al., 2006). The fragment's reference corresponds to the number in the Keldysh Institute of Applied Mathematics of the Russian Academy of Sciences database. This fragment is interesting by its high area-to-mass ratio (HAMR). When describing changes in its orbiting, it is necessary to account for significant perturbations due to the radiation pressure in addition to those by gravity. Perturbations due to the solar radiation pressure tend to be periodic. We processed observation data for the indicated fragment, which had been obtained by the ISON network during 2006-2012 within the framework of the Pulkovo Cooperation of Optical Observers (PulCOO) programme.

3. Results

A total of 226 series of observations conducted from 18 November 2006 to 16 June 2012 were processed. Each series averaged to 20-30 measurements of the topocentric right ascensions, declinations and UTC time references. The Keplerian elements were determined for each series by Laplace's method with the subsequent refining by the 6-parameter iteration method. The accuracy of the orbital elements was estimated using the residual errors representing differences of the observed positions of the fragment from the predicted ones. The computation procedure is specified in Bazyey et al. (2005) and Escobal (1970). The least errors in orbital element determination were obtained for the following series of observations:

24 November 2006 01:09:56.87 (Tenerife)

$p = (6.4666 \pm 0.0002)$ equatorial radius

$e = (0.06681 \pm 0.00002)$

$\omega = (261.16 \pm 0.02)°$

$\Pi = (321.588 \pm 0.002)°$

$i = (9.0212 \pm 0.0003)°$

$M_0 = (242.48 \pm 0.03)°$.

The state vector was determined as of 24 November 2006 01:55:50.76 UTC:

$x = -2.28181$ equatorial radius

$y = 6.21066$ equatorial radius

$z = 0.54755$ equatorial radius

$Vx = -0.0259860$ equatorial radius per minute

$Vy = -0.0111238$ equatorial radius per minute

$Vz = -0.00394734$ equatorial radius per minute.

The indicated values were assumed to be the initial conditions for the fragment's orbit integration. The

area-to-mass ratio was assumed equal to $\frac{S}{m} = 2.56$ sq.m/kg (Früh & Schildknecht, 2011). The acceleration due to the direct solar radiation was estimated as follows:

$$a = C\frac{S}{m}\left(\frac{r}{r_0}\right)\frac{r - r_S}{r}$$

with $C = P_0(1 + A)$, $P_0 = 0.0000045606$ N/sq.m the solar radiation pressure at the Earth's orbit, A – the electro-magnetic radiation reflection coefficient $(0 < A < 1)$, r_0 the average radius of the Earth's orbit, r and r_S – the fragment's and the Sun's positions in the Earth-centered coordinate system.

As fragment 43096 is referred as a high-orbit artificial Earth's satellites, the perturbations of its motion due to the Moon and Sun are comparable to those by the Earth's flattening (Borodovitsyna & Avdyushev, 2007). We accounted for the perturbations by the second zonal harmonic of the Earth's gravitational field, the Moon and Sun, as well as the solar radiation pressure. The integration was performed by the Runge-Kutta methods of the 10th order (Bazyey & Kara, 2005).

During the whole period the orbit's semi-major axis has not been subjected to the secular perturbations. The eccentricity and argument of perigee are exposed to the periodic perturbations with duration of some 370 days. The eccentricity varies from 0.017 to 0.071. The apse line oscillates with an amplitude of about 80° and slowly rotates with the angular velocity of 0.020°/day. The longitude of the ascending node and inclination of the orbit decrease at the rate of 0.0028°/day and 0.0016°/day, respectively, within the whole observation interval.

Therefore, the 43096 fragment orbit periodically changes the shape and position of the apse line, leaving its size unaltered. Besides, the apse line, longitude of the ascending node and inclination change monotonically. The numerical integration shows that the periodic perturbations in the eccentricity and argument of perigee are due to the solar radiation pressure: assuming $P_0 = 0$, those perturbations disappear.

That fact can be used to purposely change orbits of the geostationary objects and their de-orbiting to lower altitudes as down as the Earth's atmosphere.

Let us explain that by exemplifying simulation of the 43096 fragment motion. Using the eccentricity variation curve, it is easy to detect that the eccentricity was increasing from 05 May 2007 to 13 November 2007, from 08 May 2008 to 19 November 2008, from 15 May 2009 to 26 November 2009, from 22 May 2010 to 03 December 2010, and from 29 May 2011 to 04 December 2011. During those periods the perigee distance decreases due to the radiation pressure with the semi-major axis remaining altered. The eccentricity was decreasing from 13 November 2007 to 08 May 2008, from
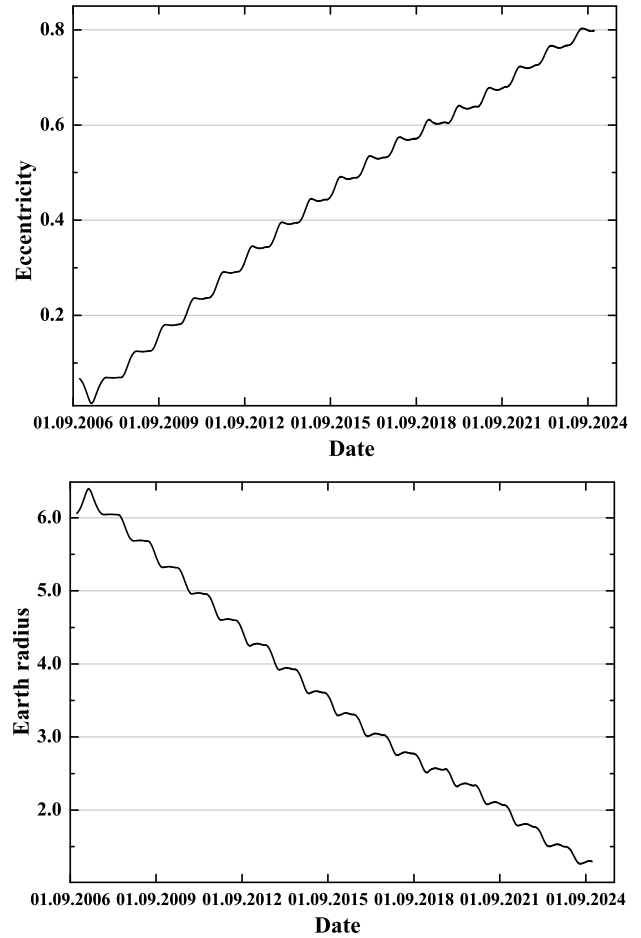
Figure 1: The change in the orbital elements of the celestial body (eccentricity and semi-major axis) subjected to the alternating radiation pressure

19 November 2008 to 15 May 2009, from 26 November 2009 to 22 May 2010 and from 03 December 2010 to 29 May 2011. If the solar radiation pressure force is stronger while the eccentricity increases comparing to those time intervals when it decreases, then it is possible to determine general secular increase of the orbital eccentricity. The same effect can be reached, for instance, by increasing the area-to mass ratio of the fragment while the eccentricity increases. We conducted the numerical experiment on the simulation of the 43096 fragment orbit with the same initial conditions as of 24 November 2006 01:55:50.76 UTC, but with alternating radiation pressure. It was assumed that $P_0 = 0.0000045606$ N/sq.m for the increasing eccentricity and $P_0 = 0$ for the decreasing eccentricity. The result is shown in Figure 1. The eccentricity increased from 0.02 as of 08 May 2007 to 0.30 as of 31 July 2012. And the semi-major axis remained unaltered at that. At the end of the integration interval the perigee distance decreased down to 29000 km (the Earth's equatorial radius 4.54). Such a considerable

change in the fragment's orbit was successfully attained just by changing the solar radiation pressure force two times per year.

Colligating the result obtained, it should be noted that such a method of changing the celestial body orbit in the near-Earth space can be applied to solve problems of the near-space ecology. Provided the capabilities to control the changes in the area-to-mass ratios of worn-out satellites, it is possible to solve the problem of cleaning up the near-Earth space from the space debris of artificial origin using the solar radiation pressure exclusively.

Based on the numerical model of motion in the near-Earth space that accounts for only the most powerful perturbations, a new method for de-orbiting artificial celestial bodies from high altitudes is suggested.

Conclusion

For the first time such a considerable amount of data over long time intervals was gathered for the objects with high area-to-mass ratios that enabled us to determine and estimate their observation and orbital characteristics.

The method of the celestial body orbit changing in the near-Earth space which is described in this paper can be useful in solution of the near-space ecology problem, particularly in the cleaning up the near-Earth space from the artificial space debris using the solar radiation pressure only.

References

Bazyey A.A., Kara I.V.: 2005, *Odessa Astron. Publ.*, **18**, 14.

Borodovitsyna T.V., Avdyushev V.A.: 2007, *The Theory of the Earth's Artificial Satellites' Motion. Analytic and Numerical Methods.* Tomsk University Publishing House (in Russian).

Escobal P.: 1970, *Methods of Orbit Determination*, Moscow: Mir (in Russian).

Früh C., Schildknecht T.: 2011, *Mon. Not. R. Astron. Soc.*, **419**, 3521.

Volvach A.E., Roumyantsev V.V., Molotov I.E. et al.: 2006, *Space Science and Technology*, **12**, No. 5/6, 50.

THE STUDY OF GALACTIC BEAT CEPHEIDS WITH APPLICATION OF ITS RESULTS TO THOSE IN THE MAGELLANIC CLOUDS

F. A. Chekhonadskikh, V. V. Kovtyukh, S. I. Belik

Astronomical observatory of Odessa National University,
Odessa, Ukraine, *chehonadskih@gmail.com*

ABSTRACT. A thorough study of the correlation between P_1/P_0 ratio, fundamental period, and chemical composition (abundances of metals that compose Z) was conducted to investigate the significance of the iron-peak elements on the ratio. The results suggested a more accurate P_1/P_0 ratio that can be useful as an alternative means of determining a beat Cepheid's metallicity. Metallicities for a large sample of stars were analysed using the suggested ratio. The metallicity distribution function for the Magellanic Clouds projected on the celestial sphere was constructed for the first time, and several stars with anomalous metallicities were detected. The average metallicities of the Magellanic Clouds were also obtained independently: –0.30 dex for the Large Magellanic Cloud (LMC) and –0.49 dex for the Small Magellanic Cloud (SMC). The [Fe/H] values for two newly-found bimodal Cepheids in the Galactic bulge were estimated: –0.39 dex for OGLE-BLG-CEP-03 and –0.29 dex for OGLE-BLG-CEP-21.

Key words: stars: Classical Cepheids – stars: abundance, metallicity

1. Introduction

In recent years the beat Cepheids have often been called double-mode Cepheids or bimodal Cepheids. They imply the same objects in any case: such Cepheids pulsate in two radial modes simultaneously. There can be different combinations of two pulsation modes for a bimodal Cepheid, as implied by their period ratios, such as first overtone and fundamental mode (P_1/P_0), or second and first overtone modes (P_2/P_1), or even third and first overtone modes (P_3/P_1). Exotic Cepheids implied by the last type were found only in other galaxies, such as the huge number discovered in the OGLE project surveys (see Udalski et al., 2008). There is a small sample of bimodal Cepheids in our Galaxy, their total number does not exceed 25 and the majority of them are P_1/P_0 pulsators.

It is well-known that the P_1/P_0 period ratio for bimodal Cepheids strongly depends on the physical parameters of the stars, such as mass (M), luminosity (L), mean effective temperature (T_{eff}), and metallicity (Z). The metallicity Z is an additive measure comprised of all elements heavier than helium. But it is not yet known which elements have greater significance with regard to P_1/P_0 ratio.

According to some theoretical studies we might assume that such elements could be the iron-peak elements, some researchers have suggested the importance of the P_1/P_0–[Fe/H] relation (see Sziládi et al., 2007). To date it has not been possible to carry out an in-depth statistical analysis regarding the influence of other elements on the indicated relationship. The results of such an analysis are presented here. We expanded the applicability of the suggested relation through our sample of beat Cepheids enlarged by the addition of the metal-deficient Cepheid V371 Per. It enabled us to conduct an in-depth study of the metallicity distribution in the Magellanic Clouds where metallicities are lower than in our Galaxy.

2. The spectral material

High signal-to-noise spectra were obtained using the 2.2-m MPG telescope and FEROS spectrograph at ESO La Silla (Chile). The spectra cover a continuous wavelength range from 4000 to 7850 Å with a resolving power of about 48 000. Typical maximum S/N values (per pixel) for the spectra exceeded 150 (see Table 1).

A broad-lined B-star with a S/N ratio exceeding that of the program stars was observed nightly to make the telluric line cancellation possible when necessary. Table 2 also contains some details of the program Cepheid observations. Previously, the spectra were used only to determine the [Fe/H] abundance (Sziládi et al. 2007).

Further processing, such as continuum placement, line depth and equivalent width (R_λ and EW) calculations were carried out using the DECH20 software

Table 1: Atmospheric parameters of the program stars

Star	MJD	S/N	T_{eff} (K)	$\log g$ (dex)	V_t (km s^{-1})
Y Car	53155.953274	187	5890	2.2	3.0
	53158.133919	270	6564	2.0	3.7
GZ Car	53158.077868	125	5904	2.1	4.4
EY Car	53156.081982	142	6000	2.6	4.5
	53158.051978	139	5855	2.1	3.6
V701 Car	53156.031049	169	5755	2.0	3.0
BK Cen	53156.135605	201	5866	2.2	3.8
	53158.211729	151	5830	2.1	3.1
UZ Cen	53156.163756	210	6307	2.3	4.0
	53158.154992	168	5809	2.1	3.5
V1210 Cen	53158.181235	274	5868	2.1	4.2
VX Pup	53157.943348	274	6415	2.6	3.8
EW Sct	53156.311619	150	5668	1.9	3.7
	53157.437109	197	5985	2.2	4.6
	53158.416900	228	6383	2.4	4.3
V367 Sct	53156.358955	151	6111	2.3	4.7
	53157.387011	146	6212	2.2	4.8
V458 Sct	53156.258363	218	6160	2.2	4.5
	53157.311805	183	5984	2.0	3.5
BQ Ser	53156.285838	133	5835	2.0	3.8
	53157.412207	139	6210	2.1	3.9
	53158.389508	169	6143	2.2	4.0
U TrA	53156.229253	300	5909	2.1	3.8
	53158.290333	270	6054	2.4	3.8
AP Vel	53155.970338	126	5855	2.1	4.0
	53158.010053	154	5970	2.4	4.0
AX Vel	53155.993418	328	6241	2.3	3.5
	53158.035784	232	6205	2.1	3.6

Table 2: The Galactic beat Cepheids parameters

Star	Sp	P_1/P_0	[Fe/H] (dex)	R_G (kpc)
Y Car	1	0.7032	0.02	7.67
EY Car	2	0.7079	0.07	7.52
GZ Car	1	0.7054	0.00	7.63
V701 Car	2	0.7017	0.07	7.72
TU Cas	12	0.7097	0.03	8.31
UZ Cen	2	0.7064	−0.02	7.45
BK Cen	2	0.7004	0.12	7.24
1210 Cen	1	0.7035	0.08	6.39
V371 Per	2	0.7312	−0.42	10.61
VX Pup	2	0.7104	−0.06	8.64
EW Sct	6	0.6986	0.04	7.57
V367 Sct	3	0.6968	0.05	6.43
V458 Sct	2	0.6993	0.09	6.92
BQ Ser	6	0.7052	−0.04	7.17
U TrA	2	0.7105	−0.07	7.14
AP Vel	2	0.7033	0.06	8.24
AX Vel	3	0.7059	−0.05	8.11

Remarks: Sp – number of used spectra;

R_G – Galactocentric distance ($R_{G,\odot} = 7.9$ kpc)

package by Galazutdinov (1992). The EWs were measured by the Gaussian fitting.

3.   Fundamental parameters and chemical composition

To determine the effective temperatures (T_{eff}) for our stars, we employed the line-depth ratio method developed by Kovtyukh (2007). The technique enabled us to determine T_{eff} with an exceptional accuracy. It is based on the ratio of the central depths of two lines that differ markedly in their functional dependence on T_{eff} (and there are a few tens of line pairs that were used in the analysis). The method is independent of interstellar reddening and just marginally dependent on individual characteristics of the stars, such as rotation, microturbulence, metallicity, etc. With ∼50–70 calibrations per spectrum the uncertainty was 10–20K for spectra with S/N ratio greater than 100 and 30–50 K for those with S/N ratio less than 100.

To determine the microturbulent velocities (V_t) and gravities ($\log g$), we used a modified method of standard analysis proposed by Kovtyukh & Andrievsky (1999). The method implies that V_t is determined from the Fe II lines (instead of the Fe I lines used in classical abundance analyses). The value of $\log g$ is determined by forcing the equality of the total iron abundance derived from the Fe I and Fe II lines. Normally, the iron abundance determined from the Fe I line using this method appears to exhibit a strong dependence on EW (because of non-LTE effects). In that case, the abundance extrapolated to zero EW is considered to be the true value.

The physical parameters of the program stars are presented in Table 1. The elemental abundances were computed using the Kurucz WIDTH9 code. As usual, the abundance values are given relative to the solar values, which were adopted from Grevesse et al. (1996). Moreover, we used the chemical composition determined for V371 Per by Kovtyukh et al. (2012) and for TU Cas by Andryevsky et al. (2002); we also used abundances determined from additional spectra of EW Sct and BQ Ser. The combined data are given in Tables 2 and 3.

4. Correlation analysis of Z components

As there was a sample of 17 program stars available, we could only identify the impact of 15 external factors from regression analysis. As ensues from observations, the P_1/P_0 ratio depends on the fundamental period P_0 itself. In addition, we attempted to separate the effects of metallicity and accounted for that in the relation. From such considerations we constructed the relationship as a linear model that, apart from period P_0, contains abundances of 14 chemical elements found in stellar atmospheres. There were several α-elements, the iron-peak and other elements, for which A(El) > 7 dex. Regression and correlation analyses for the constructed model were carried out, and quite predictable results were obtained.

Oxygen is the most common element after hydrogen and helium. The oxygen abundance in stellar atmospheres A(O) exceeds 8 dex and tends to 9 dex. Values around 7.5 dex are typical for nitrogen, carbon, most

Table 3: Chemical composition of the program stars

Star	C	N	O	Na	Mg	Al	Si	S	Ca	Sc	Ti	V	Cr	Mn
V371 Per	−0.32	−0.21	−0.18	−0.45	−0.43	−0.28	−0.28	−0.13	−0.25	−0.17	−0.07	−0.18	−0.42	−0.41
TU Cas	−0.19	...	−0.03	0.15	−0.19	0.14	0.10	−0.03	−0.02	−0.19	0.05	0.02	0.02	0.06
U TrA	−0.29	0.33	−0.03	0.05	−0.19	0.09	−0.02	0.01	−0.12	−0.10	−0.02	−0.12	−0.15	−0.25
EY Car	−0.26	0.38	0.16	0.06	−0.05	0.31	0.08	0.17	−0.01	0.05	0.04	0.07	0.02	0.01
VX Pup	−0.30	0.20	−0.06	−0.06	−0.22	−0.09	−0.12	0.00	−0.15	−0.15	−0.07	−0.09	−0.10	−0.25
AP Vel	−0.11	0.45	0.11	0.12	−0.03	0.31	0.08	0.19	−0.03	0.04	0.04	−0.02	−0.03	−0.10
BK Cen	−0.09	...	0.08	0.27	−0.03	0.20	0.14	0.25	0.04	0.06	0.12	0.04	0.12	0.02
UZ Cen	−0.25	0.30	−0.04	0.16	−0.15	0.06	−0.01	0.02	−0.08	−0.05	−0.03	−0.16	−0.04	−0.20
Y Car	−0.18	0.25	0.01	0.12	−0.19	0.06	0.04	0.09	0.01	0.00	0.00	−0.07	−0.03	−0.19
AX Vel	−0.28	0.46	−0.06	0.09	−0.06	0.16	0.04	0.08	−0.04	−0.05	−0.04	−0.08	−0.08	−0.23
V701 Car	−0.06	0.36	0.02	0.30	−0.01	0.21	0.10	0.15	0.11	0.06	0.07	−0.02	0.07	−0.03
GZ Car	−0.12	...	−0.16	0.10	−0.13	0.08	0.01	0.11	−0.19	−0.08	0.03	−0.07	−0.11	−0.15
BQ Ser	−0.17	0.27	−0.13	0.10	−0.12	0.18	0.05	0.12	−0.04	−0.10	0.02	−0.03	−0.02	−0.10
V1210 Cen	0.09	0.17	0.13	0.03	−0.06	0.26	0.09	0.26	0.04	0.07	0.09	0.02	0.02	0.00
V458 Sct	−0.17	0.41	−0.01	0.25	−0.07	0.33	0.13	0.21	0.05	0.04	0.12	0.05	0.09	−0.02
EW Sct	−0.04	0.20	−0.01	0.02	−0.12	0.17	0.06	0.16	0.02	−0.05	0.06	0.03	0.04	−0.02
V367 Sct	0.02	0.60	0.06	0.22	0.02	0.34	0.09	0.24	−0.10	0.06	0.09	0.05	−0.02	−0.06

| Star	Fe	Co	Ni	Cu	Zn	Y	Zr	La	Ce	Pr	Nd	Sm	Eu	Gd
V371 Per	−0.42	−0.27	−0.34	−0.35	−0.08	0.03	−0.05	−0.02	0.03	−0.24	−0.22	...	0.01	...
TU Cas	0.03	−0.08	−0.04	0.15	0.46	0.17	0.01	0.24	−0.05	...	0.08	...	0.11	0.17
U TrA	−0.07	−0.17	−0.06	−0.06	−0.28	0.06	−0.02	0.09	−0.06	−0.09	−0.03	...	0.05	...
EY Car	0.07	0.14	0.06	0.21	−0.20	0.16	−0.10	0.17	...	...	0.12	...	−0.02	...
VX Pup	−0.06	−0.14	−0.11	−0.26	−0.36	0.02	−0.08	0.06	−0.03	−0.15	−0.12	0.18	0.03	...
AP Vel	0.06	−0.05	0.02	0.00	−0.20	0.17	...	0.17	0.01	...	0.10	...	0.12	...
BK Cen	0.12	0.03	0.10	0.09	−0.08	0.25	0.08	0.15	0.01	−0.09	0.12	...	0.18	...
UZ Cen	−0.02	−0.08	−0.07	−0.05	−0.22	0.10	−0.07	0.09	0.05	−0.06	−0.07	0.13	0.01	...
Y Car	0.02	−0.11	−0.02	−0.10	−0.30	0.17	0.08	0.09	0.10	−0.10	0.08	0.10	0.08	...
AX Vel	−0.05	−0.14	−0.11	0.05	−0.30	0.08	−0.25	0.13	0.04	−0.14	−0.02	...	−0.02	...
V701 Car	0.07	−0.06	0.08	−0.03	−0.10	0.23	0.10	0.01	0.11	−0.01	0.01	...	0.07	...
GZ Car	0.00	−0.11	−0.02	0.07	...	0.09	0.04	0.11	0.06	−0.25	−0.05	...	0.08	−0.05
BQ Ser	−0.04	−0.11	−0.04	0.06	−0.29	0.12	−0.10	0.20	−0.02	−0.34	0.12	0.27	0.10	0.20
V1210 Cen	0.08	−0.03	0.04	0.05	−0.17	0.25	0.01	0.18	0.02	−0.22	0.06	...	0.17	...
V458 Sct	0.09	0.09	0.11	0.13	−0.16	0.21	−0.13	0.17	0.03	−0.20	0.05	0.11	0.11	...
EW Sct	0.04	−0.07	0.00	0.04	−0.27	0.20	0.01	0.25	−0.02	−0.12	0.13	0.26	0.11	...
V367 Sct	0.05	−0.12	0.11	0.09	0.32	0.17	−0.07	0.17	0.00	−0.21	0.08	...	0.23	...
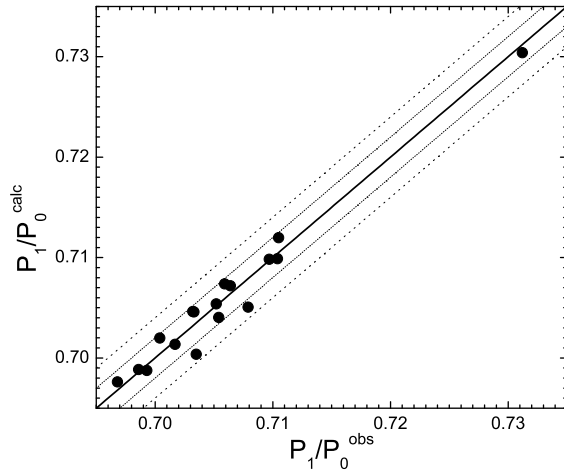
Figure 1: The comparison between the calculated P_1/P_0 ratios and P_1/P_0 ratios obtained from the observations. The ranges of error for σ and 2σ are marked with *dotted lines*.

of the α-elements, and the iron-peak elements. Though the abundances of oxygen and some other elements are about 9 dex, the iron-peak elements contribute most to the opacity.

It is known that the electron scattering plays an important role in the light energy absorption in the extended atmospheres of supergiants; therefore, the opacity depends on the electron density. The iron-peak elements, which are mainly in ionised form, supply free electrons. Thus, the period ratio P_1/P_0 tends to show greater sensitivity to the iron-peak elements, and lower or even zero sensitivity to other elements.

Our analysis of the final model has fully confirmed the validity of the initial assumptions. As expected, oxygen along with a number of other elements was not factored in the further analysis. Two α-elements, namely Ca and Si, showed a rather good correlation. But the greatest sensitivity of the relation was found for several iron-peak elements, such as Cr, Mn, Fe, Co and Ni. Given the crucial importance of the physical value, such as [Fe/H], we constructed an empirical relation for P_1/P_0, P_0 and [Fe/H]. The resulted relationship is as follows:

$$P_1/P_0 = 0.719 - 0.024 \, log \, P_0 - 0.041 \, [Fe/H]$$
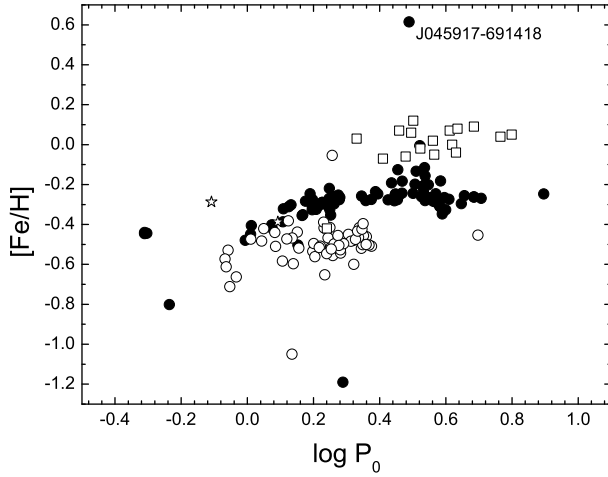$$\pm 0.002 \quad \pm 0.003 \qquad \pm 0.004.$$

Figure 2: Dependence of the [Fe/H] abundance on $log\ P_0$. *Open squares* – the Galactic beat Cepheids (program stars); *open stars* – the P_1/P_0 Cepheids of the Galactic bulge; *full circles* – the bimodal Cepheids of the LMC and *open circles* – those of the SMC.

Figure 3: Dependence [Fe/H] vs. P_1/P_0 ratio. Symbols are the same as in Fig. 2.

The results of a comparison of the calculated P_1/P_0 values with the data obtained from the photometric observations are presented in Fig. 1. The standard deviation is ± 0.002; the correlation coefficient R^2 is 0.97.

5. Confirmation and discussion

There are a small number of beat Cepheids in our Galaxy for a full confirmation of the derived relationship. The situation is better for the Magellanic Clouds. We have applied data from several sources: the EROS-2 database by Marquette et al. (2009), as well as the OGLE-III survey results by Soszyński et al. (2008) and Soszyński et al. (2010). It helped us to gather data for more than 90 beat Cepheids pulsating in the P_1/P_0 modes in the LMC and more than 60 in the SMC.

Using our relation, we estimated metallicities for the above-mentioned samples of stars. Figures 2 and 3 show the [Fe/H] sensitivity to $logP_0$ and P_1/P_0, respectively. As can be seen, there is a pronounced trend in Fig. 3. The Cepheid J045917-691418, whose data are shown in Fig. 3, drew our attention with its unusually high metallicity of 0.61 dex. Such a high value is anomalous not only for the Magellanic Clouds Cepheids, but also for Galactic pulsators.

According to modern theoretical calculations, the evolutionary tracks of high metallicity stars do not reach the instability strip. Therefore, based on theoretical models, it is possible to assume that Cepheids with such a high metallicity do not exist.

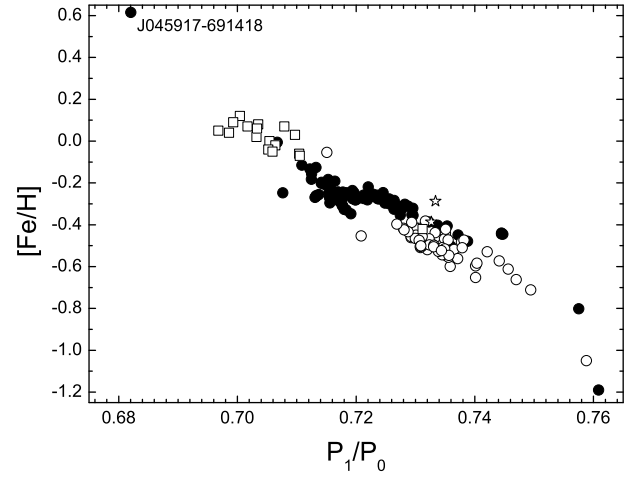To examine the case further, we focused our atten-

tion on the anomalous star. Such a subnormal value of P_1/P_0 for J045917-691418 was taken from the EROS-2 database. We searched for alternative data on that Cepheid and found an object with the same coordinates in the OGLE database. In the OGLE database that Cepheid was identified as a fundamental mode pulsator with a note that it might be a binary star with a first-overtone pulsator companion. That star should be restudied more thoroughly, but it requires new observations.

We can only assume that both study groups can be right in their definitions. The fact is that when a star reaches the instability strip, its mode of pulsation is quite unstable, and that can result in a very rapid change in pulsation periods. Since both the OGLE and EROS-2 observations are time-separated, it is likely that we face a similar situation. Thus, J045917-691418 is of great interest for further research.

We also constructed a metallicity distribution function for the Magellanic Clouds projected on the celestial sphere (see Fig. 4). A few regions with increased metallicity can be seen in the centre of the LMC projection. Although usually the distribution corresponds to the nature of irregular galaxies, no specific structures or formations are observed in the projection.

The average metallicities of the Magellanic Clouds were obtained independently: –0.30 dex for the LMC and –0.49 dex for the SMC. The average metallicity for the LMC is in good agreement with standard values obtained from spectral studies of B-supergiants or F-K supergiants. The average metallicity for the SMC is somewhat higher than common values obtained by other authors, but it is in very good agreement with the value obtained by Chekhonadskikh (2012) who used classical Cepheids in his study.

There were two double-mode P_1/P_0 Cepheids among a sample of new classical Cepheids discovered
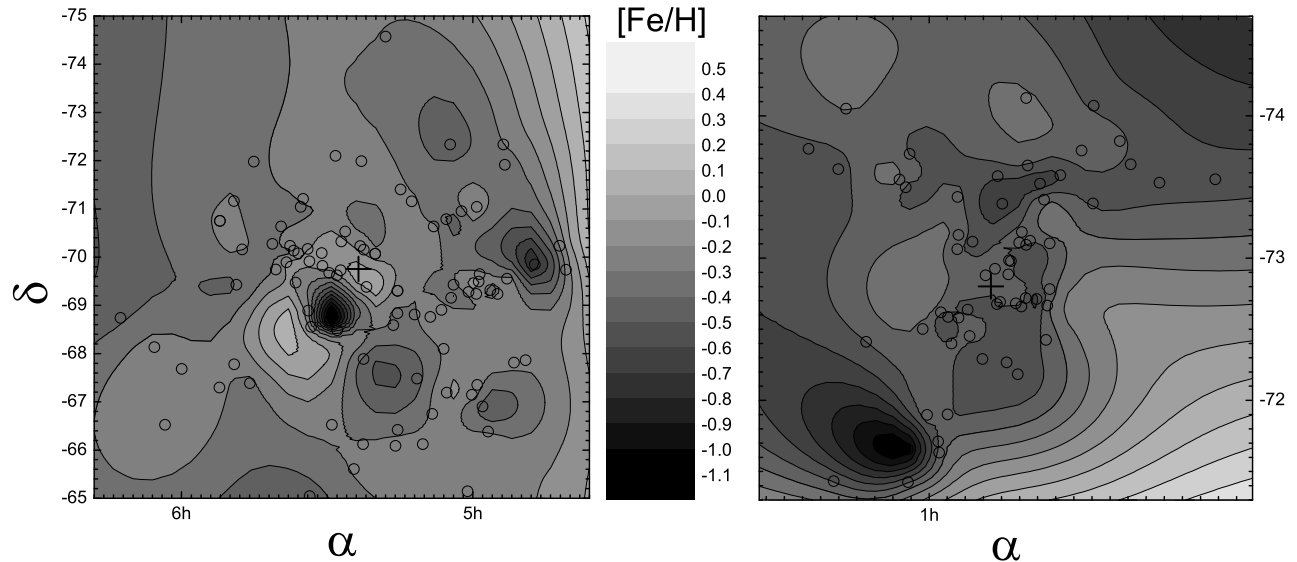
Figure 4: The [Fe/H] distribution in the LMC (*left*) and SMC (*right*) projected on the celestial sphere. *Open circles*: positions of the stars; *bold crosses*: positions of the galactic centres.

by Soszynski et al. (2011) in the Galactic bulge. We have also derived [Fe/H] for those Cepheids: –0.39 dex for OGLE-BLG-CEP-03 and –0.29 dex for OGLE-BLG CEP-21. The estimates are also given in Fig. 2 and Fig. 3.

6. Conclusions

New, accurate, and homogeneous abundances for a number of chemical elements, as well as physical atmospheric parameters, were determined for a large number of Galactic bimodal Cepheids using high-resolution and high S/N echelle spectra. The new abundances obtained and fundamental parameters are in good agreement with the results of other analyses in the literature.

A statistical analysis of the P_1/P_0–$A(El)$ correlation was conducted. The observed period ratios for the program stars exhibited a strong dependence on the abundances of several chemical elements. A new, more accurate P_1/P_0–[Fe/H] relation was suggested.

Based on the newly suggested relation, alternative [Fe/H] values were found for a large number of beat Cepheids in the Magellanic Clouds, and thereby independent average metallicities for the Magellanic Clouds were obtained. The metallicity distribution function for the Magellanic Clouds projected on the celestial sphere was constructed for the first time.

The [Fe/H] values for two new double-mode P_1/P_0 Cepheids in the Galactic bulge were estimated for the first time.

References

Andrievsky S.M., Kovtyukh V.V., Luck R.E., et al.: 2002, *A&A*, **381**, 32.

Chekhonadskikh F.A.: 2012, *KPCB*, **28/3**, 128.

Galazutdinov G.A.: 1992, *Prepr. SAO RAS*, **92**, 2.

Grevesse N., Noels A. & Sauval J.: 1996, *ASP Conf. Ser.*, **99**, 117.

Kovtyukh V.V.: 2007, *MNRAS*, **378**, 617.

Kovtyukh V.V. & Andrievsky S.M.: 1999, *A&A*, **351**, 597.

Kovtyukh V.V., Gorlova N.I. & Hillen M.: 2012, *OAP*, **25/1**, 52.

Marquette J.B., Beaulieu J.P., Buchler J.R., et al.: 2009, *A&A*, **495**, 249.

Soszyński I., Poleski R., Udalski A., et al.: 2008, *Acta Astron.*, **58**, 163.

Soszyński I., Poleski R., Udalski A., et al.: 2010, *Acta Astron.*, **60**, 17.

Soszyński I., Udalski A., Pietrukowicz P., et al.: 2011, *Acta Astron.*, **61**, 285.

Sziládi K., Vinkó J., Poretti E., et al.: 2007, *A&A*, **473**, 579.

Udalski A., Szymański M.K., Soszyński I. & Poleski R.: 2008, *Acta Astron.*, **58**, 69.

SEASONAL VARIATIONS OF IONOSPHERIC LAYER PARAMETERS DURING THE PERIOD OF MAXIMUM SOLAR ACTIVITY

Kravetz R.O.[1], Galanin V.V.[2]

Institute of Radio Astronomy of National Academy of Science of Ukraine, Odessa, Ukraine
[1]krro@ukr.net, [2]gvv@mail.ru

ABSTRACT. Critical frequencies of the ionospheric layers were studied using data from the European Digital Upper Atmosphere Server (DIAS) network of real-time ionosondes for 2012-2013. Some particularities of seasonal variations of these parameters were detailed.

From the moment of its discovery in the beginning of 20th century, the Earth's ionosphere has been the subject of continuous research that is caused by its leading role in the propagation of radio waves in the decameter wave band. In radio astronomy, the ionosphere represents a disturbance factor due to its distortion of signals from cosmic radio sources which are received by the ground-based radio telescopes. Therefore, the study of ionospheric characteristics, particularly ionospheric disturbances, is a crucial task indeed.

Main ionospheric parameters are measured by ionospheric stations, which are called ionosondes. In Europe, the ionosondes are united into a network called DIAS (the European Digital Upper Atmosphere Server) [1, 2]. The DIAS data are freely available and easily accessible via Internet. These data are displayed mainly as ionograms – plots of the virtual height of the reflection point in the ionosphere against frequency measured using vertical sounding. An ionogram is a display of the initial material obtained by an ionosond. Ionograms allow of determining all parameters of the ionospheric layers. The results of data processing are reported in the form of tables which are released on the web.

In this study we used data from three DIAS ionosondes, namely Athens, Chilton and Pruhonice. We also used some data from ionosondes Rome and Warszawa. These data were obtained from automatic processing (auto-scaling). It allows to get long sequences of these data, as well as to detect specific features, in particular, seasonal variations. To be specific, we used data for 2012-2013. This period is of particular interest, because it corresponds to the maximum of Solar Cycle 24.

Generally speaking, seasonal variations of ionospheric layer parameters, as well as other ionospheric characteristics, have been extensively studied and described by many authors [3]. However, availability of large amount of observation material and its accessibility allow, first, to examine previous conclusions and, secondly, refine and expand them. In particular, it is known that critical frequencies of D and E layers increase at middle latitudes during summer months and decrease in winter. The situation is opposite for the F_2 layer - the critical frequency of this layer decreases in summer months and increases in winter. We consider that it is useful to examine these conclusions and extend the range of such variations. That is the aim of this study.

As in our previous paper [4], we focus mainly on the E_s layer (sporadic E-layer) as on our opinion, it has the most significant influence on radio telescopes operating at decameter wavelength, because its critical frequency can reach very high values, and in some cases, it even exceeds the F_2 layer critical frequency. It is shown in [4] that sporadic E-layer is, generally speaking, a regular layer, because it is present practically all year long while its critical frequency does not exceed 3-4 MHz. Sometimes this value can reach 10-15 MHz and above. In such cases we can discuss the appearance of the sporadic layer itself. As such an appearance of sporadic layer is a seldom case, it is interesting to study the frequency of this phenomenon, i.e. the probability of its occurence.

Apart from the sporadic E-layer, the F_1 layer – a typical day-time phenomenon – is also of our interest. The F_1 layer particularities are also the subject of our study, because one border of this layer adjoins the sporadic E-layer while the other one is adjacent to the F_2 layer.

Figure 1 shows an example of the dependence of the E, F_1 and F_2 layers' critical frequencies on time for the interval of three days. Gaps on the plot signify the absence of corresponding layers on the ionograms.

Figure 1: Critical frequencies of ionospheric layers for three days
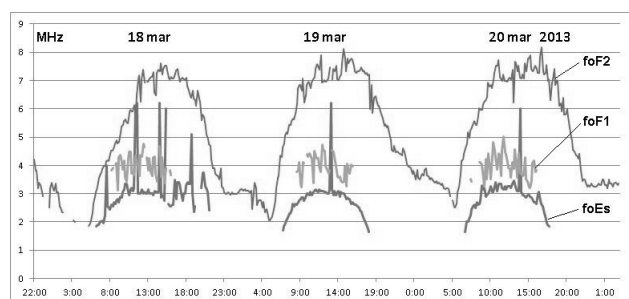
The data for this plot were taken from the Chilton ionosonde's data-output for 18-20 March 2013. These data show typical diurnal variation of critical frequencies of these layers with maximum in the daytime around noon and minimum at night; hence, there are no signals reflected by E_s and F_1 layers at night. As can be seen on the plot, some plot points for the sporadic E-layer's critical frequency curve greatly exceed the mean values. Obviously, only these points correspond to the appearance of the sporadic layer itself, because it is presumed that this layer appears only when its critical frequency is higher than 4-5 MHz.

As it seen from Figure 1, the ionospheric layers' critical frequencies vary greatly throughout the day; thus, to determine their dependencies on time for long periods, for example for a year, the corresponding values should be averaged in some way. For the mean values we took critical frequencies averaged over 4 hours near the maximum.

Using this method we got data sequences for which a single critical frequency corresponds to one day.

Figure 2 shows time dependencies of data from the Chilton ionosonde for 2012-2013, which were processed by the indicated method. Figure 3 shows such correlation for the Pruhonice ionosonde data-output. We have got similar critical frequency-time relationships for the Athens, Rome and Warszawa ionosondes. To perform direct visual evaluation, we made further averaging of the data. In particular, using a 10-day moving average we

processed data from three mentioned ionosondes. Figures 4 and 5 present the plots of these data for the Chilton and Pruhonice ionosondes, respectively. These plots show that the critical frequencies of sporadic E-layer and F_1 layer have almost similar yearly variation with maximum in July-August and minimum in January-February. Hence, the F_1 layer critical frequency almost always exceeds the critical frequency of sporadic E-layer at 0.5-1.5 MHz. The difference between maximum and minimum values is 1.5-2 MHz for the F_1 layer and 3-4 MHz for the E_s layer.
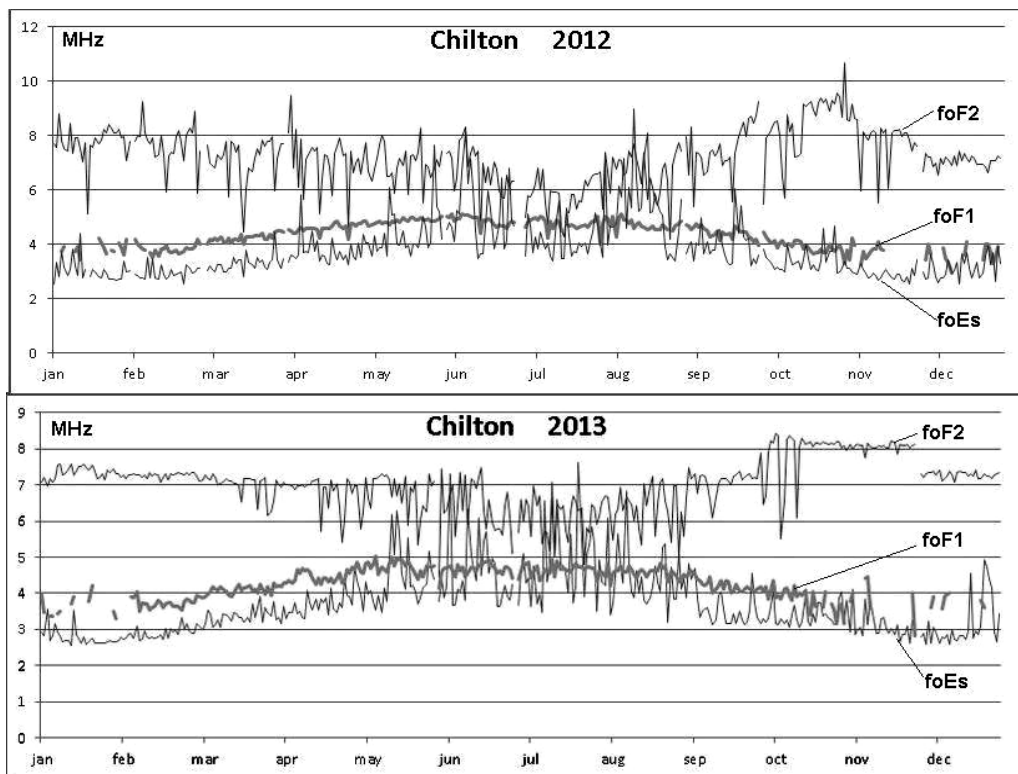
Figure 2: Critical frequencies of ionospheric layers measured by Chilton ionosonde in 2012–2013
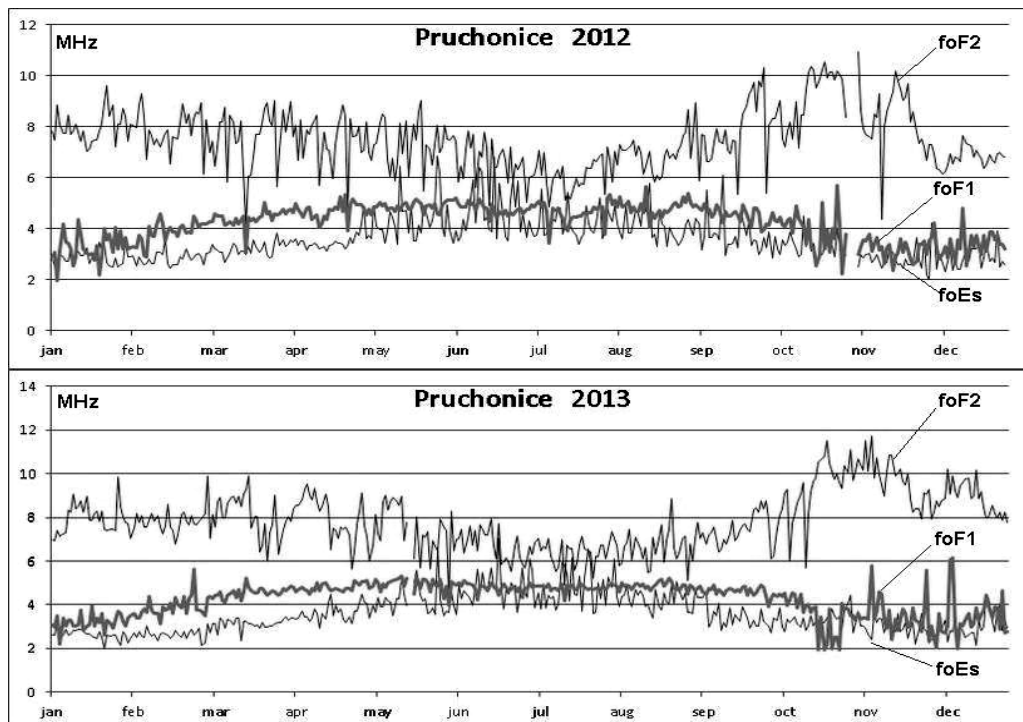
Figure 3: Critical frequencies of ionospheric layers measured by Pruchonice ionosonde in 2012–2013
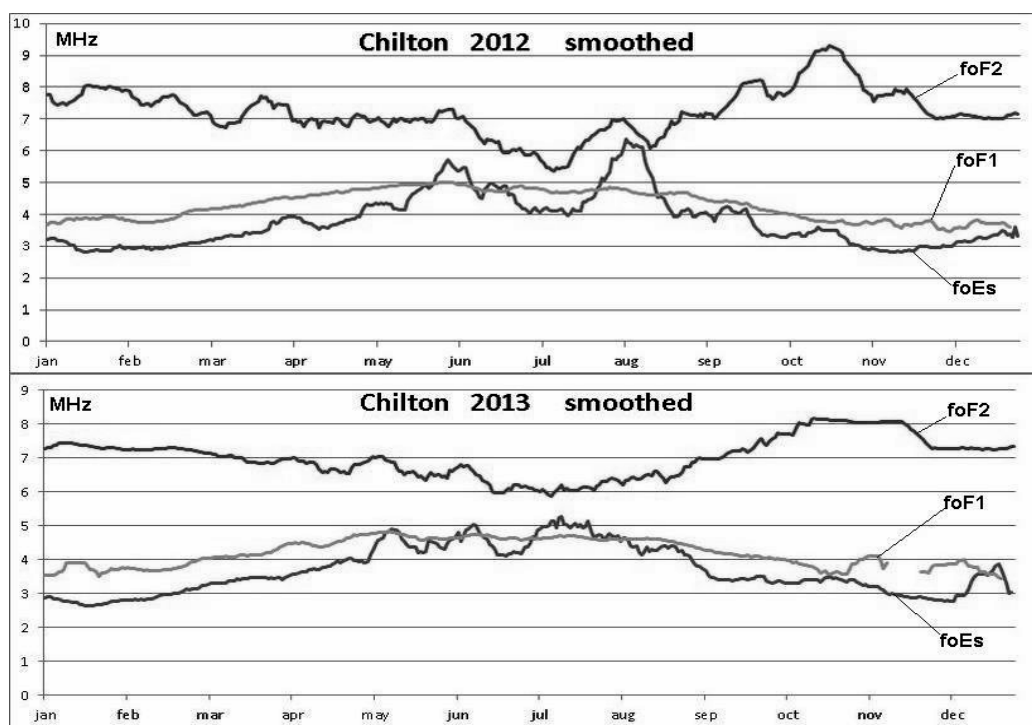
Figure 4: Critical frequencies measured by the Chilton ionosonde in 2012–2013 smoothed with a 10-day moving average
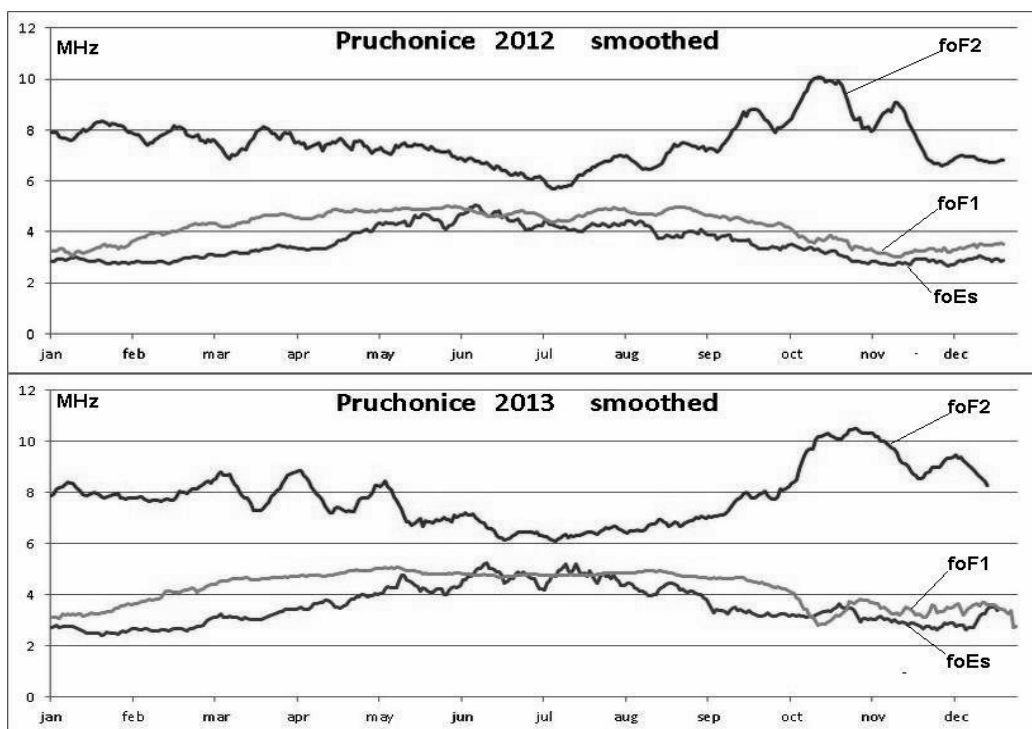
Figure 5: Critical frequencies measured by the Pruchonice ionosonde in 2012–2013 smoothed with a 10-day moving average

On the contrary, the F_2 layer critical frequency is minimum in July and maximum in November. The difference between its maximum and minimum values is 3-4 MHz.

References

1. DIAS: European Digital Upper Atmosphere Server. *http://www.iono.noa.gr/dias.*

2. Belehaki A., Cander Lj.R., Zolesi B., Bremer J., Jurén C., Stanislawska I., Dialetis D., Hatzopoulos M.: 2005, *J. Atmos. Sol-Terr. Phys.*, **67(12)**, 1092.

3. Brunelli B.E., Namgaladse A.A. *Physics of ionosphere*, M.: Nauka, 1988.

4. Kravetz R.O., Galanin V.V.: 2013, *Odessa Astron. Publ.*, **26/2**, 245.

PARTICLES, NEUTRINO AND PHOTONS IN THE MAGNETOSPHERE OF A COLLAPSING STAR

V.G. Kryvdyk

Faculty of Physics, Taras Shevchenko National University of Kyiv
64/13, Volodymyrska Street, 01601, Kyiv, Ukraine
kryvdyk@gmail.com

ABSTRACT. The formation of the stellar magnetosphere during the gravitational collapse is discussed. Primary protons and electrons accelerate in the star's magnetosphere during its gravitational collapse. In what follows, the flux of particles, photons and neutrinos generated in the magnetosphere is multiplied in a cascade process initiated by the self-interaction of particles and their interaction with magnetic fields. These processes are especially effective for the formation of magnetospheres in collapsing stars.

Key words: stellar collapse, particle acceleration, neutrino generation, magnetospheres of collapsing stars

1. Introduction

In this paper we will discuss the generation of particles, neutrino and photons in the magnetosphere of a magnetized star with the initial dipolar fields during its gravitational collapse. Gravitational collapse occurs at the final stage of stellar evolution. Gravitational collapse starts when the mass of a stellar core exceeds the Chandrasekhar limit and a star becomes dynamically unstable. After that, the star can evolve in several ways. Depending on the mass and chemical composition, a star can evolve into either of three relativistic objects, such as a white dwarf, neutron star or black hole (Zeldovich & Novikov, 1977; Shapiro & Teukolsky, 1985; Arnett, 1979). The progenitors of the relativistic massive objects could be red and blue giants, Wolf-Rayet (WR) stars, as well as supermassive stars (Cherepashchuk, 2003; Eldridge & Tout, 2004; Wooslej & Heger, 2006). WR stars can originate from the helium cores of massive stars which lost their hydrogen shells or they can be formed as a result of either mass exchange in close binary systems or intense mass-loss of single stars due to strong stellar winds. The masses of CO-cores of WR stars are continuously distributed within the range from 5 $M_\circ$ to 55 $M_\circ$ (Cherepashchuk, 2003). WR stars are stars at advanced stages of stellar evolution. They are resulted from the collapse of carbon-hydrogen (SB) stellar cores and can be reckoned as the immediate progenitors of relativistic objects. The core collapse may be followed by the explosion and formation of type Ib or Ic supernovae. Moreover, relativistic objects can also be a result of the evolution of massive red and blue supergiants with normal chemical composition. For example, supergiant V3I was the progenitor of Supernova 1987A in LMC (Chevalier, 1995). O and B stars with masses M > 10 $M_\circ$ are early-type massive stars. They generate powerful stellar winds and emit intense infrared radiation. Some of them are radio-

frequency sources. The stellar wind velocities of O stars reach 3000 km/s, and the mass loss is 10^{-5} $M_\circ$ per year.

The observational measurements of magnetic fields of different stars show the presence of strong magnetic fields in the upper atmospheres of WR and massive stars. For example, the β Cep (B2V) magnetic field is 360 Gs (Donati et al., 2001), the θ1OriC (O4-6V) field is about 1100 Gs (Donati et al., 2002), and that one of ζ Sas (B2IV) is 335 Gs (Neiner et al., 2003). Far more intense magnetic fields are observed in very young massive stars W601 (NGC 6611) - up to 1400 Gs and OI 201 (NGC 2244) - up to 550 Gs (Alecian et al., 2008). The magnetic fields observed on the surface of the supergiant O9.7 ζOrionisA were about 100 Gs (Bouret et al., 2008). 521 WDs with fields in the range from 1 to 733 MG were found in the Sloan Digital Sky Survey Data Release 7 (Kepler et al., 2013). The magnetic fields of these stars are of dipolar type (Kepler et al., 2013; Jordan, 2009). 67 new measurements of magnetic fields for 30 massive stars in the range from 10 G to 380 G made with FORS 2 at the VLT are given in the catalogue by Hubrig (Hubrig et al., 2013). The magnetic fields in about 65 from 550 stars were observed in the MiMeS project (Wade et al., 2013). The magnetic fields observed have important dipole components with polar strengths from several hundred G up to 20 kG.

We will examine gravitational collapse of a magnetized star with the initial dipolar magnetic fields and initial heterogeneous distribution of protons and electrons according to a power law (p), relativistic Maxwell (M) and Boltzmann (B) distributions.

The external electromagnetic field of a collapsing star changes according to the following law (Ginzburg & Ozernoi, 1964):

$$B_r = 2r^{-3}\mu(t)\cos\theta,$$
$$B_\theta = r^{-3}\mu(t)\sin\theta,$$
$$B_\varphi = 0, \qquad (1)$$
$$\mathcal{E}_\varphi = -c^{-1}r^{-2}\frac{\partial\mu}{\partial t}\sin\theta,$$
$$\mathcal{E}_r = \mathcal{E}_\theta = 0.$$

Where B_r, B_θ, B_φ and $\mathcal{E}_r$, $\mathcal{E}_\theta$, $\mathcal{E}_\varphi$ are the components of magnetic and electric fields, respectively; $\mu(t) = (1/2)F_0R(t)$ is the magnetic momentum of the star with radius $R(t)$ that changes with time; $F_0 = 4\pi R_0^2 B_0^2$ is the initial magnetic flux of the star; R_0 is the initial radius of star; θ and φ are the polar and azimuth angles, respectively.

Full dipole magnetic field in the magnetosphere of a collapsing star is defined by the following equation (Kryvdyk, 2010):

$$B(r, \theta, R) = \left(B_r^2 + B_\theta^2 + B_\varphi^2\right)^{\frac{1}{2}} = \frac{\mu(t)}{r^3}(1 \cdot 3\cos^2\theta)^{1/2}$$
$$(2)$$

Eqs. (1) describes the external electromagnetic field of a collapsing star with the Newtonian potential. Due to a large mass-to charge ratio of a particle, Newton's method will be always suitable for description of the field in the magnetosphere of a collapsing star, excluding the area near the Schwarzschild radius. The stellar magnetosphere is compressed during a collapse as a result of the magnetic field strength increase. This variable magnetic field will generate the vortex electric field, which will accelerate the charged particles to relativistic energies. In the course of a core-collapse the magnetic field of a star changes according to the law (1) increasing up to 10^{12}G at the final stages of the collapse. The energy of particles changes because of betatronic acceleration, produced by the electric field E_φ, as well as energy losses due to magnetic braking.

During a collapse primary charged particles accelerate to relativistic energies (Kryvdyk, 1999; 2001; 2003; 2004; 2010). The energy of particles changes as per (Kryvdyk, 2010):

$$E/E_0 = (R_0/R)^{-A_1(\theta)}. \qquad (3)$$

Where

$$A_1(\theta) = \frac{5}{3}k_1(3\cos^4\theta + 1.2\cos^2\theta - 1)(1 + \cos^2\theta)^{-2}$$

with $k_1 = 2$ for non-relativistic particles, and $k_1 = 1$ for relativistic particles; and E_0 is primary particle energy.

Figure 1 shows the distribution of particle energy in the magnetosphere according to a power law as a function $R_* = R_0/R$ and $E_* = E/E_0$ (Kryvdyk, 2010).
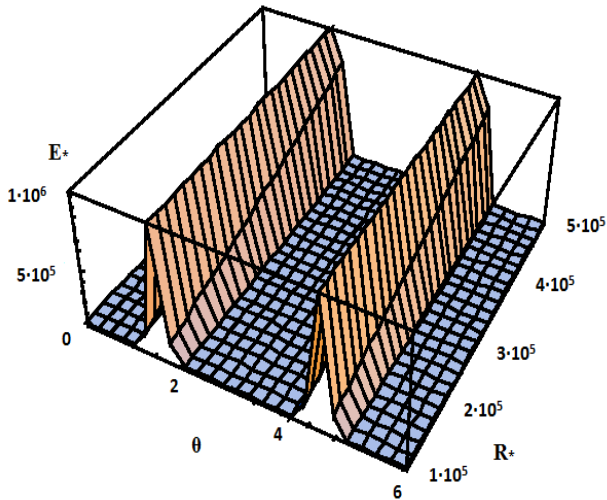
At the final stage of the collapse, electrons accelerate to energies $\leq 10^{11}eV$ while protons – to $E \leq 2 \cdot 10^{14}eV$ (Kryvdyk, 2010).

The initial magnetosphere of a collapsing star consists of protons and electrons distributed according to a power law (p), relativistic Maxwell (M), and Boltzmann (B) particle distributions; and the magnetosphere's density changes as r^{-3}. In the study by Kryvdyk (2010), the evolution of the particle energy spectrum for such distributions was determined for two extreme cases: (i) when energy losses due to magnetic braking do not affect the spectrum, and (ii) when they determine the spectrum evolution.

Figure 2 presents the particle number density $N_* = N/N_0$ in the magnetosphere near the star's surface as a function $R_* = R_0/R$ and polar angle θ for the power-law distribution of particles (Kryvdyk, 2010).
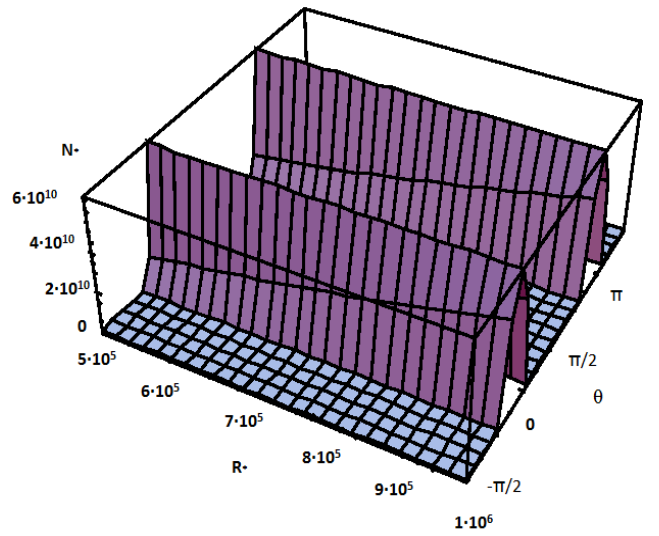

Figure 2: The particle number density in the magnetosphere near the star's surface at the final stage of the collapse with $R_* = R_0/R$ and $N_* = N/N_0$.

Interacting among themselves and with the magnetosphere's magnetic fields, accelerated charged particles will lose their energy due to ionization and radiation. At the same time, secondary charged particles (electrons, positrons, protons, and mesons), as well as neutrons, neutrino and photons are generated in the magnetospheres of collapsing stars. These secondary charged particles will also accelerate in the increasing magnetic fields during collapses. In the course of multiple cascade interaction, secondary particles will also generate other particles and photons. Therefore, the collapsing star magnetosphere consists of charged particles, neutrons, neutrinos and photons.

2. Generation of high-energy neutrinos, particles and photons in the collapsing star magnetosphere

In this section, we will consider in detail the generation of charged particles, neutrons, photons and neutrinos in the magnetosphere of collapsing stars.

The generation of these particles is shown in Table 1.

Figure 1: The change in particle energy distributed according to a power law during a collapse in the magnetosphere of a star with $R_* = R_0/R$, and $E_* = E/E_0$.

Table 1: The generation of particles in the magnetosphere of a collapsing star

Acceleration of the initial protons and electrons		
↓		
Generation and acceleration of secondary particles) →	Generation and acceleration of tertiary particle→···	….Multiple generation and acceleration of particles
Protons (p) **Neutrons (n)** **Electrons (e⁻)** **Positrons (e⁺)** **Mesons (π, μ)** **Neutrino (ν)** **Antineutrino(ν⁻)** **Photons (γ)**	**Protons (p)** **Neutrons (n)** **Electrons (e⁻)** **Positrons (e⁺)** **Mesons (π, μ)** **Neutrino (ν)** **Antineutrino(ν⁻)** **Photons (γ)**	**Protons (p)** **Neutrons n)** **Electrons (e⁻)** **Positrons (e⁺)** **Mesons (π, μ)** **Neutrino (ν)** **Antineutrino(ν⁻)** **Photons (γ)**

Especially important are cascade showers of charged particles, neutrons, neutrinos and photons generated in the magnetosphere. These processes are very effective for the formation of magnetosphere of a collapsing star.

Secondary charged particles, neutrons, neutrinos and photons can be generated in the magnetosphere of a collapsing star, namely:

2.1. π-mesons, μ-mesons, electrons, positrons and neutrinos produced in nuclear interactions;

2.2. electron-positron pairs resulted from annihilation of gamma quanta in a nuclear field;

2.3. electron-positron pairs resulted from the collision of charged particles;

2.4. electron-positron pairs resulted from photon-photon collisions;

2.5. μ-meson pairs produced by passing of gamma quanta in a nuclear field;

2.6. recoil electrons resulted from the collision of charged particles;

2.7. electron-positron pairs produced in a strong curvilinear magnetic field.

2.1. Generation of π-mesons, μ-mesons, electrons, positrons and neutrinos by nuclear interactions in the magnetosphere of a collapsing star

In earlier studies of the author (Kryvdyk, 1999; 2001; 2003; 2004; 2010) it was reported that primary protons and electrons accelerate in the magnetosphere of a collapsing star to relativistic energies. The accelerated protons will interact with other protons in the magnetosphere, generating mesons in the following nuclear interactions (Leng, 1974; Hajakawa, 1978a; 1978b):

$$p + p \rightarrow p + p + n_1 \left(\pi^+ + \pi^-\right) + n_2\pi^0,$$
$$p + p \rightarrow p + n + \pi^+ + n_3 \left(\pi^+ + \pi^-\right) + n_4\pi^0, \quad (4)$$
$$p + p \rightarrow n + n + 2\pi^+ + n_5 \left(\pi^+ + \pi^-\right) + n_6\pi^0,$$
$$p + p \rightarrow D + \pi^+ + n_7 \left(\pi^+ + \pi^-\right) + n_8\pi^0,$$
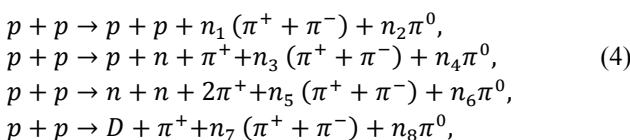
where p – protons; n – neutrons: D – deuterons; n_1-n_2 – positive integers.

The secondary electrons, positrons, photons and neutrinos will generate in the later on by decay of mesons:

$$\pi^\pm \rightarrow \mu^\pm + \nu_\mu/\bar{\nu}_\mu$$
$$\pi^0 \rightarrow \gamma + \gamma \quad (5)$$
$$\mu^\pm \rightarrow e^\pm + \nu_e/\bar{\nu}_e + \nu_\mu/\bar{\nu}_\mu,$$

For relativistic protons with energy from *290 MeV* to *1 GeV* only one with next reaction can be possible (Leng, 1974):

$$p + p \rightarrow p + n + \pi^+ , \text{ or } p + p + \pi^0, \text{ or } D + \pi^+. \quad (6)$$

The minimum proton energy E_{min} for the generation of π-mesons is

$$E_{min} = \frac{Y^2 m_\pi^2 c^4}{2m_p c^2} + 2Y m_\pi c^2 \approx Y(280 + 10Y)[\text{MeB}],$$

where $m_\pi c^2$ and $m_p c^2$ the rest energy of a π-meson and a proton, respectively.

Π-mesons can be generated only by protons with energy higher than 290 MeV. These protons can accelerate in the variable magnetic fields in the magnetosphere of a collapsing star (Kryvdyk, 1999; 2001; 2003; 2004; 2010). Neutral neutrons are also generated by reactions (4) - (6). Neutrons do not interact with the magnetic fields; and therefore, they freely go out of the magnetosphere, forming the neutron wind around the collapsing star. When there are sufficient amount of free neutrons and protons, neutrinos can be resulted from Urca processes in which neutrons and protons capture electrons or positrons, causing radiation of energy in the form of neutrinos in the following reactions (Chiu & Salpeter, 1964):

$$p + e^- \rightarrow n + \nu_{e,}$$
$$n + e^+ \rightarrow p + \bar{\nu}_{e,} \quad (7)$$
$$n \rightarrow p + e^- + \bar{\nu}_{e,}$$

Intense magnetic fields will influence the rate of Urca-reactions. In very strong magnetic fields ($H \geq 4 \cdot 10^{13}$ *Gs*) urca- processes can arise in hundred time (Canuto V., et al. 1970, Fassio–Canuto 1969).

Quasi-free pions will be also generated in the magnetosphere of a collapsing star resulting from reactions (4) and (6). Therefore, the following Urca-reactions in which neutrinos, electrons and pions are generated, are possible in the magnetosphere:

$$\pi^- + n \rightarrow n + e^- + \bar{\nu}_e ,$$
$$n + e^- \rightarrow n + \pi^- + \nu_{e,}$$
$$\pi^- + n \rightarrow n + \mu^- + \bar{\nu}_\mu ,$$
$$n + \mu^- \rightarrow n + \pi^- + \nu_\mu. \quad (8)$$

2.2. Generation of electron-positron pairs as results of annihilation of gamma quanta in a nuclear field

The electron-positron pairs will be generated during passing of gamma-photons with energy $h\nu > 2m_e c^2 = 1.022$ *MeV* in the nuclear Coulomb field with charge eZ,

where $m_e c^2 \approx 0.511\ MeV$ is the electron rest energy. For photons with energy $h\nu \gg m_e c^2$ the cross-section of electron-positron pair generation is as follows (Leng, 1974):

$$\sigma(h\nu) = 4\alpha Z^2 r_0^2 \left[\frac{7}{9}\ln\left(\frac{2h\nu}{m_e c^2}\right) - \frac{109}{54}\right] \text{ for } h\nu \ll \frac{m_e c^2}{\alpha Z^{1/3}}, \quad (9)$$

$$\sigma(h\nu) = 4\alpha Z^2 r_0^2 \left[\frac{7}{9}\ln\left(\frac{191}{Z^{1/3}}\right) - \frac{1}{54}\right] \text{ for } h\nu \gg \frac{m_e c^2}{\alpha Z^{1/3}},$$

where $r_0 = e^2/m_e c^2 \approx 2.8 \cdot 10^{-13}\ cm$ is the classical electron radius; $\alpha \approx 1/137$ is the fine-structure constant. The value $4\alpha r_0^2 \approx 2.3 \cdot 10^{-27}\ cm^2$.

The main nuclei in the magnetosphere are protons (Z=1); therefore, the cross-sections of electron-positron pair generation due to the interaction of gamma-photons with protons are:

$$\sigma_{php}(h\nu) \approx 2.3 \cdot 10^{-27} \left[\frac{7}{9}\ln\left(\frac{2h\nu}{m_e c^2}\right) - \frac{109}{54}\right] \text{ for } h\nu \ll 70\ MeV,$$

$$\sigma_{php}(h\nu) \approx 2.3 \cdot 10^{-27} \left[\frac{7}{9}\ln(191) - \frac{1}{54}\right] \text{ for } h\nu \gg 70\ \text{Me}V.$$
$$(10)$$

The numerical values of nuclear cross-section in this case are:

$$\sigma_{php}(h\nu) \approx 4.2 \cdot 10^{-28}\ cm^2 \text{ for } h\nu \ll 70\ MeV, \quad (11)$$

$$\sigma_{php}(h\nu) \approx 9.4 \cdot 10^{-27}\ cm^2 \text{ for } h\nu \gg 70\ MeV.$$

2.3. Generation of electron-positron pairs by the interaction of charged particles

The electron-positron pairs will be resulted from the interaction of electrons with protons. The cross-section for the electron interactions is as follows (Leng, 1974):

$$\sigma_{ep}(h\nu) = \frac{28}{27\pi}\alpha^2 r_0^2 \ln(1/\alpha)\left[3\ln\left(\frac{E_e}{m_e c^2}\right)\ln\left(\frac{E_e}{191 m_e c^2}\right) + \ln^2(191)\right], \quad (12)$$

where E_e is electron energy.

For the numerical values $\alpha \approx 1/137$ and $r_0 \approx 2.8 \cdot 10^{-13}\ cm$, $m_e c^2 \approx 0.511\ \text{Me}V$ we obtain the following cross-sections:

$$\sigma_{ep}(h\nu) \approx 6.8 \cdot 10^{-30}[3\ln(2\ E_e)\ln(10^{-2}E_e) + 27.6]. \quad (13)$$

Their numerical values is

$$\sigma_{ep}(h\nu) \approx 6.3 \cdot 10^{-29} cm^2 \quad (14)$$

2.4. Generation of electron-positron pairs in photon-photon collisions

Electron-positron pairs can be also generated in the magnetosphere as a result of collisions of two photons with energies E_1 and E_2 (given that $E_1 E_2 > (m_e c^2)^2$. The cross-section for this interaction is as follows (Leng, 1974; Heitel, 1954):

$$\sigma_{2ph}(E_1, E_2) = \frac{\pi r_0^2}{2}(1 - \beta^2)\left[2\beta(\beta^2 - 1) + (3 + \beta^4)\ln\left(\frac{1+\beta}{1-\beta}\right)\right]. \quad (15)$$

Where $\beta = \left[1 - \frac{(m_e c^2)^2}{E_1 E_2}\right]^{1/2}$, βc is the electron velocity in the center-of-mass system.

Value $\sigma_{2ph}(E_1, E_2)$ change in range

$$5.2 \cdot 10^{-26} \leq \sigma_{2ph}(E_1, E_2) \leq 2.9 \cdot 10^{-25}\ cm^2 \quad (16)$$
$$\text{for } 0.85 \leq \beta \leq 0.999.$$

2.5. Generation of μ-meson pairs by annihilation of gamma quanta in nuclear field

If the energy of a gamma photon exceeds the threshold energy $2m_\mu c^2 \sim 211\ MeV$, then a $\mu^\pm$ pair is to be produced in the interaction of this photon with the nuclear Coulomb field. The cross-section of this interaction can be obtained from equation (9) just by replacing the electron mass m_e with the meson mass m_μ. The value $m_e/m_\mu \sim (1/207)^2 \sim 1.37 \cdot 10^{-5}$; thus, for μ-meson pairs

$$\sigma_{p\gamma}(h\nu) \approx 1.29 \cdot 10^{-32}\ cm^2 \quad (17)$$

2.6. Generation of recoil electrons in collisions of charged particles

Recoil electrons will be generated in collisions of charged particles with other particles. The magnetosphere of a collapsing star consists substantially of electrons and protons. The cross-section of the generation of recoil electrons with energy E_e in collisions with relativistic protons with energy E_p and charge eZ is as follows (Leng, 1974; Hajakawa, 1978a; 1978b):

$$\sigma_p(E_p, E_e)dE_e \approx 2\pi r_0^2 \frac{m_e c^2}{\beta_p^2 E_e^2} dE_e, \quad (18)$$

where $\beta_p = \left[1 - (m_p c^2)^2/E_e E_p\right]^{1/2}$, $\beta_p c$ is the proton velocity in the center-of-mass system.

The numerical value this cross-section is

$$\sigma_p(E_p, W_e)dW_e \approx 2.55 \cdot 10^{-25} \frac{1}{\beta_p^2 W_e^2} dW_e. \quad (19)$$

The upper limit of energy for this process is $E_e \approx pc$, where p is impulse of the incident particle.

As follows from section 2, the initial electrons and protons in the magnetosphere of collapsing star will accelerate to relativistic energy. The relativistic electron will lose their energy in the magnetic fields significant fast from proton, and therefore the electron lifetime is significant less from the proton lifetime. In the magnetosphere will generate also the second electrons by the mutual collisions protons with electrons.

2.7. Generation of electron-positron pairs in a strong magnetic field

If the magnetic fields arise to critical value

$$B_c = m_e^2 c^3/e\hbar = 4{,}4 \cdot 10^{13}\ G, \quad (20)$$

where m and e are the electron mass and charge, respectively; h is Planck's constant; then the electron-positron plasma will be produced via direct vacuum decay.

In the system with a sufficiently strong curvilinear magnetic field the decay can occur in a much weaker magnetic field. This mechanism is effective for the formation of magnetospheres in pulsars with strong surface magnetic fields (Goldreich and Julian 1969; Sturrock, 1971; Ruderman and Sutherland, 1975). By rotating neutron stars with radius R and the magnetic fields B near surface will generate the parallel electric fields

$$E_\parallel \approx \Omega R B / c, \qquad (21)$$

where Q is the rotational velocity, and c is the speed of light.

The electrons and positrons will accelerate to relativistic energies in this electric field. Moving along the curvilinear magnetic field, they will emit the so-called curvature photons whose energy is sufficient to produce electron-positron pairs in the magnetic field. These pairs also accelerate to high energies in parallel electric fields (2) where they can produce pairs themselves, emitting curvature photons. This is the main mechanism of generation of multiple electrons, positrons and γ photons. The multiplication coefficient will increase as the particles produced in a high Landau level in the magnetic field emit synchrotron radiation, i.e. synchrophotons, which can also produce pairs.

At the collapse's final stage, magnetic fields near the star's surface can increase to value $B \sim 10^{12}$ *Gs;* thus, the generation of multiple electrons, positrons and γ photons in the curvilinear magnetic field can be the effective mechanism of formation of electron-positron pairs in magnetosphere of collapsing stars.

3. Neutrino generation in the magnetosphere of a collapsing star

Secondary neutrons, protons, electrons, positrons and photons are generated in the magnetosphere of a collapsing star as results of different processes. These particles will produce neutrinos by interactions with particles and fields in the magnetosphere. In the neutral non-degenerate plasma the main processes of neutrino generation are the following (Leng, 1974; Fassio-Canuto, 1969; Braaten & Segel, 1993; Bruenn, 1985; Dicus, 1972; Itoh et al., 1989; Koers & Wijers, 2005; Lattimer et al., 1991; Munakata et al., 1985; Qian & Woosley, 1996; Ratkovic et al., 2003; Reynoso et al., 2006):

3.1. Bremsstrahlung by electron-atom collision
   $e^- + (Z, A) \rightarrow (Z-1, A) + \nu_e + \overline{\nu}_e$;
3.2. Neutrino emission in Urca processes in the magnetosphere;
3.3. Bremsstrahlung of the charged particles in strong magnetic fields;
3.4. Photoneutrino reactions $e^\pm + \gamma \rightarrow e^\pm + \nu_e + \overline{\nu}_e$;
3.5. Plasmons decay $\Gamma \rightarrow \nu_e + \overline{\nu}_e$;
3.6. Annihilation of electron-positron pairs
   $e^+ + e^- \rightarrow \nu_e + \overline{\nu}_e$;
3.7. Generation of neutrinos in meson decay.

We will consider these processes in detail in next subsection.

3.1. Neutrino emission by electron-atom collision

Neutrino can be emitted due to electron-atom bremsstrahlung, when a free electron collides with a nucleus *(Z, A)*. As a result a pair of neutrino-antineutrino will be produced (Leng, 1974; Pontekorvo, 1959):

$$e^- + (Z, A) \rightarrow (Z-1, A) + \nu_e + \overline{\nu}_e . \qquad (22)$$

For this process the neutrino luminosity is as follows (Koers & Wijers, 2005; Qian & Woosley, 1996; Reynoso et al., 2006):

$$Q_{\nu\,br} = 1.5 \cdot 10^{27} \, T_{11}^{5.5} \, \rho_{10}^2 \, \frac{Erg}{cm^3 \cdot sec}, \qquad (23)$$

where the temperature is $T_{11} = T/10^{11}$ *K*, the baryon density is $\rho_{10} = \rho/10^{10}$ *g/cm³*. From now on the unit of neutrino luminosity Q_ν is $\frac{Erg}{cm^3 \cdot sec}$.

By replacing temperature T with energy E *(eV)* from the relation

$$T[K] = E/k = 1{,}16 \cdot 10^4 \, E[eV], \qquad (24)$$

we obtain

$$Q_{\nu\,br} = 3.5 \cdot 10^{49} \, E_{11}^{5.5} \, \rho_{10}^2 , \qquad (25)$$

where the unit energy E is *eV*.

The energy of particles in the magnetosphere during gravitational collapse increase as $E/E_0 = (R_0/R)^{-A_1(\theta)}$ (see Eq. 3).

Therefore, the neutrino luminosity in the magnetosphere due to electron-atom bremsstrahlung is

$$Q_{\nu\,br} = 3{,}4 \cdot 10^{49} \left[\frac{E_0 \left(\frac{R_0}{R}\right)^{-A_1(\theta)}}{10^{11}} \right]^{5.5} \rho_{10}^2 \cdot \qquad (26)$$

During collapse the electron energy accelerate to $E_e \approx 10^{11}$ *eV,* and the energy of protons increases to $E_p \approx 10^{14}$ *eV* (Kryvdyk, 2010); the proton density increases to $\rho_p = 10^{12}$ *proton/cm³* $\approx 1.7 \cdot 10^{-12}$ *g/cm³*. For such energy and density, at the final stage of collapse *(R₀/R=10⁶)* the neutrino luminosity due to electron-proton collisions in the equatorial regions of the magnetosphere *(θ=π/2)* can reach the extreme value

$$Q_{\nu\,br} \approx 3.3 \cdot 10^{18} \, \frac{Erg}{cm^3 \cdot sec} . \qquad (27)$$

3.2. Neutrino radiation by Urca processes in the magnetosphere

For the magnetosphere of a collapsing star which consists of electrons, positrons, protons and neutrons, the particular interest is focused on the effects of the electron capture on protons, as well as that one of the positron capture by the neutron reaction – the so-called Urca-process:

$$e^- + p \rightarrow n + \nu_e; \qquad\qquad (28)$$
$$e^+ + n \rightarrow p + \overline{\nu}_e .$$
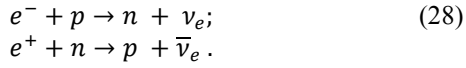
The last Urca-processes are the main processes in the environment with nuclei of small density. The neutrino luminosity for Urca-processes is the following (Qian & Woosley, 1996):

$$Q_{\nu\,URCA} = 9.0 \cdot 10^{31} T_{11}^6 \, \rho_8 , \qquad\qquad (29)$$

where temperature $T_{11} = T/10^{11} K$, $\rho_8 = \rho/10^8 \, g/cm^3$ is the baryon density in the magnetosphere.

If energy E is measured in eV, we obtain

$$Q_{\nu\,URCA} = 2.2 \cdot 10^{56} E_{11}^6 \, \rho_8 , \qquad\qquad (30)$$

where $E_{11} = E/10^{11} eV$.

The neutrino luminosity for Urca-processes greatly depends on the energy of particles. The energy of particles grows very quickly during collapse; thus, Urca-processes will play a significant role in the neutrino generation in the magnetosphere. The neutrino luminosity in the magnetosphere for Urca-process changes during collapse as

$$Q_{\nu\,URCA} = 2.2 \cdot 10^{56} \left[\frac{E_0\left(\frac{R_0}{R}\right)^{-A_1\,(\theta)}}{10^{11}} \right]^6 \rho_8 . \quad (31)$$

At the final stages of the collapse ($R_0/R = 10^6$) in the equatorial regions of the magnetosphere ($\theta = \pi/2$) the protons can accelerate to energies $E_p \leq 10^{14} \, eV$, and the magnetosphere density grows up to $\rho_p = 10^{12} \, proton/cm^3 = 10^{-12} g/cm^3$. If in the magneto-sphere the electrons capture on protons with energy $E_p \leq 10^{14} \, eV$, then neutrino will be produced with the speed

$$Q_{\nu\,URCA} \leq 2.2 \cdot 10^{56} \, \frac{Erg}{cm^3 \cdot sec} . \qquad (32)$$

This is a very powerful flow of neutrinos, which will be rapidly frozen in the magnetosphere during gravitational collapse.

3.3. Neutrino generation due to of electron braking radiation in a strong magnetic field

Neutrinos can be also produced due to synchrotron radiation by electrons accelerated in the strong magnetic field. The neutrino luminance for this process for a relativistic degenerate electron is as follows (Canuto et al., 1970; Fassio-Canuto, 1969; Landstreet, 1967):

$$Q_{\nu\,eB} = \begin{cases} 3 \cdot 10^{-44} B_8^6 T_7 \rho^4 \,, for \, B_8 \, \rho^{\frac{2}{3}} \leq 8 \cdot 10^6 \, T_7, \\ 4 \cdot 10^{-7} B_8^{\frac{2}{3}} T_7^{\frac{19}{3}} \rho^{\frac{4}{9}}, for \, B_8 \, \rho^{\frac{2}{3}} \geq 8 \cdot 10^6 \, T_7, \end{cases} \tag{33}$$

where $B_8 = B/10^8$.

For magnetosphere of collapsing stars at the final stage of gravitational collapse the magnetic fields are $B =$ $10^{12} G$, electron energy is $E_e \leq 10^{12} eV$, the electron density is

$$\rho_e = 10^{12} \, electron/cm^3 = 9 \cdot 10^{-16} g/cm^3 .$$

For such magnetosphere the values $B_8 \, \rho^{\frac{2}{3}} \approx 10^{-6}$; $8 \cdot 10^6 T_7 \approx 6 \cdot 10^{16}$. As follows from this the estimation, $B_8 \, \rho^{\frac{2}{3}} \ll 8 \cdot 10^6 T_7$. Therefore, the extreme neutrino luminance for electron braking radiation

$$Q_{\nu\,eB} = 3 \cdot 10^{-44} B_8^6 T_7 \rho^4 \approx 3.3 \cdot 10^{-71} \, \frac{Erg}{cm^3 \cdot sec} . \quad (34)$$

This value is very small; hence, it does not enable us to examine the neutrino radiation due to the electron braking in the magnetosphere.

3.4. Generation of neutrinos due to photoneutrino processes

Neutrinos will be also produced in the collisions of photons with electrons and positrons in photoneutrino reactions (Ritus, 1961; Chiu & Stabler, 1961; Petrosian et al., 1967):

$$e^\pm + \gamma \rightarrow e^\pm + \nu_e + \overline{\nu}_e .$$
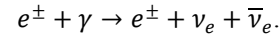
The neutrino luminosity for the photoneutrino processes in hot plasma with is determined as follows (Dutta et al., 2004; Koers & Wijers, 2005; Reynoso et al., 2006)

$$Q_{\nu\,photo} = 1.1 \cdot 10^{31} T_{11}^9 , \qquad\qquad (35)$$

where $T_{11} = T/10^{11} K$.

If the energy E is measured in eV, then

$$Q_{\nu\,photo} = 4{,}2 \cdot 10^{67} E_{11}^9 . \qquad\qquad (36)$$

For magnetospheres of collapsing stars

$$Q_{\nu\,photo} = 4{,}2 \cdot 10^{67} \, [E_0\left(\frac{R_0}{R}\right)^{-A_1\,(\theta)} /10^{11}]^9 . \qquad (37)$$

At the final stage of gravitational collapse ($R_0/R = 6$) the electrons can accelerate to the energy $E_e \leq 10^{11} eV$. The extreme neutrino luminosity for photoneutrino processes for such hot plasma in the equatorial regions the magnetosphere ($\theta = \pi/2$) is

$$Q_{\nu\,photo} \leq 4{,}2 \cdot 10^{67} \, \frac{Erg}{cm^3 \cdot sec} , \qquad (38)$$

This value is very big, so we can make conclusions about strong cooling magnetosphere due to neutrino emission due to photoneutrino processes in magnetosphere during collapse.

3.5. Generation of neutrino-antineutrino pairs by plasmon decay

When a photon moves through ionized gas, a virtual electron-hole pair (plasmon) will appear. This plasmon decays into neutrino-antineutrino pairs

$$\Gamma \to \nu_e + \overline{\nu}_e. \tag{39}$$

The neutrino luminosity for such process is the following (Ratcovich et al., 2003; Koers and Wijers, 2005; Reynoso et al., 2006):

$$Q_{\nu\,plasma} = 7.1 \cdot 10^{26} T_{11}^9. \tag{40}$$

Replacing the temperature *T (K)* on energy *E(eV)*, we obtain

$$Q_{\nu\,plasma} = 2.7 \cdot 10^{63} E_{11}^9. \tag{41}$$

For magnetospheres of collapsing stars

$$Q_{\nu\,plasma} = 2.7 \cdot 10^{63} \left[E_0 \left(\frac{R_0}{R} \right)^{-A_1(\theta)} / 10^{11} \right]^9 \tag{42}$$

The electrons can accelerate in magnetosphere to the energy $E_e \leq 10^{11} eV$.

The extreme neutrino luminosity for plasmon decay in the equatorial regions of the magnetosphere ($\theta=\pi/2$) at the final stage of gravitational collapse ($R_0/R=6$) is

$$Q_{\nu\,plasma} \leq 2.7 \cdot 10^{63} \frac{Erg}{cm^3 \cdot sec}. \tag{43}$$

3.6. Formation of neutrino-antineutrino pairs in annihilation of electron-positron pairs

As follows from section 3, large number of electron-positron pairs will be generated in the magnetosphere of a collapsing star. During the annihilation of these pairs neutrino pairs can be formed (Chiu and Stabler, 1961; Chiu, 1961; Chiu and Morrison, 1960):

$$e^+ + e^- \to \nu_e + \overline{\nu}_e.$$

The neutrino luminosity for this process as follows (Itoh et al., 1989; Koers & Wijers, 2005; Reynoso et al., 2006)

$$Q_{\nu\,pair} = 3.6 \cdot 10^{33} T_{11}^9. \tag{44}$$

By replacing the temperature on energy *E(eV)*, we obtain

$$Q_{\nu\,pair} = 1.37 \cdot 10^{70} E_{11}^9. \tag{45}$$

For magnetospheres of collapsing stars we obtain

$$Q_{\nu\,pair} = 1.37 \cdot 10^{70} \left[E_0 \left(\frac{R_0}{R} \right)^{-A_1(\theta)} / 10^{11} \right]^9. \tag{46}$$

The extreme neutrino luminosity for plasmon decay in the equatorial regions of the magnetosphere ($\theta=\pi/2$) at the final stage of gravitational collapse ($R_0/R=6$) due to annihilation of electrons and positrons with the energy $E_{e\pm} = 10^{11} eV$ is

$$Q_{\nu\,pair} = 1.37 \cdot 10^{70} \frac{Erg}{cm^3 \cdot sec}. \tag{47}$$

3.7. Generation of neutrino by mesons decay

If the plasma temperature exceeds $6 \cdot 10^{11} K$ ($E = 50$ *MeV*), in the thermal radiation field of stars, neutrinos can be generated due to meson decay in the magnetosphere (Arnett, 1967):

$$\pi^\pm \to \mu^\pm + \nu_\mu/\bar{\nu}_\mu, \tag{48}$$
$$\mu^\pm \to e^\pm + \nu_e/\bar{\nu}_e + \nu_\mu/\bar{\nu}_\mu.$$

The neutrino luminosity for μ-meson decay is the following (Hansen, 1968):

$$Q_{\nu\,\mu} = 4.32 \cdot 10^{38} T_{11}^3 \ \text{for } 50 \leq T_9 \leq 500. \tag{49}$$

If energy *E* is in *eV,* then

$$Q_{\nu\,\mu} \approx 6.74 \cdot 10^{50} E_{11}^3 \tag{50}$$

For magnetospheres of collapsing stars

$$Q_{\nu\,photo} = 6.74 \cdot 10^{50} \left[E_0 \left(\frac{R_0}{R} \right)^{-A_1(\theta)} / 10^{11} \right]^3. \tag{51}$$

The formation of π-mesons is possible only for very high-energy protons (over 290 MeV). These protons will accelerate in a variable magnetic field of the magnetosphere of a collapsing star.

At the final stage of collapse the proton energy *E* can accelerate to 10^{14} eV; therefore, the neutrino luminosity for μ-meson decay in magnetosphere can increase to the value

$$Q_{\nu\,\mu} \approx 6.74 \cdot 10^{59} \frac{Erg}{cm^3 \cdot sec} \tag{52}$$

4. Neutrino absorption and scattering in magnetosphere during collapse

Neutrino are absorbed and scattered due to the following processes:

1. $e^\pm$-neutrino scattering: $\nu_i + e^\pm \to \nu_i + e^\pm$;
2. Absorption neutrino by neutron: $\nu_e + n \to p + e^-$;
3. Absorption antineutrino by proton: $\overline{\nu}_c + p \to n + e^+$.

Here we assume that all the particles are non-degenerate.

4.1. Electron and positron scattering

The cross-section neutrino scattering of electrons in a plasma is the following (Tubbs & Schramm, 1975):

$$\sigma_{\nu e} = \frac{3 G_F^2 \hbar^2 c^2}{2\pi} \left[(c_V + c_A)^2 + \frac{1}{3}(c_V - c_A)^2 \right] (kT) E_\nu. \tag{53}$$

Where

$$c_V = 1/2 + 2\sin^2 \theta_W,$$
$$c_A = 1/2; \ \sin^2 \theta_W = 0.22.$$
$$G_F^2 \hbar^2 c^2 = 5.3 \cdot 10^{-44} \ cm^2 MeV^{-2}.$$

The average thermal neutrino distribution $\langle E_\nu \rangle = 3.15$ kT. It applies to the electron-neutrinos, which interact with electrons through both the charged and neutral current.

The neutrino mean free path due to combined electron-positron scattering as follows from (Koers, 2005)

$$\lambda^{-1}(v_i, e^\pm) = \sigma(v_i, e^\pm)n_{e^-}.$$

Because the electron and positron density scales as T^3, the pass length is proportional to T^5 .

For magnetospheres of collapsing stars with the electron energy $E_e \leq 10^{11}$ eV and electron density $\rho_e = 10^{12}$ $electron/cm^3 = 9 \cdot 10^{-16} g/cm^3$ the neutrino mean free path due to combined electron-positron scattering is

$$\lambda(v_i, e^\pm) \leq 10^{14} cm. \tag{54}$$

4.2. Neutron and proton absorption

Electron-neutrinos and antineutrinos can be absorbed by neutrons and protons through the charged interaction. The cross-section is (Tubbs & Schramm, 1975)

$$\sigma_{vp} = \frac{G_F^2 \hbar^2 c^2}{\pi}(1 + 3\alpha^2)E_\nu^2 g(E_\nu).$$

where

$$g(E_\nu) = \left(1 \pm \frac{Q}{E_\nu}\right)\left[1 \pm 2\frac{Q}{E_\nu} + \frac{Q^2 - (\pm m_e^2)}{E_\nu^2}\right]^{1/2}$$

where α = -1.26 is the nuclear axial coupling coefficient and Q = 1.3 MeV is the neutron-proton mass difference. The positive sign applies to neutrino capture on neutrons, the negative sign to antineutrino capture on protons.

The pass length for neutrino-proton scattering is

$$\lambda^{-1}(v_i, p) = \sigma(v_i, p)(0.5n_p)$$

This value is proportional to T^2 .

For magnetospheres of collapsing stars with proton energy $E \leq 10^{14}$ eV and proton density $\rho_e = 10^{12}$ $proton/cm^3$ the neutrino mean free path due to combined electron-positron scattering is

$$\lambda(v_i, p) \leq 10^2 cm. \tag{55}$$

As follows from Egs. (54) and (55), $\lambda(v_i, e^\pm) \gg \lambda(v_i, p)$.

Therefore, electron-neutrinos and antineutrinos will be absorbed in the magnetosphere by neutrons and protons through the charged interaction.

Neutrinos will be absorbed in the magnetosphere due to their interaction with matter. The interaction cross-section for electron neutrino and muon neutrinos with the substance is very small and is approximately 10^{-44} cm^2 for neutrinos with energies 1 MeV. The loss rate of neutrino due to scattering on electrons, protons or neutrons is (Lattimer et al., 1991; Koers & Wijers, 2005):

$$P_{ve} \approx 9.1 \cdot 10^{-35} N_e N_\nu T_9^2 \ [s^{-1} cm^{-3}],$$
$$P_{vp} \approx 1.5 \cdot 10^{-6} N_p N_\nu T_9^5 \ [s^{-1} cm^{-3}], \tag{56}$$

where

$$N_\nu = 7.65 \cdot 10^{27} T_9^3 \tag{57}$$

is a number of neutrino in the unit of volume, N_e is a number of electrons, and N_p is a number of protons or neutrons.

The main part neutrino will be absorbed in the magnetosphere on protons and neutrons. By substituting (57) for (56) and replacing temperature $T(K)$ on energy $E(eV)$, we obtain the rate of neutrino scattering on protons or neutrons

$$P_{vp} \approx 3.77 \cdot 10^{69} N_p E_{11}^8 \ , \tag{58}$$

where $E_{11} = E/10^{11} \ eV$.

For magnetospheres of collapsing stars

$$P_{vp} \approx 3,77 \cdot 10^{69} N_p \left[E_0 \left(\frac{R_0}{R}\right)^{-A_1(\theta)}/10^{11}\right]^8. \tag{59}$$

5. Numerical evaluation of neutrino luminosity in the magnetosphere of a collapsing star

As follows from the previous sections, in the magnetosphere of a collapsing star the neutrino flux will be generated due to various mechanisms. Neutrinos can go out of the magnetosphere. As a result, this magnetosphere loses its energy. The rate of energy loss due to neutrino luminosity for different mechanisms can be determined by formulae (14), (16), (20), (22), (24), (26) and (29). The most neutrino will be generated in the magnetosphere of a collapsing star due to the pair annihilation. Therefore, the neutrino luminosity in the magnetosphere of a collapsing star can be written down as

$$Q_\nu = Q_{\nu\,pair} = 1.37 \cdot 10^{70} . \tag{60}$$

The neutrino luminosity from the whole magnetosphere of a collapsing star can be obtained by integrating the specific neutrino luminosity for the whole magnetosphere:

$$L_\nu = \int Q_\nu \, dV , \tag{61}$$

where $dV-$ the volume element of magnetosphere.

As neutrinos do not interact practically with magnetic fields, their distribution in the magnetosphere is spherically symmetric. For such case

$$dV = 4\pi r^2 dr. \tag{62}$$

Substituting (60) and (62) into (61) and integrating by volume within $R \leq r \leq R_m$, we obtain the full neutrino luminosity for the magnetosphere of a collapsing star

$$L_\nu \approx 8 \cdot 10^{70} (R_m - R)^3 . \tag{63}$$

Here R is the radius of star; R_m is the magnetosphere radius of ($R \leq R_m \leq r$).

This formula allows to determine the full neutrino luminosity in the magnetosphere.

For regions near surface of collapsing stars ($R_m \geq R$)

$$L_v \geq 8 \cdot 10^{70} \, Erg/sec. \tag{64}$$

As we can see, the magnetospheres of collapsing stars are the very powerful sources of neutrinos, which are generated by the nuclear reactions and the annihilation of electron-positron pairs. These neutrinos will go out of the magnetosphere thereby cooling it.

5. Conclusion

The primary protons and electrons are accelerated in the magnetosphere of a collapsing star to relativistic energies during gravitational collapse. Later on, the secondary charged particles (electrons, positrons, protons and mesons), neutrons, neutrinos and gamma photons will be generated in the magnetosphere of a collapsing star due to different interaction between the particles and fields. The charged secondary particles will be also accelerated in the increasing magnetic field, generating the cascade charged particles, neutrons, neutrinos and photons. As results of these processes, the magnetosphere of the collapsing star will be formed. This magnetosphere consists of protons (p), electrons (e), positrons (e$^+$), neutrons (n), mezons (π, μ), neutrinos (v), and photons (γ).

Being generated in the magnetosphere of a collapsing star, some part of neutrinos will escape the magnetosphere thereby cooling magnetosphere with very high rate. For the subsequent existence of the energy balance in the magnetosphere, the continuous energy flow from the star into the magnetosphere is required. This energy flow can be provided by stellar winds, accelerating in strong magnetic fields during a stellar collapse.

Some part of particles and neutrinos go out from the magnetosphere in the interstellar medium. This means that magnetospheres of stars during their gravitational collapse are the powerful sources of particles and neutrinos in our Galaxy and other galaxies. The contribution of these sources in the general flux of cosmic rays and neutrinos will be investigated in the further study.

References

Alecian E., et al.: 2008, *Astron. and Astroph.*, **481**, L99.
Arnett W. D.: 1967, *Canad. J. Phys.*, **45**, 1621.
Arnett W. D.: 1979, *Gravitational collapse of evolved stars as a problem in physics.In: "Sources of gravitational radiation"*. Ed. Smarr. Gambridge, pp. 163-174.
Baiotti L., Giacomazzo B., Rezzolla L.: 2008, *Phys. Rev. D*, **78**, id. 084033.
Bouret J.- C. et al. : 2008, *MNRAS*, **389**, 75.
Braaten E., Segel D.: 1993, *Phys. Rev. D*, **48**, 1478.
Bruenn S.W.: 1985, *Ap. J. Supl. Ser.*, **58**, 771.
Canuto V. et al.: 1970, *Phys. Rev. D.*, **2**, 281.
Cherepashchuk A.M.: 2003, *Physics Uspekchi*, **46**, 335.
Chevalier R. A.: 2005, *Ap. J.*, **619**, 839.
Chiu H.Y., Morrison P.: 1960, *Phys. Rev. Lett.*, **5**, 573.
Chiu H.Y.: 1961, *Phys. Rev.*, **123**, 1040.

Chiu H.Y., Salpeter E.E.: 1964, *Phys. Rev. Lett.*, **12**, 413.
Chiu H.Y. Stabler R.C.: 1961, *Phys. Rev.*, **122**, 1317.
Dicus D. A.: 1972, *Phys. Rev. D*, **6**, 941.
Donati J.F. et al: 2002, *MNRAS*, **333**, 55.
Donati J.F. et al.: 2001, *MNRAS*, **326**, 1265.
Dutta S.T., Ratkovich S., Prakash M.: 2004, *Phys. Rev. D*, **69**, id. 023005.
Eldridge J.J., Tout C.A.: 2004, *MNRAS*, **353**, 87.
Fassio-Canuto L.: 1969, *Phys. Rev.*, **187**, 2141.
Friman B.L., Maxwell O.V.: 1979, *Ap. J.*, **232**, 541.
Ginzburg V.L., Ozernoy L.M.: 1964, *Zh. Exper. i Theor. Fiz.*, **47**, 1030.
Goldreich P., Julian :1969, *Ap. J.*, **157**, 869.
Hajakawa S.: 1978a, *Cosmic ray physics. Part 1. Nuclear aspects*, Mir, Moskva.
Hajakawa S.: 1978b, *Cosmic ray physics. Part 2. Astrophysical aspects*, Mir, Moskva.
Hansen C. J.: 1968, *Astrophys. Space Sci.*, **1**, 499.
Heitel W.: 1954, *The quantum theory of radiation*, Oxford University Press, Oxford.
Hubrig S. et al: 2013, *Astron. and Astrophys.*, **551**, id.A33, 13 pp.
Itoh N. et al: 1989, *Ap. J.*, **339**, 354.
Jordan S.: 2009, *Proc. IAU Symposium*, **259**, 369.
Kepler S.O. et al.: 2013, *MNRAS*, **429**, 2934.
Koers H.B.J., Wijers R.A.M.J.: 2005, *MNRAS*, **364**, 934.
Kryvdyk V.: 1999, *MNRAS*, **309**, 593.
Kryvdyk V.: 2001, *Adv. Space Res.*, **28**, 463.
Kryvdyk V.: 2003, *Adv. Space Res.*, **31**, 1315.
Kryvdyk V.: 2004, *Adv. Space Res.*, **33**, 484.
Kryvdyk V.: 2010, *Kinem. Phys. Cel. Bodies*, **25**, 277.
Landstreet J. D.: 1967, *Phys. Rev.*, **153**, 1372.
Lattimer J.M. et al.: 1991, *Phys. Rev. Lett.*, **66**, 2701.
Leng K.R.: 1974, *Astrophysical formulae*, Springer-Verlag, Berlin-Heidelberg-New York.
Munakata H., Kohyama Y., Itoh N.: 1985, *Ap. J.*, **296**, 197.
Petrosian G., Beaudet V., Salpeter E.E.: 1967, *Phys. Rev.*, **154**, 1445.
Pontekorvo B.M.: 1959, *JETP*, **36**, 1615.
Qian Y.Z., Woosley S.E.: 1996, *Ap. J.*, **471**, 331.
Ratkovic S., Dutta S.I., Prakash M.: 2003, *Phys. Rev. D*, **67**, id. 123002.
Reynoso M.M., Romero G.E., Sampayo O.A.: 2006, *Astron. Astrophys.*, **454**, 11.
Ritus V. I.: 1961, *JETP*, **41**, 1285.
Ruderman M.A., Sutherland: 1975, *Ap. J.*, **196**, 51.
Sturrock P. A.: 1971, *Ap. J.*, **164**, 529.
Tubbs D.L., Schramm D.N.: 1975, *Ap. J.*, **201**, 467.
Wade G.A. et al.: 2014, *Proc. IAU Symp.*, **302**, 265.
Wooslej S.E., Heger A.: 2006, *Ap. J.*, **637**, 914.
Zeldovich J.B., Novikov I.D.: 1971, The*ory of gravity and stellar evolution*. Nauka, Moscow (in Russian).

CHARACTERISTICS OF THE PERIOD CHANGES IN MIRA-TYPE VARIABLES

V.I. Marsakova

I.I. Mechnikov Odessa National University
Odessa, Ukraine
vmarsakova@mail.ru

ABSTRACT. The period changes in a sample of Mira-type variables were analysed and classified. Characteristics of the long-term cyclicity in the period changes were obtained.

Key words: Stars: LPVs, Mira-type, period changes.

Introduction

The Mira Ceti stars are long-period variables whose light curves are not only distinguished by the periods of variability, but also exhibit significant cycle-to-cycle alterations as opposed to the corresponding light curves of classical pulsating stars (e.g., δ Cephei or RR Lyrae variables). The comprehensive survey of the properties of Mira variables and similar long-period variables was conducted by Kudashkina (2003). In particular, it was reported that many Mira-type variables exhibited changes in their periods. Zijlstra & Bedding (2002) defined continuously changing periods, sudden changes, and meandering Miras (whose periods change to some extent with time, followed by a return to the previous period). Our study resulted in more detailed classification of the period changes.

We used observation data taken from the French Association of Variable Star Observers (AFOEV), Variable Star Observers League of Japan (VSOLJ) and American Association of Variable Star Observers (AAVSO), which enabled us to study the target stars' variability over a period of about 100 years.

The methods and detailed procedures applied in our analysis are given in Andronov & Marsakova (2006). Some methods had been discussed earlier in other studies, in particular: "asymptotic parabolae" and "running parabolae" fittings were applied for determination of the characteristics of extrema (Andronov, 1997; Marsakova & Andronov, 1996); trigonometric polynomial was employed to obtain parameters of the mean light curves (Kudashkina & Andronov, 1996); the light curves were subjected to wavelet analysis and running sine approximation to study the period and amplitude stability (Andronov, 2003; Chinarova, 2010; Andronov & Chinarova, 2013).

To obtain variations in individual cycle parameters with time, in this research we have analysed a sample of 56 variables classified as either the Mira type or intermediate type which is between semi-regular (SRa) and Mira classes. We examined variations in such parameters as periods, amplitudes, the light curve asymmetry, the mean luminosity (averaged over individual pulsation cycles), parameters of humps on the ascending branches, etc. as described in Andronov &

Marsakova (2006). To analyse and classify the period changes, we used the O-C curves obtained using moments of maxima. The individual cycle characteristics for the majority of target stars are listed in catalogues (Marsakova & Andronov, 1998; Marsakova & Andronov, 2000c).

The research results allow us to define the following types of period changes:

1. Small irregular period changes. Small and moderate amplitudes of the O-C curve can be seen in Fig. 1.
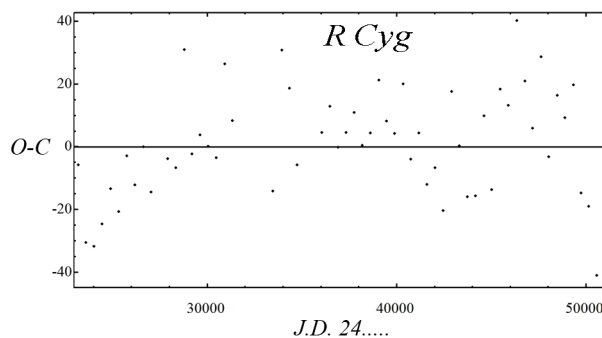
Figure 1: The R Cyg O-C curve (small irregular period changes)

2. Switchover between similar period lengths producing the saw-tooth O-C curve. Many Mira variables show such period changes all the time or just over certain time intervals. Such evolution is cyclic rather than strongly periodic. The corresponding O-C curve is shown in Fig. 2. Characteristics of these period changes (including mean pulsation periods, as well as the O-C variation periods and amplitudes) are given in Table 1. Accounting for the findings of the study by Marsakova & Andronov (2007), it can be noted that there are no humps on the ascending branches of the light curves of the indicated variable stars; and the proportion of pulsation cycles with short increments on the ascending branches are rather small.
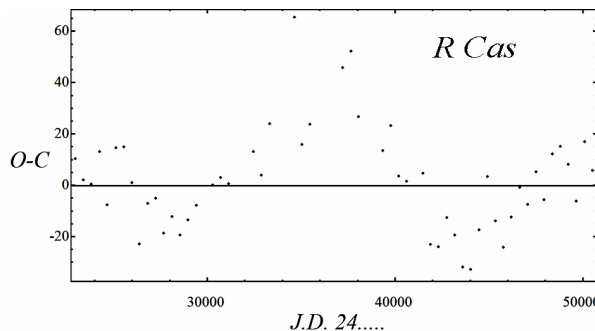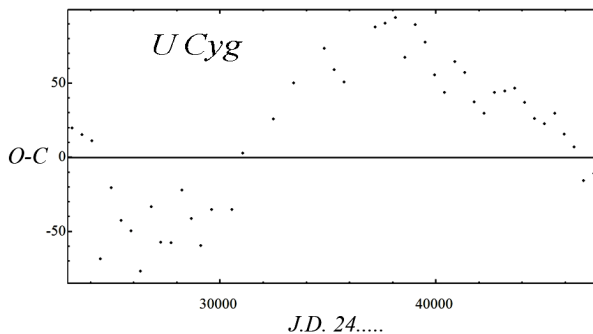

Figure 2: The R Cas saw-tooth O-C curve

Table 1: The period changes' characteristics for the variables with the most distinct saw-tooth O-C curves.

Variable	Pulsation period	Periods of the O-C variation	Amplitude of the O-C main wave
X Aur	164	20520±400	32±2
T Her	165	9000±200	10±1
RS Her	219	12600±260	17±1
R Boo	224	11340±195	11±1
R Dra	246	12500±260	11±1
X Oph	332	16000±500	24±3
χ Cyg	409	15400±350	15±2
R Cas	430	16600±300	20±2

3. Smooth cyclic period changes on the timescale of ~17000–22000 days.

These changes were discussed in Marsakova & Andronov (2013) by the example of three Mira variables. The most evident smooth cyclic changes in period were reported in T Cephei (also see Marsakova & Andronov, 2000b). Alternative example is shown in Fig. 3. These period changes are similar to those described in the previous paragraph, but generally they have comparatively longer mean cycle length and higher amplitude of the O-C variations (see Table 2). Moreover, for some variables there are noticeable humps on the light curve ascending branches, which can transform to double-peak maxima over the period evolution course (Marsakova & Andronov, 2013).

Figure 3: The U Cyg smooth cyclic O-C curve

Table 2: The period changes' characteristics for the variables with the most distinct smooth cyclic changes.

Variable	Pulsation period	Period of the O-C variation	Amplitude of the O-C main wave	Presence of humps on the ascending branch
W Lyr	197	23900±1400	25±3	
V Cas	229	22600±230	52±1	
R UMA	302	23000±540	25±1	
S UMi	328	14600±440 20600±500	29±3 26±2	+
U UMi	331	17600±200	50±2	+
Z Sco	348	22500±700	48±5	
T Cam	374	22500±550	52±4	+
T Cep	388	19000±180	82±2	+
T Cas	445	18700±600	25±3	+
U Cyg	466	23200±800	60±4	

General characteristics of humps on the ascending branches were discussed in Kudashkina & Rudnitskij (1995) and Marsakova & Andronov (2007). The results of the cross-correlation analysis of variations of the T Cep light curve parameters were presented in Marsakova & Andronov (2000b). It was reported that the light curve amplitude and period are strongly correlated while their variations are shifted by 3 cycles; moreover, the amplitude and hump magnitude variations are synchronous.

In Tables 2 and 3, the variables are listed in increasing order of the main pulsation period, but it is clear that the O-C wave cyclicity does no depend on the main period of pulsation.

However, as is obvious, these period changes are not strongly periodic either, and the cyclicity may be disrupted with time.

4. Progressive period changes (continuous ones of the same sign) were found in R Aql, R Hya, W Dra and T UMi (Marsakova & Andronov, 2000a; Marsakova & Andronov, 2006). Such period changes are illustrated with the R Aql O-C curve in Fig. 4. R Aql and R Hya exhibit constantly decreasing periods while W Dra shows slowly increasing period. T UMi has been undergoing abrupt decrease in period since about J.D. 2443000. There are different types of the period changes according to the classification by Zijlstra & Bedding (2002); meanwhile, Wood & Zarro (1981) introduced a helium - shell flash model that explains all such period changes at various stellar core masses and helium - shell flash phases.

It is remarkable that residuals from parabolic approximation of the R Aql O-C curve (the so-called O-C curve of the second order) produce a saw-tooth curve with the period of 18500±260 days (Fig. 5).

Slow decrease in the period was expected by the O-C curve in Y Per, but there is also some influence of the multi-periodicity.
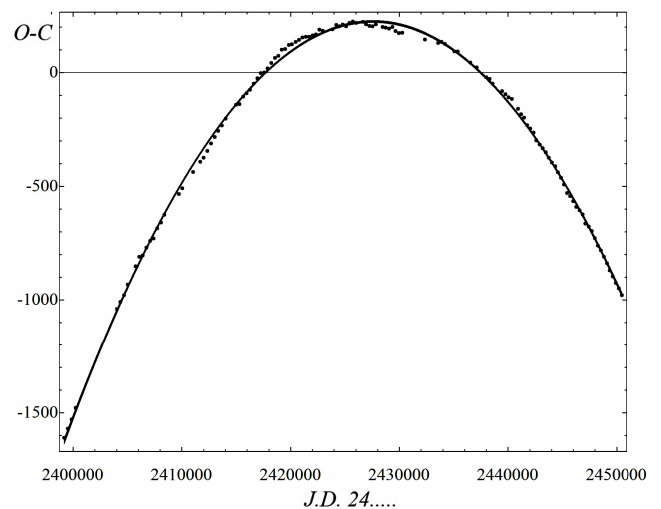

Figure 4: The R Aql O-C curve and its parabolic approximation
(O-C = −13568300 + 11.1786·t − 0.00000230241·t2, where t is measured in J.D.)
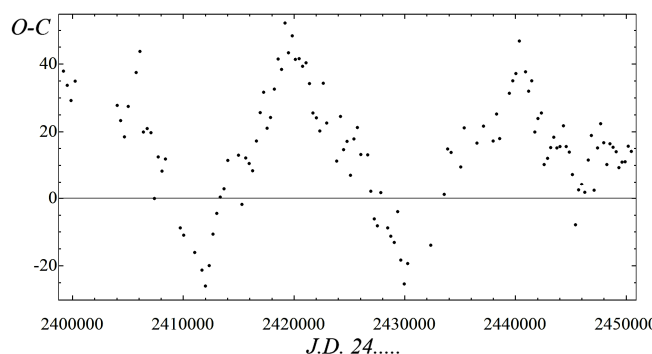
Figure 5: The residuals from parabolic approximation of the R Aql O-C curve (the so-called O-C curve of the second order)

5. Effects of multi-periodicity were discussed in Marsakova (2012), Marsakova & Andronov (2013) and Chinarova (2010). Such influence results in noisy O-C curves and significant decrease in the pulsation amplitude in some time intervals. To detect these effects, it is necessary to carry out thorough analysis of the light curves using various mathematical methods.

Conclusions

Among our sample 56 variable stars 16 variables exhibit small irregular period changes; smooth cyclic period changes are shown in 14 variables; and 11 variables produce saw-tooth O-C curves. There are also 4 variables with progressive period changes and 6 variables subjected to the multi-periodicity effects. We did not succeed in classifying period changes in 5 variables due to poor observation data.

Two critical aspects should be emphasised. Firstly, the effects of multi-periodicity may superimpose on period changes of one of the types (namely, saw-tooth, cyclic or even progressive ones as in Y Per) causing some distortion. Secondly, for the data acquired at the moments of maxima over a very long time interval (as it was made, for instance, by SVO; http://var.astronet.se/mirainfooc.php), it is evident that the O-C curve type may alter with time (but in this case we employed data obtained by different techniques). Thus, the suggested classification is applied to effects rather than variable stars.

The present study is a part of two projects, namely "Inter-Longitude Astronomy" (Andronov et al., 2010) and "Ukrainian Virtual Observatory" (Vavilova et al., 2012).

Acknowledgements. We would like to sincerely thank all amateur observers of variable stars who contribute to the observations of international associations (such as AFOEV, VSOLJ and AAVSO) for their work that made such research possible.

The author is grateful to I.L. Andronov and L.S. Kudashkina for helpful discussions.

References

Andronov I.L.: 1997, Astron. *Astrophys. Suppl.*, **125**, 207.
Andronov I.L., Baklanov A.V.: 2004, *Astronomy School Reports*, **5**, 264, http://uavso.pochta.ru/mcv
Andronov I.L., 2003: *ASP Conference Series*, **229** .391.
Andronov, I. L.:2005: *ASP Conference Series*, **335**, 37.
Andronov I.L. et al.: 2010, *Odessa Astron. Publ.*, **23**, 8.
Andronov I.L., Chinarova L.L.: 2013, *Częstochowski Kalendarz Astronomiczny-2014.* P. 171. (arXiv:1308.1129)
Andronov I.L., Marsakova V.I.: 2006, *Astrophysics*, **49**, 370.
Chinarova L.L.: 2010, *Odessa Astron. Publ.*, **23**, 25.
Kudashkina L.S.: 2003, *Kinematics and Physics of Celestial Bodies*, **19**, 193.
Kudashkina L.S., Andronov I.L.: 1996, *Odessa Astron. Publ.*, **9**, 108.
Kudashkina L. S., Rudnitskij G. M.: 1995, *Odessa Astron. Publ.,* 7, 63.
Marsakova, V.I.: 1999, *Odessa Astronomical Publication*, **12**, 205.
Marsakova V.I., Andronov I.L.: 1996, *Odessa Astron. Publ.*, **9**, 127.
Marsakova V.I., Andronov I.L.: 1997, *Kinematics and Physics of Celestial Bodies*, **13**, № 6, 49.
Marsakova V.I., Andronov I.L.: 1998, *Odessa Astron. Publ.*, **11**, 79.
Marsakova V.I., Andronov I.L.: 2000a, *ASP Conference Series*, **203**, 130.
Marsakova V.I., Andronov I.L.: 2000b, *ASP Conference Series*, **203**, 131.
Marsakova V.I., Andronov I.L.: 2000c, *Odessa Astron. Publ.*, **13**, 83.
Marsakova, V.I., Andronov, I.L: 2006, *Astrophysics*, **49**, 506.
Marsakova, V.I., Andronov, I.L.: 2007, *Astrophysics*, **50**, 99.
Marsakova V.I., Andronov I.L., 2012, *Odessa Astron. Publ*, **25**, № 1, 60.
Marsakova V.I., Andronov I.L.: 2013: *Odessa Astron. Publ*, **26**, № 1, 78.
Marsakova V.I., Andronov I.L., 2013: *Częstochowski Kalendarz Astronomiczny-2014*, P. 273. (arXiv:1310.2412)
Vavilova I.B., et al.: 2012, *Kinem. Phys. Celest. Bodies,* **28**, 85.
Wood P.R., Zarro D.M.: *Astrophys. J.*, 1981, **247,** 247.
Zijlstra, A.A. & Bedding, T.R.: 2002, *Journal AAVSO*, **31**, 2.

DETERMINATION OF THE POSITION AND VELOCITY OF THE NATURAL SATELLITE'S SHADOW ON THE ILLUMINATED PART OF THE SPHERICAL PLANET'S VISIBLE DISK

V.V. Mikhalchuk

The Odessa National Maritime Academy
Didrikhsona str., 8, 65029, Odessa, Ukraine, *vmihalchuk@mail.ru*

ABSTRACT. This study introduces a simple analytical method for determination of the rectangular coordinates of the natural satellite's (or the moon's) shadow cast on the illuminated part of the spherical planet's visible disk and projected onto the sky plane, as well as the rates of change of those coordinates when the shadow is moving. The analytical method's formulae, derived in two approximations of the Earth's and the Sun's positions relative to the planet's rotation axis, provide an accurate solution for each approximation at any phase angle values that enables to apply them to simulate processes associated with the satellite's shadow passing across the illuminated part of the planet's visible disk.

Key words: natural satellite, moon, shadow.

1. Introduction

The simulation of the planet satellites' motion provides for the observations of their exact positions. When a natural satellite is orbiting the planet, a geocentric observer can see the satellite's position in orbit at a given instant projected onto the geocentric sky plane relative to the planet's visible disk limb, which is the planets' projection onto the same plane. The geocentric sky plane is perpendicular to the line connecting the centres of the planet and the Earth.

Illumination of the planet and its satellite by the Sun specifies the line that connects the centres of the planet and the Sun. The planet and its natural satellite cast their shadows in the same direction. The satellite's position relative to the planet's shadow and the satellite's shadow position with respect to the planet's disk are determined for a heliocentric observer who can see the satellite's position in orbit at a given instant projected onto the heliocentric sky plane with relation to the planet's terminator, which is the planet's projec-

tion onto the same plane. The heliocentric plane of the sky is perpendicular to the line connecting the centres of the planet and the Sun.

When the satellite passes near those two lines (i.e. the planet-Earth and the planet-Sun lines) while orbiting the planet, the satellite-planet phenomena can be observed from the Earth's centre. At that an occultation of the satellite by the planet's disk is observed close to superior geocentric conjunctions, and the satellite's transit in front of the planet's disk can be seen close to inferior geocentric conjunctions. The satellite's eclipse is observed close to superior heliocentric conjunctions, and the satellite's shadow passing across the planet's disk is seen close to inferior heliocentric conjunctions.

The prediction of phenomena in the satellite systems of different planets is based on the determination of the relative positions of the planet's and each of its satellites' projections onto either of the sky planes (the geocentric or heliocentric ones) (Emel'yanov, 1996; Bureau Des Longitudes, 2001). The phenomena conditions are determined independently for each of those sky planes.

The satellite's shadow passing across the planet's disk when the satellite and its shadow can be observed simultaneously is of special interest. In that case, the determination of both the instant of the satellite's shadow contact with the illuminated part of the planet's disk and the shadow's rectangular coordinates in the heliocentric sky plane is carried out similarly to the method described in (Mikhalchuk, 2007). The natural satellite's shadow projection can be seen by a terrestrial observer in the geocentric plane of the sky; however, the determination of the satellite's shadow rectangular coordinates relative to the planet's visible disk in that plane gets complicated due to the satellite's shadow being projected onto the illuminated part of the spherical planet's surface rather than on the heliocentric sky plane (as it is the case when the contact conditions are estimated). Moreover, due to the influence of the phase and spherical surface curvature, the

motion of the satellite's shadow across the illuminated part of the planet's visible disk differs from that of the satellite's projection onto the heliocentric sky plane.

The target problem can be solved with the numerical method that implies various coordinate conversions; but such a method is very cumbersome and does not give formulae for immediate determination of the satellite's shadow coordinates and their rates of change.

The indicated features of the natural satellite's shadow position and motion across the illuminated part of the planet's visible disk necessitate the development of an analytical method that provides some formulae to immediately transform the satellite's position projected onto the heliocentric sky plane to its shadow's projection onto the geocentric sky plane. The formulae that describe the satellite's shadow position and motion across the planet's visible disk can be applied to easily and accurately approximate not only the shadow's position and velocity, but also its visible size and shape (Mikhalchuk, 2004), which are quite important when conducting physical, astrometric and photometric observations.

The purpose of this study is to determine the position of the spherical planet satellite's shadow in the geocentric sky plane, as well as its rate of change, using the described analytical method.

2.   The determination of the satellite's shadow position on the planet's surface

The formulated problem is solved using the orthographic approximation, i.e. the orthographic limb is the boundary of the planet's visible disk, and the orthographic terminator is the boundary of the illuminated part of the planet's visible disk.

The natural satellite's shadow position on the illuminated part of the planet's visible disk depends on the lighting conditions, i.e. the planet's phase. If the phase angle Φ is nonzero, the position of the satellite's shadow projected onto the geocentric sky plane relative to the planet's visible disk centre does not coincide with the satellite's position projected either onto the same plane or on the heliocentric sky plane.

The planet's orientation in space is specified by the direction of its rotation axis. The apparent position of the planet's rotation axis relative to a terrestrial observer can be defined by two angles, namely the planetocentric declination of the Earth $D_\oplus$ and the angle P of the axis position in the geocentric celestial sphere. The planet's visible disk illuminance relative to a terrestrial observer is defined by the phase angle Φ and the angle Q of the minimum illuminance point position. Those angles are related to the difference $\Delta A = A_\oplus - A_\odot$ of the planetocentric right ascensions of the Earth and the Sun, which can be derived by the

following formula adopted from (Mikhalchuk, 2007a):

$$\tan \Delta A = \frac{\sin \Phi \sin(P - Q)}{\cos \Phi \cos D_\oplus + \sin \Phi \sin D_\oplus \cos(P - Q)}. \quad (1)$$

The formula that connects angles Φ, P, Q and $D_\oplus$ (the planet's physical ephemerides) with the planetocentric declination of the Sun $D_\odot$ is given in (Mikhalchuk, 2007a).

To determine the satellite's shadow position observed on the illuminated part of the planet's visible disk, we introduce a rectangular coordinate system (x, y, z), that is oriented relative to the orthographic limb plane (the geocentric plane of the sky). The origin of this coordinate system is in the centre of the planet's geometric disk, and the X and Y axes lie in the sky plane. The Y-axis is oriented along the planet's rotation axis projected onto the sky plane towards its North Pole; the X-axis is oriented eastward; and the Z-axis is oriented along the line of sight outward from the Earth. Let us take the planet's equatorial radius a as a unit for measuring distance. The satellite's apparent position in the geocentric sky plane at a given instant is specified by the rectangular coordinates x and y, and the apparent position of its shadow is specified by the rectangular coordinates x_s and y_s. The velocity V of the planet's satellite motion in the geocentric sky plane close to the satellite's inferior geocentric conjunction has projections onto the X and Y axes as such $\dot{x}$ and $\dot{y}$, respectively; and the projected velocity V_s of its shadow's motion is specified by $\dot{x}_s$ and $\dot{y}_s$. The rectangular coordinates x and y, as well as their rates of change $\dot{x}$ and $\dot{y}$, can be defined by formulae given in (Mikhalchuk, 2007).

Let us introduce another rectangular coordinate system (x', y', z') that is oriented relative to the orthographic terminator plane (the heliocentric plane of the sky). The origin of this coordinate system is in the centre of the planet's geometric disk that can be observed from the Sun, and the X' and Y' axes lie in the orthographic terminator plane. The Y'-axis is oriented along the planet's rotation axis projected onto that plane towards the North Pole, the X'-axis is oriented eastward; and the Z'-axis is oriented along the line of sight outward from the Sun. The satellite's rectangular coordinates x' and y' at a given instant specify the satellite's shadow position in the heliocentric plane of the sky, and the position of its shadow on the planet's surface relative to the same plane is determined by the rectangular coordinates x'_s, y'_s and z'_s. The projections of the satellite and its shadow onto the heliocentric plane of the sky coincides, therefore $x'_s = x'$ and $y'_s = y'$. The velocity V' of the planet's satellite motion in the heliocentric sky plane close to the satellite's inferior heliocentric conjunction has projections onto the X' and Y' axes as such $\dot{x}'$ and $\dot{y}'$, respectively. The method for computing the rectangular coordinates x' and y', as well as their rates of change $\dot{x}'$ and $\dot{y}'$, is described

in the study (Mikhalchuk, 2007).

If the planet's satellite is not a close one, i.e. its radius vector r fulfills condition $r \gg a$, its motion projected onto the geocentric and heliocentric sky planes close to its geocentric and heliocentric conjunctions can be deemed uniform, meaning that velocities $\dot{x}$ and $\dot{y}$, as well as $\dot{x}'$ and $\dot{y}'$ are constant.

Hence, based on the known rectangular coordinates x' and y' of the planet's satellite position in the heliocentric sky plane close to its inferior heliocentric conjunction, as well as on their rates of change $\dot{x}'$ and $\dot{y}'$, it is necessary to find the satellite's shadow rectangular coordinates x_s and y_s, as well as their rates of change $\dot{x}_s$ and $\dot{y}_s$.

The methods for accurate solution of the formulated problem, which are initially intended for the spherical planets, can be also applied for its approximate solution for ellipsoid planets. It can be shown that the planet's flattening can be neglected for low ratios $\dfrac{|y'|}{a}$ and $\dfrac{|\dot{y}'|}{V'}$ meaning that the planet is spherical.

As in the general case $x_s'^2 + y_s'^2 + z_s'^2 = x'^2 + y'^2 + z_s'^2 = a^2$, an auxiliary dimensionless coordinate should be introduced to solve the target problem:

$$\zeta' = -\frac{z_s'}{a} = \sqrt{1 - \frac{x'^2 + y'^2}{a^2}}, \qquad (2)$$

this coordinate should always be positive on the planet's side illuminated by the Sun. The auxiliary coordinate $\zeta' = 0$ on the terminator, and $\zeta' = 1$ at the subsolar point. Having this coordinate differentiated with respect to time, its rate of change can be found:

$$\dot{\zeta}' = -\frac{\dot{z}_s'}{a} = -\frac{x'\dot{x}' + y'\dot{y}'}{a^2\zeta'}. \qquad (3)$$

The natural satellite's shadow position relative to the planet's visible disk and its velocity can be defined by transforming the satellite's position projected onto the heliocentric sky plane to its shadow's projection onto the geocentric sky plane.

3. The numerical method for determination of the satellite's shadow position and velocity on the illuminated part of the planet's visible disk

The numerical method enables to find the satellite's shadow rectangular coordinates x_s and y_s in the geocentric sky plane, as well as their rates of change $\dot{x}_s$ and $\dot{y}_s$ by the initial rectangular coordinates of the satellite x' and y' and their rates of change $\dot{x}'$ and $\dot{y}'$ in the heliocentric sky plane. This method can also be implemented with the known formulae for determination of the satellite's shadow position on the illuminated side of the spherical planet (Mikhailov, 1954).
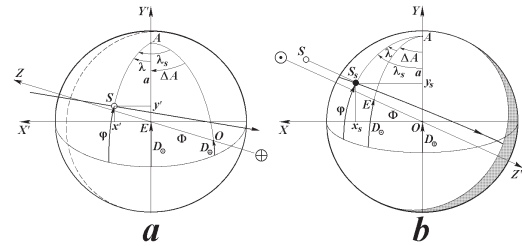
Figure 1: The appearance of the planet, its natural satellite and the satellite's shadow as seen from the Sun (a) and from the Earth (b).

Let us consider the planet's disk appearance as seen from the Sun, i.e. in the heliocentric sky plane (Fig. 1a). The satellite S casts the shadow S_s which cannot be discerned as its position always coincides with the satellite's position. The great-circle arc that bounds the planet's side visible from the Earth, i.e. the planet's light limb projected onto the heliocentric sky plane, is shown with the dotted line.

The numerical method implies that first the transition is made from the satellite's (and its shadow's) coordinates x' and y' projected onto the heliocentric sky plane to non-rotating planetocentric coordinates λ and φ by the known formulae for the oblique orthographic projection (Vakhrameeva, Bugaevskij, Kazakova, 1986). In that coordinate system the longitude λ is reckoned from the planetographic meridian of the subsolar point E westwards of the planet; and the latitude φ is reckoned from the planet's equatorial plane. Then, the planetocentric coordinate system is rotated by the angle ΔA around point E to the subterral point O that specifies the geocentric sky plane orientation. The planet's disk appearance as seen from the Earth, i.e. in the geocentric sky plane, is shown in Fig. 1b. The planetocentric longitude λ_s of the satellite's shadow, which is reckoned from the planet's central meridian passing through point O, is defined by the following formula: $\lambda_s = \lambda + \Delta A$.

And finally, similarly using the known formulae for the oblique orthographic projection, the transition is made from the non-rotating planetocentric coordinates λ_s and φ of the satellite's shadow to its rectangular coordinates x_s, y_s and z_s in the geocentric sky plane.

The transformation of the rates of change in coordinates $\dot{x}_s$, $\dot{y}_s$ and $\dot{z}_s$ is made by a similar way. The numerical method is precise and holds for any phase angle values and any planetocentric declinations of the
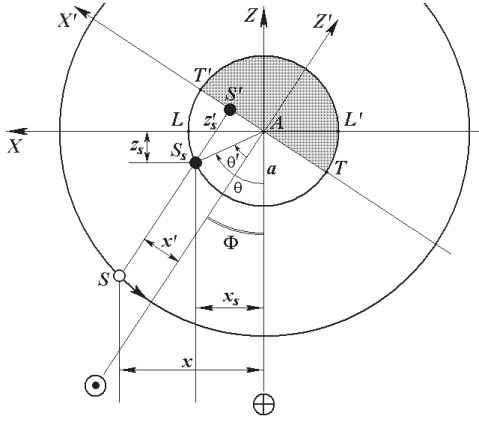
Figure 2: The satellite's shadow position on the planet's surface in its equatorial plane.

Figure 3: The satellite's shadow on the planet's visible disk in the first approximation.

Earth and the Sun. That allows of its applying for the analytical method testing.

4. The analytical method for determination of the satellite's shadow position and velocity on the illuminated part of the planet's visible disk

Let us consider the problem solution in the first approximation when the Earth and the Sun are assumed to be in the planet's equatorial plane. It means that $D_\odot = 0$ and $D_\oplus = 0$. Hence, it follows that $P - Q = \pm 90°$. In all expressions the sign is selected by the following rule: the upper sign corresponds to the situation when the eastern part of the planet's visible disk is illuminated; and the lower sign implies that its western part is illuminated.

The angles Φ and ΔA are in the planet's equatorial plane, hence, according to formula (1) it can be deemed that $\Phi = \pm \Delta A$.

In a special case of the first approximation when the natural satellite S moves true in the planet's equatorial plane: $y' = 0$, $\dot{y}' = 0$ (Fig. 2), its projection S' onto the heliocentric sky plane changes its position uniformly along the X' axis between points T' and T. The satellite's shadow S_s, which can be observed from the Earth, transits through the planet's equator arc between points L and T. The satellite's shadow position on the planet's surface in its equatorial plane is specified by the angles θ and θ' relative to a geocentric and heliocentric observer, respectively. Hence, $x' = a \sin \theta'$, $z'_s = -a \cos \theta'$ and $x_s = a \sin \theta$, $z_s = -a \cos \theta$ where $\theta = \theta' \pm \Phi$.

In more general case when the satellite's path is parallel to the planet's equatorial plane (Fig. 3), $\dot{y}' = 0$, $x' = a \cos \chi' \sin \theta'$, $y' = a \sin \chi'$, $z' = -a \cos \chi' \cos \theta'$

where the angle χ' is equal to the planetocentric latitude of the satellite's shadow relative to the $X'Y'$ plane. Relative to the XY plane the planetocentric latitude of the satellite's shadow is χ, and $\chi = \chi'$ at that. Hence, $x_s = a \cos \chi \sin \theta$, $y_s = a \sin \chi$ and $z_s = -a \cos \chi \cos \theta$. Those expressions are valid even in the more general case when $\dot{y}' \neq 0$, i.e. the natural satellite moves at an arbitrary angle to the planet's equatorial plane.

Taking into account that the auxiliary coordinate ζ' and its rate of change $\dot{\zeta}'$ are defined by formulae (2) and (3), respectively, the rectangular coordinates of the satellite's shadow are as follows:

$$\left.\begin{array}{l} x_s = x' \cos \Phi \pm a\zeta' \sin \Phi \\ y_s = y' \\ z_s = -a\zeta' \cos \Phi \pm x' \sin \Phi \end{array}\right\}, \qquad (4)$$

and their rates of change are the following:

$$\left.\begin{array}{l} \dot{x}_s = \dot{x}' \cos \Phi \pm a\dot{\zeta}' \sin \Phi \\ \dot{y}_s = \dot{y}' \\ \dot{z}_s = -a\dot{\zeta}' \cos \Phi \pm \dot{x}' \sin \Phi \end{array}\right\}. \qquad (5)$$

Simultaneous formulae (4) and (5) hold for any phase angle values.

Let us consider this case in the second approximation when it is only the Sun is in the planet's equatorial plane ($D_\odot = 0$), and the Earth's planetocentric declination $D_\oplus$ can take on different values (Fig. 4).

The angles Φ and ΔA are situated in different planes; therefore, $\theta = \theta' + \Delta A$, and the values of angles Φ and ΔA are linked by the following expression:

$$\cos \Phi = \cos D_\oplus \cos \Delta A. \qquad (6)$$

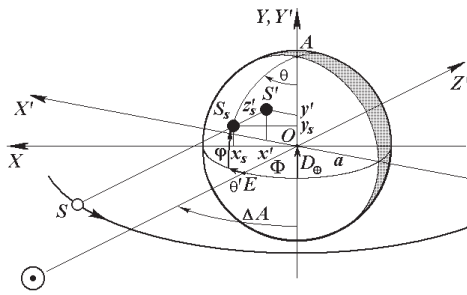The sign of angle ΔA in expression (6) is the same as in $\sin(P - Q)$.

Figure 4: The satellite's shadow on the planet's visible disk in the second approximation.

Figure 5: The satellite's shadow coordinate and velocity in a special case in the first approximation.

Therefore, the rectangular coordinates of the satellite's shadow will be equal to

$$\left.\begin{array}{l} x_s = x' \cos \Delta A + a\zeta' \sin \Delta A \\ y_s = y' \cos D_\oplus - (a\zeta' \cos \Delta A - x' \sin \Delta A) \sin D_\oplus \\ z_s = -y' \sin D_\oplus - (a\zeta' \cos \Delta A - x' \sin \Delta A) \cos D_\oplus \end{array}\right\}, \quad (7)$$

and their rates of change are the following:

$$\left.\begin{array}{l} \dot{x}_s = \dot{x}' \cos \Delta A + a\dot{\zeta}' \sin \Delta A \\ \dot{y}_s = \dot{y}' \cos D_\oplus - (a\dot{\zeta}' \cos \Delta A - \dot{x}' \sin \Delta A) \sin D_\oplus \\ \dot{z}_s = -\dot{y}' \sin D_\oplus - (a\dot{\zeta}' \cos \Delta A - \dot{x}' \sin \Delta A) \cos D_\oplus \end{array}\right\}. \quad (8)$$

At the solution of the formulated problem are used only the coordinates x_s and y_s of the satellite's shadow, and also their rate of change $\dot{x}_s$ and $\dot{y}_s$.

The velocity of the satellite's shadow motion across the illuminated part of the planet's visible disk can be defined by the following formula: $V_s = \sqrt{\dot{x}_s^2 + \dot{y}_s^2}$. The simultaneous formulae (7) and (8) hold for any phase angle values and planetocentric declination of the Earth.

If it is deemed that $D_\oplus = 0$ in the second approximation, then it follows from expression (6) that $\Phi = \pm \Delta A$, and the simultaneous formulae (7) and (8) are transformed to the system of formulae (4) and (5).

5. The simulation of the satellite's shadow motion across the illuminated part of the planet's visible disk using the analytical method

The suggested analytical method was tested under various lighting conditions for the planet's visible disk using the numerical method as a reference one. The coordinate z_s of the satellite's shadow and its rate of change $\dot{z}_s$ were used at testing of an analytical method, but for the solution of the formulated problem they have no practical importance. The plot of the x_s coordinate and its rate of change $\dot{x}_s$ against the x' coordinate in a special case in the first approximation at different phase angles are shown in Fig. 5.

As it follows from Fig. 5, the presented dependence is only linear at $\Phi = 0$. At other phase angle values the dependence is nonlinear. As coordinate x' is proportional to time, the satellite's shadow motion across the planet's visible disk is not uniform. The minimum velocity of the satellite's shadow motion is observed near the planet's light limb L, the maximum velocity is observed near the terminator T. With increasing phase angle the nonuniformity of the natural satellite's shadow motion increases.

The analytical method was tested for an example of the Ganymede and its shadow transit across Jupiter's visible disk that occurred on November 12-13, 2002 near the western quadrature (Mikhalchuk, 2007). As per initial data, the instant T'_0 of the satellite's inferior heliocentric conjunction was $19^\text{h}30^\text{m}.45$ TDT November 12. The daily changes $\dot{x}' = -13.14963$ and $\dot{y}' = -0.00769$ computed at the indicated instant can be deemed constant throughout the transit. The instants T'_1 and T'_2 of the satellite's shadow contact with the illuminated part of the planet's visible disk in the spherical approximation were $17^\text{h}44^\text{m}.77$ TDT and $21^\text{h}18^\text{m}.02$ TDT November 12, respectively. An example of computation results at instant $19^\text{h}00^\text{m}.0$ TDT November 12 is presented in Table 1. For the indicated instant the values of the initial coordinates were $x' = +0.27807$ and $y' = -0.19053$.

The approximations for the numerical method (both the first and the second one) are the same as those for the analytical method. The computation using the precise numerical method was carried out according to the physical ephemerides. As follows from Table 1, the results obtained using different methods (namely, the numerical and analytical ones) are similar in the same approximations; that goes to show the trueness

Table 1: The computation results of the Ganymede's shadow position and velocity on the illuminated part of Jupiter's visible disk obtained with various methods.

Method	Approximation	x_s	y_s	z_s	$\dot{x}_s$	$\dot{y}_s$	$\dot{z}_s$
Numerical	first	+0.44921	−0.19053	−0.87288	−12.19177	−0.00769	−6.27257
Numerical	second	+0.44918	−0.19338	−0.87226	−12.19195	−0.02820	−6.27217
Numerical	precise	+0.44945	−0.18385	−0.87418	−12.19255	+0.01108	−6.27106
Analytical	first	+0.44921	−0.19053	−0.87288	−12.19177	−0.00769	−6.27257
Analytical	second	+0.44918	−0.19338	−0.87226	−12.19195	−0.02820	−6.27217

of the analytical method applied.

6. Conclusion

The key findings of the present study enable to make the following conclusions:

1. The suggested analytical method for determination of the coordinates of the satellite's shadow of the spherical planet on the geocentric plane of the sky and their rate of change allows to receive the solution as the formulae directly connecting these values with coordinates of the satellite on the heliocentric plane of the sky and their rates of change for two approximations of the location of the Earth and the Sun relative to the planet's rotation axis.

2. The formulae obtained in both approximations of the conditions of illumination of the visible planet's disk, are valid for any values of the phase angle and are precise within the limits of the given approximation.

3. The motion of the satellite's shadow on the illuminated part of the visible planet's disk is not uniform, that it is necessary to take into account at the calculation of the ephemerides and at determination of the sizes of the satellite's shadow on the illuminated part of the visible planet's disk.

References

Emel'yanov N.V.: 1996, *Pis'ma Astron. Zh.,* **22**, 153.
Bureau Des Longitudes: 2001, *Paris, IMCCE, http://www.bdl.fr/ephem/ephesat/phenjup_eng.html*
Mikhalchuk V.V.: 2007, *Astron. Vestn.,* **41**, 555.
Mikhalchuk V.V.: 2004, *Kinematika Fiz. Nebeshykh Tel,* **20**, 76.
Mikhalchuk V.V.: 2007a, *Odessa Astron. Publ.,* **20**, Part 2, 76.
Mikhailov A.A., 1954: *The Theory of Eclipses,* GITTL, Moscow.
Vakhrameeva L.A., Bugaevskij L.M., Kazakova Z.L., 1986: *Mathematical Mapping,* Nedra, Moscow.

THREE-DIMENSIONAL NUMERICAL HYDRODYNAMIC SIMULATION OF ON- AND OFF-STATES IN MICROQUASARS AND QUASARS

V.V. Nazarenko, S.V. Nazarenko

Astronomical Observatory, Odessa National University,
Odessa, Ukraine, *astro@paco.odessa.ua*

ABSTRACT. As is shown in the present computations performed using three-dimensional numerical astrophysical methods, in microquasars in the course of precession of the accretion disc blown by the donor's wind the on- and off-states start being generated in the disc. In our case, the transition between these states takes 30-40 minutes of the orbital time. In the off-state the temperature changes discretely, i.e. such a change appears as separate sharp peaks, which almost merge with each other over time.

Key words: Stars: close binary system; microquasars; quasars.

1. Introduction

The present study carried out using numerical methods for astrophysics aims to show that in microquasars in the course of precession of the accretion disc blown by the donor star's wind the on-states (high/soft) and off-states (low/hard) start being generated in the disc.

The afore-mentioned phenomenon was simulated by the example of a microquasar in the semi-detached close binary (CB) Cyg -1.

The main purpose of these computations is to simulate the accretion disc and its driven precession provided that the donor slightly overfills its Roche lobe (the donor's photospheric layers are in the vicinity of the L_1 point), and the radiation wind flows from the remaining part of the donor's surface (except the vicinity of the L_1 point) at that.

2. The numerical algorithm

The numerical approach for the accretion disc formation in the microquasar Cyg X-1 is identical to that one used in massive X-ray CB and microquasar candidates Cen -3 and LMC -3 [1,2]. When computing the gas flow, the astrophysical version of the large-particle method by Belotserkovskii & Davydov [3] was applied

for integration of the non-stationary Euler equations.

To show how the computations were performed, let us describe the numerical scheme of the astrophysical version of the Belotserkovskii & Davydov large-particle method. To carry out computations by the method of large particles, the entire computational domain is divided into three-dimensional rectangular grid cells, and all integer values of physical quantity indices correspond to the grid cells geometric centres. All physical quantities are constant within a given cell. The fractional indices fall at the grid cell's boundaries. The formulae below are written in such a way that the direction of an increase in each index along all three axes coincides with the positive directions of those axes. In the presented formulae the variables $U^n_{i,j,k}$, $V^n_{i,j,k}$ and $UZ^n_{i,j,k}$ are initial velocities at a given n^{th} time-step along the x, y and z axes in the cell with indices i, j and k, respectively; and the variables $U^n_{1,i,j,k}$, $V^n_{1,i,j,k}$ and $UZ^n_{1,i,j,k}$ are final velocities in the first stage of computations.

It should be noted that in the first stage of computations with a given time-step the pressure and external field effects were the only factored in. The effects of the transfer of physical quantities across the cell boundaries were accounted for in the second stage of computations. In equations 2, 7 and 9, among all non-inertial forces, only those proportional to ω_0 and ω_0^2 are taken into account; while the effects proportional to $\omega_p \cdot AA$ and $(\omega_p \cdot AA)^2$, i.e. effects associated with the donor's precession, are not factored in due to their apparent smallness as $\omega_p = \omega_0/2.56$ and $AA = 0.15$. It is also should be mentioned that the pressure effects written as the central differences in the equations below make the numerical scheme unstable; however, the effects of the physical quantity transfer, which account for the gas flow direction, are used in the second stage of computations, and that makes the numerical scheme of the large-particle method absolutely stable, steady and strictly conservative.

$$U^n_{1,i,j,k} = U^n_{i,j,k} + A \cdot dt \quad ,where \qquad (1)$$

$$A = \frac{P^n_{i+1/2,j,k} - P^n_{i-1/2,j,k}}{\rho^n_{i,j,k} \cdot dx_i} +$$

$$+ \frac{GM_{donor}(x - x_{donor})}{R^3_{donor}} + \frac{GM_x(x - x_{accr})}{R^3_{accr}} -$$

$$- 2 \cdot V^n_{i,j,k} \cdot \omega_0 \cdot \cos\beta + \omega_0^2(x - x_{c.m})\cos\beta \quad (2)$$

$$\beta = \arctan z_{accr} \quad , \quad (3)$$

where $z_{accr} = AA\sin(\omega_p t)$, $\omega_p = \frac{2\pi}{P_{prec}}$, $\omega_0 = \frac{2\pi}{P_0}$, $AA = 0.15$

$$R_{donor} = \sqrt{(x - x_{donor})^2 + (y - y_{donor})^2 + (z - z_{donor})^2} \quad (4)$$

$$R_{accr} = \sqrt{(x - x_{accr})^2 + (y - y_{accr})^2 + (z - z_{accr})^2} \quad (5)$$

$$V^n_{1,i,j,k} = V^n_{i,j,k} + B \cdot dt \quad , where \quad (6)$$

$$B = \frac{P^n_{i,j+1/2,k} - P^n_{i,j-1/2,k}}{\rho^n_{i,j,k} \cdot dy_j} +$$

$$+ \frac{GM_{donor}(y - y_{donor})}{R^3_{donor}} + \frac{GM_{accr}(y - y_{accr})}{R^3_{accr}} +$$

$$+ 2U^n_{i,j,k} \cdot \omega_0 \cdot \cos\beta +$$

$$+ 2UZ^n_{i,j,k} \cdot \omega_0 \cdot \sin\beta + \omega_0^2(y - y_{c.m.}) \quad (7)$$

$$UZ^n_{1,i,j,k} = UZ^n_{i,j,k} + C \cdot dt \quad , where \quad (8)$$

$$C = \frac{P^n_{i,j,k+1/2} - P^n_{i,j,k-1/2}}{\rho^n_{i,j,k} \cdot dz_k} +$$

$$+ \frac{GM_{donor} \cdot (z - z_{donor})}{R^3_{donor}} + \frac{GM_{accr}(z - z_{accr})}{R^3_{accr}} +$$

$$+ 2\omega_0 \cdot V^n_{i,j,k} \cdot \sin\beta + \omega_0^2(z - z_{c.m.})\sin\beta \quad (9)$$

$$E^n_{1,i,j,k} = E^n_{i,j,k} + D \cdot dt \quad , where \quad (10)$$

$$D = \frac{P^n_{i,j,k}}{\rho^n_{i,j,k}} \cdot \frac{U^n_{i+1/2,j,k} - U^n_{i-1/2,j,k}}{dx_i} +$$

$$+ \frac{P^n_{i,j,k}}{\rho^n_{i,j,k}} \cdot \frac{V^n_{i,j+1/2,k} - V^n_{i,j-1/2,k}}{dy_j} +$$

$$+ \frac{P^n_{i,j,k}}{\rho^n_{i,j,k}} \cdot \frac{UZ^n_{i,j,k+1/2} - UZ^n_{i,j,k-1/2}}{dz_k} \quad (11)$$

$$P^n_{i,j,k} = n^n_{i,j,k} \cdot KT^n_{i,j,k} \quad (12)$$

In the presented formulae G - the constant of gravitation; M_{donor} and M_{accr} - the donor and accretor masses, respectively; x_{donor}, y_{donor}, z_{donor} - the donor's geometric centre coordinates; x_{accr}, y_{accr}, z_{accr} - the accretor's geometric centre coordinates; P_0 - the orbital period; P_{prec} - the precession period of the target CB; $x_{c.m.}$, $y_{c.m.}$, $z_{c.m.}$ - the coordinates of the CB centre of mass; $E^n_{i,j,k}$ - specific internal energy at the beginning of a given time-step in the grid cell with indices i, j, k, $E^n_{1,i,j,k}$ - specific internal energy at the end of the first stage of the nth time-step in the grid cell with indices i, j, k; $\rho^n_{i,j,k}$ - the density in the first stage of the nth time-step in the grid cell with indices i, j, k; dx_i, dy_j, dz_k a given grid cell's dimensions in the x, y, z directions; $P^n_{i,j,k}$ - the pressure in the grid cell with indices i, j, k at the nth time-step; K - the Boltzmann constant; $T^n_{i,j,k}$ - the temperature in the grid cell with indices i, j, k at the nth time-step. The physical quantities with fractional indices were computed with numerical differences of up to and including the third order that resulted in rather accurate calculation of the physical quantities on the non-uniform computational grid.

The second stage of computations of the numerical algorithm for the large-particle method is described starting with formula 13. In this stage the flows of physical quantities across the grid cell boundaries are computed, and the final velocities and temperatures at a given time-step are determined. Formula 13 describes the calculation of change in density at a given time-step in a given grid cell. Formulae 14-15 describe calculations of the mass flow across $i - 1/2$ boundary of a given grid cell. As is seen in these formulae, the velocity directions are taken into account when computing the mass flow. Such arrangement of the second stage computations for the large-particle method makes the scheme integrally stable, steady and strictly conservative. The other mass flows across other grid cells boundaries, used in formula 13, are computed similarly to formulae 14 and 15. At that the positive direction of the velocity in formulae 14 and 15 corresponds to the increment in the grid cell number.

$$\rho^{n+1}_{i,j,k} = \rho^n_{i,j,k} + \frac{\triangle M^n_{i-1/2,j,k} - \triangle M^n_{i+1/2,j,k}}{dx_i dy_j dz_k} +$$

$$+ \frac{\triangle M^n_{i,j-1/2,k} - \triangle M^n_{i,j+1/2,k}}{dx_i dy_j dz_k} +$$

$$+ \frac{\triangle M^n_{i,j,k-1/2} - \triangle M^n_{i,j,k+1/2}}{dx_i dy_j dz_k} \quad (13)$$

$$\triangle M^n_{i-1/2,j,k} = dy_j \cdot dz_k \cdot U^n_{1,i-1/2,j,k} \cdot \rho^n_{i-1,j,k} \cdot dt,$$
$$if\ \mathrm{U}^n_{1,i-1/2,j,k} > 0$$

$$(14)$$

$$\triangle M^n_{i-1/2,j,k} = dy_j \cdot dz_k \cdot U^n_{1,i-1/2,j,k} \cdot \rho^n_{i,j,k} \cdot dt,$$
$$if \ \mathrm{U}^n_{1,i-1/2,j,k} < 0$$

(15)

When computing formula 18, three velocity components (calculated in the first stage) and total energy, which are determined in curly brackets in formula 16, successively substitute for the variable $Z^{n+1}_{i,j,k}$.

$$Z^{n+1}_{i,j,k} = \left\{ U^n_{1,i,j,k}; V^n_{1,i,j,k}; UZ^n_{1,i,j,k}; E^n_{total,i,j,k} \right\} \quad (16)$$

$$E^n_{total,i,j,k} = \frac{(U^n_{1,i,j,k})^2 + (V^n_{1,i,j,k})^2}{2} +$$
$$+ \frac{(UZ^n_{1,i,j,k})^2}{2} + E^n_{1,i,j,k} \quad (17)$$

$$Z^{n+1}_{i,j,k} = \frac{Z^n_{i,j,k}\rho^n_{i,j,k}}{\rho^{n+1}_{i,j,k}} + \frac{\triangle M^n_{i-1/2,j,k} \cdot Z^n_{i-1,j,k}}{\rho^{n+1}_{i,j,k} \cdot dx_i \cdot dy_j \cdot dz_k} +$$
$$+ \frac{-\triangle M^n_{i+1/2,j,k} \cdot Z^n_{i,j,k} + \triangle M^n_{i,j-1/2,k} \cdot Z^n_{i,j-1,k}}{\rho^{n+1}_{i,j,k} \cdot dx_i \cdot dy_j \cdot dz_k} +$$
$$+ \frac{-\triangle M^n_{i,j+1/2,k} \cdot Z^n_{i,j,k} + \triangle M^n_{i,j,k-1/2} \cdot Z^n_{i,j,k-1}}{\rho^{n+1}_{i,j,k} \cdot dx_i \cdot dy_j \cdot dz_k} -$$
$$- \frac{\triangle M^n_{i,j,k+1/2} \cdot Z^n_{i,j,k}}{\rho^{n+1}_{i,j,k} \cdot dx_i \cdot dy_j \cdot dz_k} \quad (18)$$

The boundary conditions and radiation wind from the donor in these computations are similar to those ones in our earlier studies [1, 2].

We assumed that the binary parameters are as follows: the Cyg X-1 orbital period is 5.6 days; the accretor's mass is 10 $M_\odot$; the donor's mass is 20 $M_\odot$[4]; the accretion velocity in the disc is about $3.0 \cdot 10^{-8}$ $M_\odot$/year [5].

The condition of the accretion disc formation is that the wind acceleration in the radial direction in the vicinity of the L_1 point and along the line of centres in the accretor's Roche lobe should decrease to zero. The L_1 point vicinity starts at the L_1 point and extends to the accretor's Roche lobe; in these computations the chosen vicinity extension in the radial direction is 0.22 (here and elsewhere all distances are given in units of orbital separation).

In this study, the driven precession computations were performed given that the precession donor is embedded, i.e. fixed in this computational grid while it is accretor that changes its position in space (i.e. moves across the computational grid). However, mutual positioning of the accretor and donor changes in a similar way as if it is the donor is precessing (the effect of

the uniform motion relativity in classical physics). At that we assume that the donor is precessing uniformly without surges and accelerations, so the accretor's motion will be uniform as well. The precession period is assumed equal to 20 orbital periods.

It should be noted that we do not assume any additional conditions for the on- and off-states creation, they should be generated in the disc under the only effect of precession with no additional conditions.

3. The computational results of the on- and off-states generation in the disc

The study task is posed in such a way that the initiation of the winds from the donor and accretion disc is calculated first, then the accretion disc's driven precession is started, and the computations proceed as far as the computer capability permits to trace disc's evolution as long as possible.

The donor's wind is initiated during the first quarter-third of the first orbital period, and the disc is formed in the course of the first orbital period.

The orbital plane section and that one of the plane, which is perpendicular to it and lies on the line of centres, in the computational domain at the instant of time corresponding to the precession period 1.31 are presented in Fig. 1 and 2. These figures show the donor, wind from donor and accretion disc, which is tightly compressed by the wind from the donor at the given precession phase (the beginning of the low/hard phase).

The key properties of the disc resulted from these computations, such as the temperature in the disc's centre and accretion rate around the disc's centre as functions of time, are shown in Fig. 3 and 4. As is seen in these figures, the accretion rate and temperature over each precession period change markedly (by more than two orders of magnitude); when there is a two-order increase in the temperature in the disc's centre, the accretion rate drops accordingly by two or just over two orders of magnitude at the same instants. All those variables fluctuate dramatically at that while the transition between high and low temperature conditions, and low and high accretion rates, respectively, takes 30-40 minutes of the orbital time.

Thus we can state the fact that in our computations in the course of precession of the numerical disc model high and low temperature conditions, and low and high accretion rates, respectively, are generated; and we interpret these conditions as the off- and on-states of the accretion discs in microquasars, respectively. The fact that the numerical disc model alters significantly over the precession period is given in Fig. 5 where it is shown that the disc's mass changes with the precession period (the disc's mass is given on the logarithmic scale in $M_\odot$). As it is seen in this figure, the disc's mass
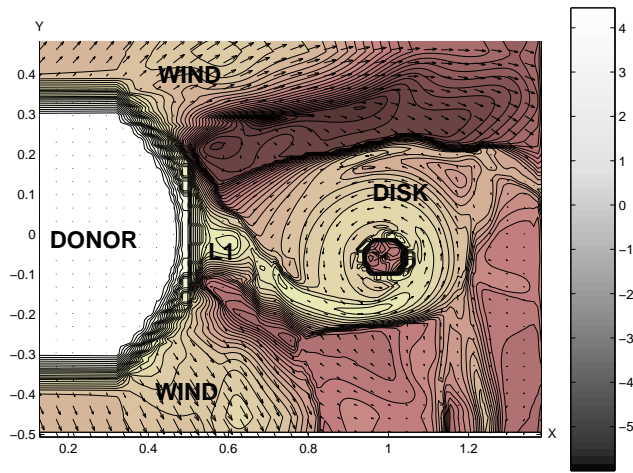
Figure 1: The number density distribution over the computational domain at the precession phase 1.31 in the orbital plane.
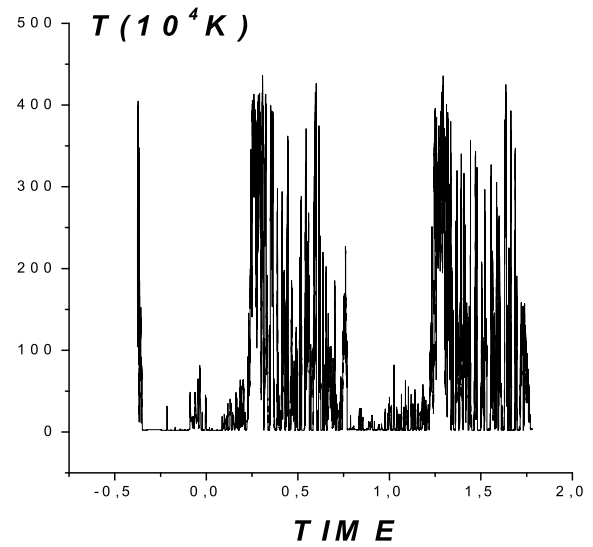

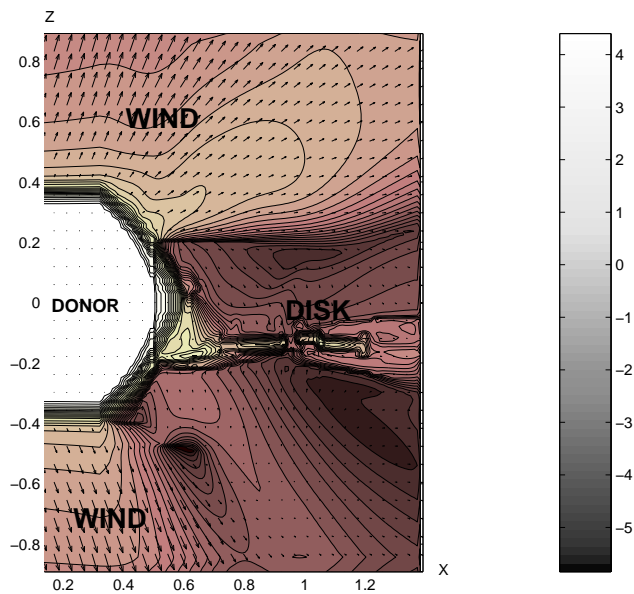Figure 3: The temperature in the disc's centre over time.

Figure 2: The number density distribution over the computational domain at the precession phase 1.31 in the Z-X plane.
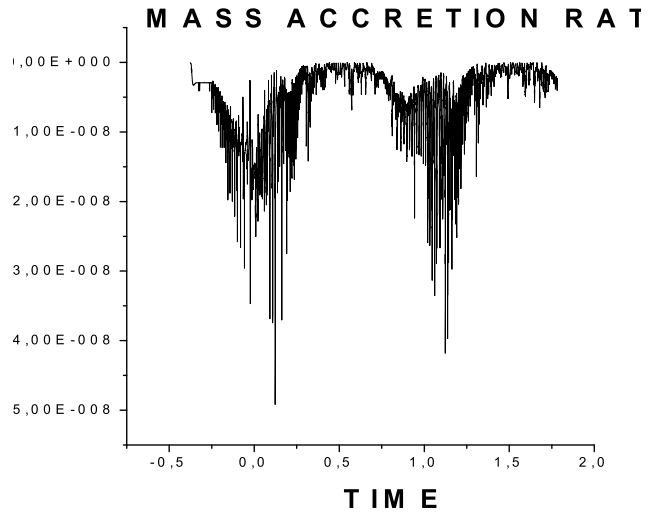

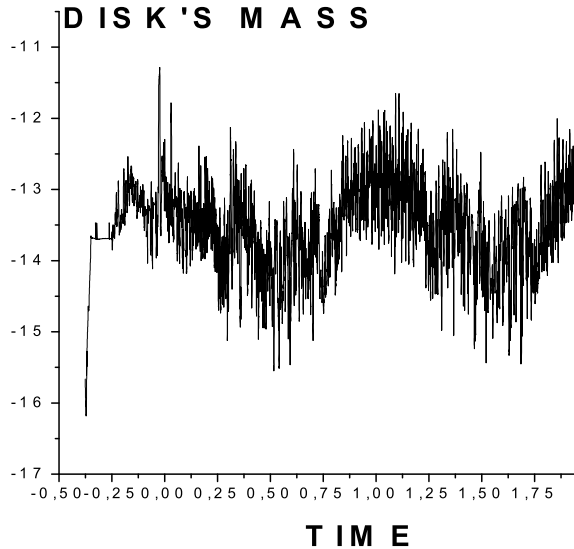Figure 4: The mass accretion rate in the disc's centre over time.

Figure 5: The disc's mass over time on the logarithmic scale in $M_\odot$.

changes by almost two orders of magnitude; and at that when the accretion rate is maximum at the high/soft phase, the disc's mass also reaches maximum.

As can be concluded from the aforesaid, the precession mechanism of the on- and off-states generation works as follows: while the accretion disc is precessing, the wind from the donor flows onto the disc at different instants at various angles, causing the disc's tight compression (that occurs near the precession phase 0.00, which is approximately the middle of the high/soft phase); in that case the accretion rate increases, and the on-state occurs in the disc as the radiative cooling is very effective with high concentrations in the disc's centre, and hence the gas cools down to low temperatures. At the counter precession phase near the phase 0.50 (which is approximately the middle of the low/hard phase) the disc does not practically experience the wind's pressure that results in the wind-accretion rate decrease and the off- state occurrence as the radiative cooling becomes ineffective at that instant, and the temperature in the disc's centre increases significantly.

4. Conclusions

This study conducted using methods for three-dimensional numerical hydrodynamics shows that in microquasars in the course of precession of the accretion disc blown by the donor's wind the on- and off-states are generated in the disc, at that the transition between these states is catastrophically fast and takes 30-40 minutes of the orbital time. The computations also showed that the temperature in the disc's centre changes discretely in the off-state and such a change appears as separate sharp peaks, which are at very small distances from each other (5-10 minutes of the orbital time). As follows from the observations, such discrete behaviour of the temperature in the low/hard phase corresponds to the similar discrete behaviour of the hard X-rays in the low/hard phase.

References

Nazarenko V.V.: 2006, *Astronomy Reports,* **50**, 647.

Nazarenko V.V.: 2008, *Astronomy Reports,* **52**, 40.

Belotserkovskii O.M., Davydov Yu.M.: 1982, "The big particles code in gas dynamics", Moskaw, Scientist, 391.

Karitskaja E.A., Bochkarev N., private communications.

Wijers R.A.M.J. & Pringle J.E.: 1999, *MNRAS,* **308**, 207.

10 NEW VARIABLE STARS IN THE CONSTELLATION ANTLIA

Ivan Sergey, Sergei Dubrouski, Igor Baluk, Alexander Pobyiaha

The Regional Centre of Technical Creativity of Children and Youth (RCTCCY), Gomel, Belarus
seriv76@tut.by; toliman@tut.by; balig@tut.by; apobiyaha@gmail.com

ABSTRACT. 10 new variable stars in the constellation Antlia are reported, their phenomenological characteristics are listed.

Key words: Stars: new variable stars, eclipsing binaries, RR Lyr-type stars, Catalina survey.

1. Introduction

The authors carried out investigation using the time series photometry data from the Catalina Real-Time Transient Survey (CRTS) in 2013-2014. About 2,300 new variable stars were found; the data for 10 the most recently discovered ones are presented in the journal Odessa Astronomical Publications. Sergei A. Dubrouski is a software architect of the data-mining project who is responsible for the semi-automatic search for new variable stars prior to the final processing of those data by a group of enthusiasts. Alexander V. Pobyiaha is Sergey Dubrouski's assistant in the digital photometric sky survey data processing.

SSS_J105243.0-283155
The star was discovered by I.I. Baluk.
The PPMXL position of the star: RA = 10^h 52^m 43.007^s, Dec = -28° 31' 55.49".
The star's catalogue identifiers: the 2MASS identifier – J10524300-2831555, the USNO identifier – B1.0 0614-0251069.
The star's variability type: EA.
The peak brightness is 16.20^m; the primary minimum brightness is 16.91^m (in the C and V bands), the secondary minimum brightness is 16.33^m (in the C and V bands).
The star's light ephemerides are plotted in Figure 1. D = 0.18.

HJD Min = 2454236.981 + 0.587550 *E
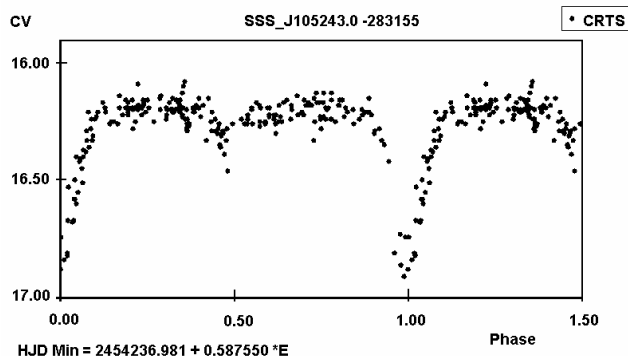
Figure 1

SSS_J104410.6-225402
The star was discovered by I.I. Baluk.
The PPMXL position of the star: RA = 10^h 44^m 10.619^s, Dec = -22° 54' 02.46".
The star's catalogue identifiers: the 2MASS identifier – J10441060-2254023, the USNO identifier – B1.0 0670-0284915.
The star's variability type: RRC.
The peak brightness is 16.95^m; the minimum brightness is 17.44^m (in the C and V bands).
The star's light ephemerides are plotted in Figure 2. M – m = 0.4.

HJD Max = 2455031.876 + 0.290566 *E
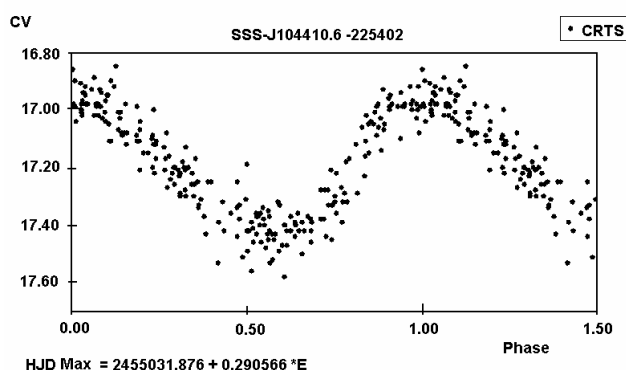
Figure 2

SSS_J103605.4-233709
The star was discovered by I.I. Baluk.
The PPMXL position of the star: RA = 10^h 36^m 05.396^s, Dec = -23° 37' 10.12"
The star's catalogue identifiers: the 2MASS identifier – J10360539-2337101, the USNO identifier – B1.0 0663-0243873.
The star's variability type: EW.
The peak brightness is 16.30^m; the minimum brightness is 16.80^m (in the C and V bands).
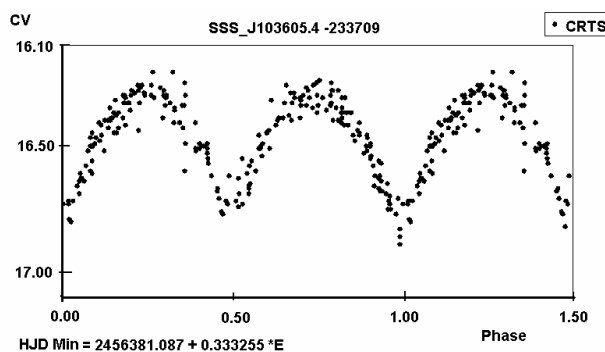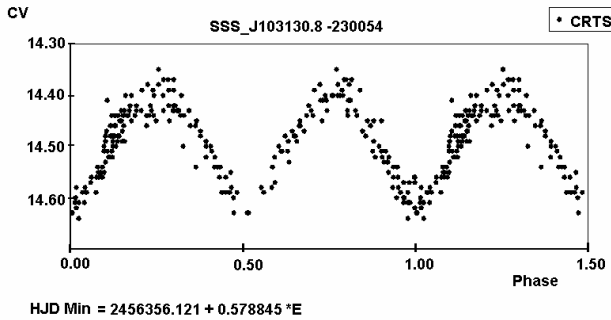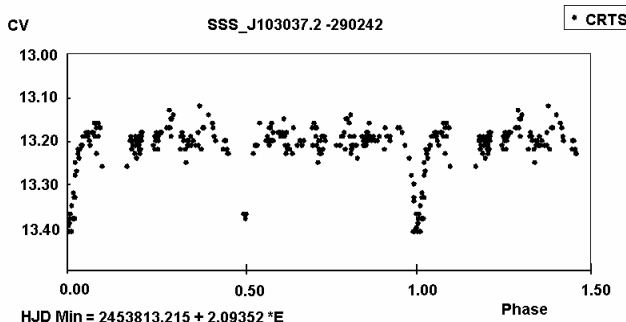The star's light ephemerides are plotted in Figure 3.

HJD Min = 2456381.087 + 0.333255 *E
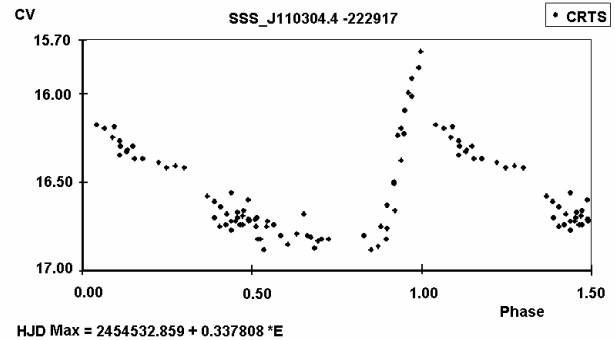
Figure 3

SSS_J103130.8-230054

The star was discovered by I.I. Baluk.

The UCAC4 position of the star: RA = 10^h 31^m 30.844^s, Dec = -23° 00' 54.55".

The star's catalogue identifiers: the 2MASS identifier – J10313084-2300545, the USNO identifier – B1.0 0669-0272688, the GSC identifier – 06620-00917, the UCAC4 identifier – 335-062709.

The star's variability type: EW.

The peak brightness is 14.40^m; the minimum brightness is 14.60^m (in the C and V bands).

The star's light ephemerides are plotted in Figure 4.

HJD Min = 2456356.121 + 0.578845 *E

Figure 4

SSS_J103037.2-290242

The star was discovered by I.I. Baluk.

The UCAC4 position of the star: RA = 10^h 30^m 37.228^s, Dec = -29° 02' 42.86".

The star's catalogue identifiers: the 2MASS identifier – J10303723-2902428, the USNO identifier – B1.0 0609-0245875, the GSC identifier -06632-01372, the UCAC4 identifier -305-064151.

The star's variability type: EA.

The peak brightness is 13.20^m; the primary minimum brightness is 13.41^m (in the C and V bands); the secondary minimum brightness is 13.38^m (in the C and V bands).

The star's light ephemerides are plotted in Figure 5. D = 0.07.

HJD Min = 2453813.215 + 2.09352 *E

Figure 5

SSS_J110303.4-222917

The star was discovered by I.M. Sergey.

The UCAC4 position of the star: RA = 11^h 03^m 04.39^s, Dec = -22° 29' 17.93".

The star's catalogue identifiers: the 2MASS identifier – J11030438-2229179, the USNO identifier – B1.0 0675-0306520, the UCAC4 identifier – 338-062729.

The star's variability type: RRAB.

The peak brightness is 15.78^m, the minimum brightness is 16.88^m (in the C and V bands).

The star's light ephemerides are plotted in Figure 6. M – m = 0.2.

HJD Max = 2454532.859 + 0.337808 *E

Figure 6

SSS_J103154.2-251541

The star was discovered by I.M. Sergey.

The PPMXL position of the star: RA = 10^h 31^m 54.26^s, Dec = -25° 15' 41.62".

The star's catalogue identifiers: the 2MASS identifier – J10315426-2515417, the USNO identifier – B1.0 0647-0249453.

The star's variability type: RRAB.

The peak brightness is 16.20^m, the minimum brightness is 17.40^m (in the C and V bands).

The star's light ephemerides are plotted in Figure 7. M – m = 0.2.

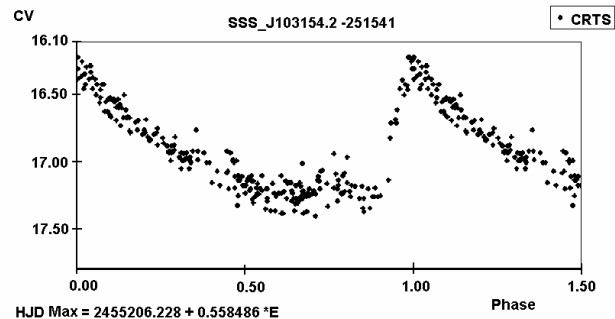HJD Max = 2455206.228 + 0.558486 *E

Figure 7

SSS_J103830.8-254501

The star was discovered by I.M. Sergey.

The UCAC4 position of the star: RA =10^h 38^m 30.77^s, Dec = -25° 45' 01.14".

The star's catalogue identifiers: the 2MASS identifier – J10383074-2545011, the USNO identifier – B1.0 0642-0251547, the UCAC4 identifier – 322-062782.

The star's variability type: RRAB.

The peak brightness is 15.30^m, the minimum brightness is 16.55^m (in the C and V bands).

The star's light ephemerides are plotted in Figure 8. M – m = 0.12.

SSS_J103830.8 -254501
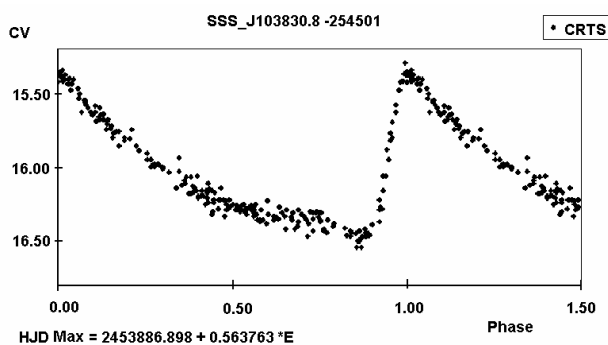
Figure 8

SSS_J104603.5-200058

The star was discovered by I.M. Sergey.

The UCAC4 position of the star: RA =10^h 46^m 03.48^s, Dec = -20° 00' 58.53".

The star's catalogue identifiers: the 2MASS identifier – J10460348-2000589, the USNO identifier – B1.0 0699-0238422, the UCAC4 identifier – 350-061961.

The star's variability type: RRAB.

The peak brightness is 16.20^m, the minimum brightness is 17.41^m (in the C and V bands).

The star's light ephemerides are plotted in Figure 9. M – m = 0.15.

SSS_J104603.5 -200058
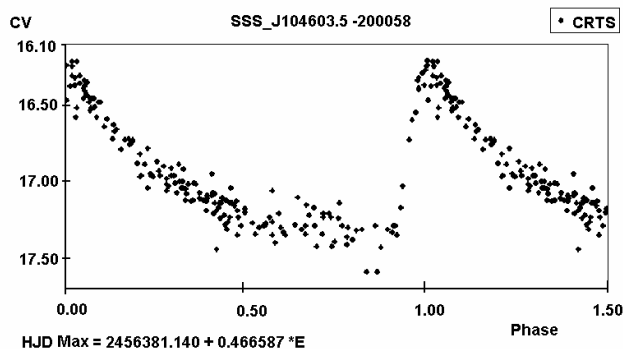
Figure 9

SSS_J104626.6-272234

The star was discovered by I.M. Sergey.

The UCAC4 position of the star: RA =10^h 46^m 26.62^s, Dec = -27° 22' 35.01".

The star's catalogue identifiers: the 2MASS identifier – J10462661-2722350, the USNO identifier – B1.0 0626-0330553, the GSC identifier – 06642-00172, the UCAC4 identifier – 314-063479.

The star's variability type: EB.

The peak brightness is 13.73^m, the primary minimum brightness is 14.42^m (in the C and V bands) the secondary minimum brightness is 14.05^m (in the C and V bands).

The star's light ephemerides are plotted in Figure 10. M – m = 0.15.
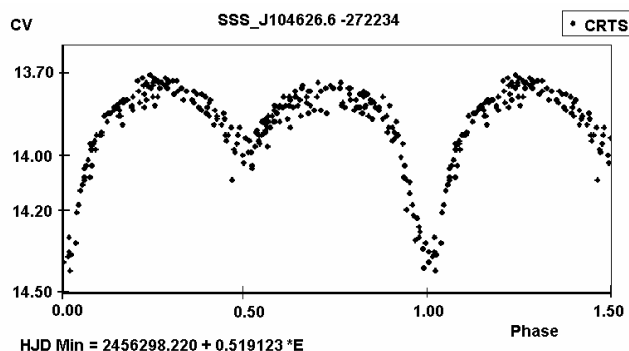
SSS_J104626.6 -272234

Figure 10

References

Lafler J., Kinman T. D.: 1965, *Ap. J. Suppl.*, **11**, 216.

Drake A. J. et al.: 2009, *ApJ*, **696**, 870.

THE ROTATING DISC EFFECT

O. Sh. Shahrukhanov

Astronomical Observatory, Odessa National University
Odessa, Ukraine

ABSTRACT. It is demonstrated that it is possible to obtain a significant small-scale gradient of spatial properties using the rotating disc.

1. Introduction

The study of the rotating disc effect on the displacement of interference fringes produced by the interferometer is discussed in this paper. The preliminary results of the study were described earlier by Shahrukhanov (2013ab). Later on the 4.5 kg disc was substituted for the 2.5 kg disc to achieve greater fringe shifting effect.

The schematic representation of the interferometer is shown in Figure 1. The metal tubes in which the interferometer was housed were removed from the scheme due to decreased amplitude of vibrations caused by the disc rotation. To do so the whole device (the disc with drive motor) was housed within metal casing wrapped with cloth tape to ensure the vibration disturbance elimination.

The interference fringe displacement effect is observed when the disc is positioned so that its rotation axis coincides with the interferometer arm M2-M3. When the disc is positioned between the interferometer's main arms M2-M3 and M1-M3, the fringe shifting effect is not observed within the measurement accuracy. The maximum fringe displacement is above 2000 angstroms with the disc's angular momentum of about 5 kg·sq.m/sec.

Figure 2 shows the time dependence of the angular momentum and interference fringe displacement value (in angstroms).

A physical model describing the phenomenon nature was proposed by me for publication in 1984. The model was based on two principles of inertia:

a) the inertial forces result from interaction of mass trajectories (the disc is considered to be an aggregate of point masses);

b) the effective values of inertial forces are arranged in the scalar field.

The same principles are deemed general ones for the nature of magnetic field.

2. Conclusion

The described model investigation allows to draw a conclusion that in principle it is possible to find the gradient of inertial interactions. In the presented model the speed of light is thought as the index of spatial properties at a given point.
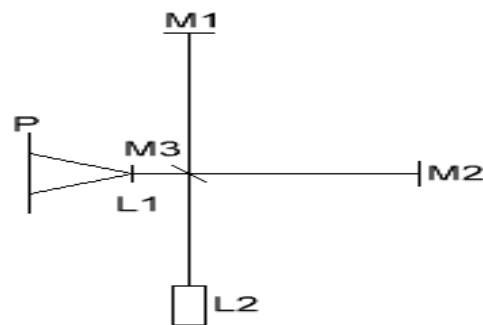

Figure 1: The schematical representation of the interferometer. The legend: M1, M2 – mirrors, M3 – a beam-splitter, L1 – a lens, L2 – a laser, P – the screen onto which the interference pattern is projected.
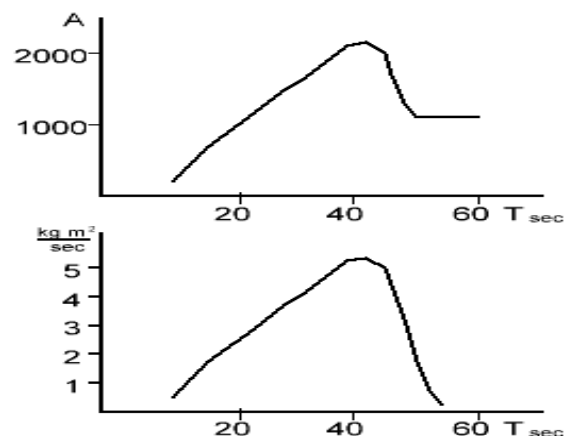

Figure 2: The time dependence of the angular momentum and interference fringe displacement value.

References

Shahrukhanov O.Sh.: 2013a, *Odessa Astr. Publ.,* **26**, 315.

Shahrukhanov O. Sh.: 2013b, "Chemical and Dynamical Evolution of Stars and Galaxies" Conference to commemorate the 75th Anniversary of N.S. Komarov", 20-22.08.2013, Odessa, Ukraine.

WAVELET ANALYSIS OF VARIABILITY OF THE RADIO SOURCE 3C120 IN CENTIMETER WAVELENGTH RANGE

Sukharev A.L.[1], Aller M.F.[2]

[1] Radio Astronomical Institute of National Academy Sciences of Ukraine, Observatory "URAN-4"

[2] Radio astronomical observatory of Michigan University, Ann Arbor, USA

ABSTRACT. 3C120 – radio galaxy with an active nucleus has been intensively studied for many years in a wide range of the electromagnetic spectrum. We used observational data for 1966-2010 years, obtained with the radio telescope at Michigan State University (UMRAO) at frequencies of 14.5, 8 and 4.8 GHz. To study the variability of the radio source, we used wavelet method for time series analysis. The main periods in three frequencies are ~4.5 years and 6-12 years (~0.7, 1.6 and 3.4 years for the short-periodic flux component). The delay between radio frequencies was calculated. The comparison between the change in periods of fluctuations of radio fluxes and dynamics of the jet was performed (image VLBI Mojave, 15.4 GHz). Based on the periods found, we conducted forecasting changes in the radio flux and compared the results with the observation data.

Keywords: 3C120, radio galaxy, flux variability.

1. Introduction

The studied radio source 3C120 (Mrk 1506) refers to the radio galaxy type FR I and is characterized by rapid and significant changes in luminosity in different ranges of electromagnetic waves. With redshift – 0.033 (Michel et al., 1988), distance to the object – 150 Mpc, the highest speed of jet components – 6.4c (Lister et al., 2013), and flat radio spectrum, 3C120 is a gamma-ray source.

2. Data processing

Initial data on three frequencies (14.5, 8, 4.8 GHz) were obtained on a 26-meter radio telescope of the University of Michigan. The method of data gathering and processing for the RT-26 is described in (Aller et al., 2001). The observation period is 1966-2010 (Figure 1). The average interval between samples is 7 days. The correlation coefficients between the radio frequencies are as follows: 0.88 (14.5-8 GHz), 0.70 (14.5-4.8 GHz), 0.86 (8-4.8 GHz).

In the process of data preprocessing for analysis the smoothing with moving average and detrending with polynomial were performed (Gaydyshev, 2001), followed by trigonometric interpolation. To isolate the short-periodic component (O-C), the FFT filtering was applied (Voskoboynikov, 2010). To search for periodicities in the data, we used continuous wavelet analysis with the Morlet function and wavelet filtering and reconstruction, which are described in detail in the following papers (Davidov, 2007;

Smolentsev, 2010; Astafeva, 1996). Determination of time delay between data at different frequencies was performed using cross-correlation method (Rosenberg et al., 1994).
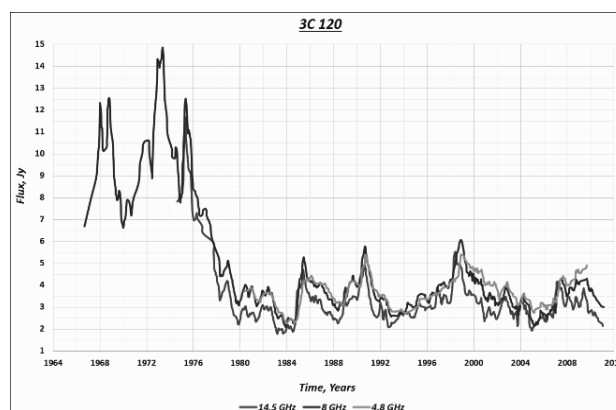

Figure 1: The 3C120 combined graphs for changes in radio fluxes at three frequencies

3. Wavelet analysis

As a result of the analysis the matrix of the continuous wavelet transform coefficients was obtained, representing a surface in three-dimensional space. Usually, they are replaced by projections on the plane "frequency-time" with the contour line that allows of tracking changes over time in the frequency spectrum. The examples of wavelet spectra are shown in Figure 2.

The values of the periods in years are given in Table 1. The radio variability is divided into long-term (trend) and fast (O-C) components. The high-frequency part of the signals was isolated from trending periods and restored by the FFT filtering. Thus, we obtained the values of short periods which are hardly distinguishable on the original spectra.

As is seen from Table 1, the values of the long period are stable for the entire length of the time series, except that one at frequency 14.5 GHz. Most values of short periods change over time; moreover, the corresponding periods of oscillations occur in limited intervals of time. The phase activity (last column on the right) shows the time of maxima of global wavelet spectra in the frequency range (showing time distribution of full power of wavelet spectrum). Since the spectral composition of the signal changes over time, each time of maximum spectral power at the global spectrum corresponds to the value of period,

which is the most strongly expressed at this time (Ryabov et al., 2012). Thus, using the visualization of wavelet spectrum as a series of "period-spectral power" graphs for each year separately, we can determine which periods make the largest contribution to the radio source's phase activity and compare them with VLBI maps.
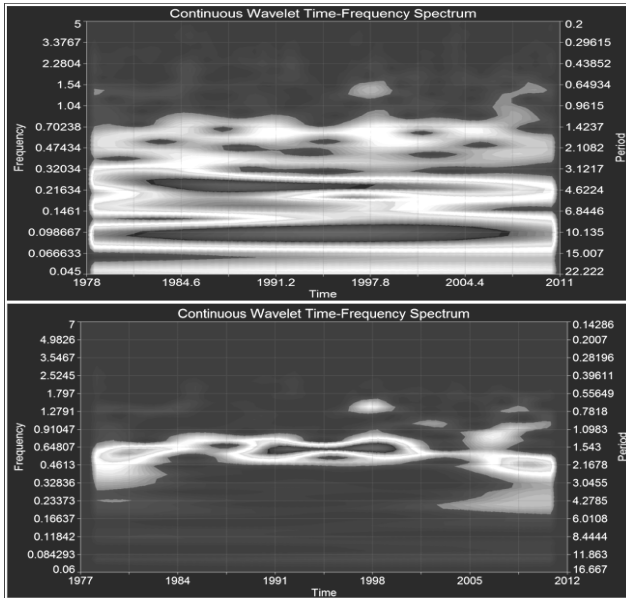

Figure 2: Wavelet spectra at a frequency of 14.5 GHz. The top graph represents the original series; the bottom one shows the short-periodic part, isolated by filtration (power spectrum)

Table 1: Table of periods for the radio source 3C120. Designations: Freq. – radio frequency; P_{max}, P_{min} – change interval period; T_{start}, T_{end} – time interval of existence period; PSD_{max}, T, PSD_{max} – maximum value of spectral power and its corresponding time; T, GWS_{max} – phase activity (the main is underlined).

3C 120, trend							
Freq.	P_{max}	P_{min}	T_{start}	T_{end}	PSD_{max}	T, PSD_{max}	T, GWS_{max}
14.5	4.6	3.8	1980.3	2008.5	195	1989.6	*1985.0*
	6.3	5.9	1979.0	1997.8	97	1989.2	1990.2
	10.1		1988.4	2009.9	198	1994.8	1998.0
8		4.3	1982.2	1996.5	230	1987.8	*1985.2*
		8.1	1990.4	2007.7	118	1991.1	1990.0
		12.4	1970.0	2005.0	1613	1979.0	1998.3
4.8		4.5	1983.3	1994.0	194	1988.4	*1986.0*
	10.0		1989.7	2009.2	401	1996.7	1989.3 2007.6
3C 120, O - C							
14.5	1.8	1.5	1979.3	1984.3	19	1980.8	1985.0
	1.6		1989.2	2000.7	29	1998.2	1992.0
	2.1		2005.5	2010.2	18	2008.7	*1998.2*
	0.8	0.7	1981.1	1985.1	3	1983.6	2003.7
	0.7		1996.3	1999.5	9	1997.8	2007.2
8	1.9	1.6	1978.7	2007.4	32	1979.5	1978.4
	3.4		1999.5	2008.4	43	2006.8	1985.1
	2.7	2.3	1979.1	1991.6	15	1980.1	1990.5
	4.1		1968.0	1974.8	19	1971.6	1999.8
	2.4		1970.8	1975.4	12	1973.4	2004.0
	1.2		1971.5	1975.7	8	1974.2	*2007.0*
4.8	3.3	2.7	1981.5	2006.5	10	1983.5	1981.6
	1.5	1.3	1988.7	1994.0	11	1991.2	1984.8
	1.6	1.3	1997.8	2007.2	4	1999.5	*1990.5*
	1.9	1.6	1998.7	2007.2	5	2001.4	1998.8 2002.1 2004.0

4. Forecasting changes in radio fluxes

Wavelet analysis showed the presence of cyclical component in the observed data. Thus, it made possible to build a parametric model (sine or damped sine wave) time series and predict the flux change outside of the available sample. For a number of components and their frequencies obtained from the spectral method (Scargle, 1982), we estimated the amplitude and phase of harmonics by the least squares method; the frequency, amplitude and phase were optimized by nonlinear approximation to the best values. The charts for original data (normalized) and the forecast are shown in Figure 3. The correlation coefficients and standard error of approximation are as follows: 0.90, 0.16 (14.5 GHz); 0.83, 0.41 (8 GHz); 0.94, 0.23 (4.8 GHz).
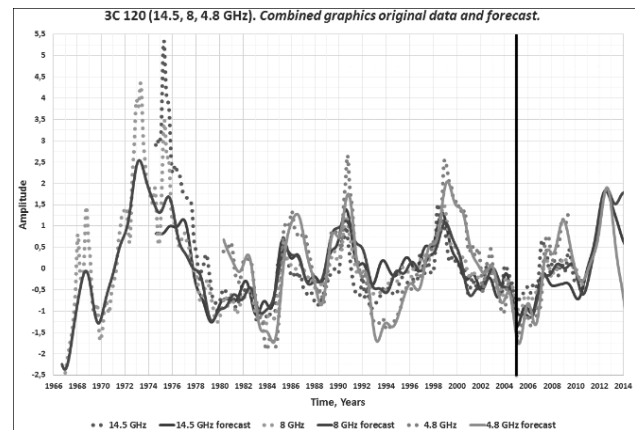

Figure 3: Charts of original data (indicated by dots) and parametric models (indicated by lines). The vertical line indicates the beginning of the forecast with 2005.2- 2014.0.

It is seen that after the beginning of the forecast, the coincidence with the original data deteriorates, but fortunately the forecast shows the total change in the data series. Perhaps, after 2010 there will be an increase in the flux of radio emission at three frequencies. This method of estimating the forecast time series is inferior in accuracy to modern methods based on neural networks, but it is much better in terms of speed of calculations for large data sets.

5. Time delays between the frequencies of observations

Between the data series, obtained at different frequencies, there are time delays. To determine their values, cross-correlation functions were computed. For frequency pairs 14.5-8, 14.5-4.8, 8-4.8 GHz the delay values were 51.1, 138.5, 58.4 days, respectively. However, the delay for the initial data contains the sum of oscillations with different periods. In the bands separate periods delay value varies with time. For example, in periods band ~6-4 years, change delay (in days) was: 146-292 (14.5-4.8 GHz); 36-146 (14.5-8 GHz); 18 – 109 (8-4.8 GHz). In periods band ~2-1 year, the delay value between frequencies decreases to the end of the series from 36 to 8 days. In periods band ~1.0-0.4 year the delay value ~22 days did not change with time (14.5-8 GHz).

6. Comparison of radio variability with VLBI maps

The observed activity in the radio source is the sum of contributions of radio-core and jet. In this paper, we attempt to relate changes in quasi-periodic radio flux with

the movement of bright spots in the jet (MOJAVE Program) (Lister et al., 2009). They were used to compare the phase activity at a frequency 14.5 GHz (1998.2, 2003.7, 2007.2) as the closest to 15.4 GHz (at this frequency VLBI maps were constructed). An example is shown in Figure 4. On the maps for 1998 high brightness of the nucleus and jet components is seen. The period values are 0.7 and 1.5 years for O-C data and 4.2, 10.0 years for trending periods. On the maps for 2003 in jet dominates one outlying from core low brightness component, the period for O-C data is 1.7 years. On maps for 2007 also dominated outlying component, and a new, near the core, periods for O-C data – 1.2 and 2.0 years. When spots in the jet bright, in O-C spectrum more short periods, with the distance from the nucleus brightness diminishes spots and increase the value of periods O-C component. High spectral power trending periods corresponds to high brightness of the core. Therefore, it is the most likely that the rapid variability of the radio emission forms a jet activity and long-term – core source. It should be noted that the VLBI «core» is not a base of jet. Certain patterns can be extended to the observation period when sessions VLBI measurements were not.
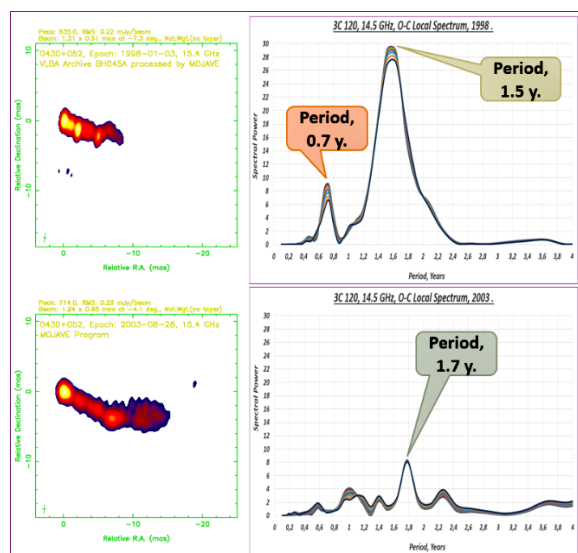

Figure 4: The figure shows VLBI maps to date 1998.01.03 (top) and 2003.08.28 (below) and the corresponding local wavelet spectra for the O – C data.

7. Results

The data processing based on wavelet analysis shows presence of some long-periodic (4-12 years) and short-periodic (0.7-3.4 years) components of the radio source. At a frequency 14.5 GHz periods of major fluctuations slightly decrease with time. For O-C components periods variation is 0.1-0.6 year. In short periods according to O-C data the highest spectral power was observed in the limited time at the moment of activation core and jet.

On the basis of quasi-periodic oscillations radio fluxes the forecast from 2005 to 2014 was calculated by means of parametric time series models. Up to ~2011 the forecast showed a good correspondence to real observation data, then an increase in flows at frequencies 14.5, 8, 4.8 GHz is likely to occur. The main phase of the radio source activity and form them «spectra periods».

Since the observed changes in flows composed of various sum of quasiperiodic processes were calculated the delay between the observing frequencies of not only the original series, but also in the bands of individual periods variability. The value varies with time delay and differs for different spectral bands.

Possible to assign from local wavelet power spectra of individual periods, which provide the main contribution to the phase of activity, allows us to «see» them with VLBI images of the coincidence of the observation time. Moving on jet bright components form fast quasiperiodic variations in the radio flux. Slow long-term flux changes, probably related to the activity of radio-core source. The advantage of long-term monitoring radio fluxes allows to use this relationship to a time when there was no regular VLBI observations (in catalog MOJAVE data from 1995). «Long waves» variable reflects macroscopic processes, changing accretion rate of gas shell to the core (Dibay, 1987), or instability in accretion disk. In paper (Cowperthwaite et al., 2012) they describe the possibility of destruction of the inner part of accretion disk in 3C120 before emissions of new components in the jet. Long-periodic variability may also be a result of the precession of the jet of radio source in presence of a double black hole (Caproni et al., 2004). The long period of 12.4 years, according to the data of optical monitoring of 3C120 may be explained by precession of the jet and coincides with the period value at a frequency 8 GHz (on 14.5 and 4.8 GHz similar values of long periods ~10 years).

Rapid variability of the radio flux can be explained by the shock waves moving in the jet. Interaction with superluminal jet component is manifested in form of forming a plurality of shock waves behind him (Marscher, 2008). A good description occurrence of short periods, model based on the magnetic dynamo (Meyer et al., 2002). In the radio source 3C120 some components of the jet close to the nucleus show a very small shift in a long time, which may be a result of «standing wave» in the interaction of forward and backward shock waves in the jet (Hiroki Nagakura et al., 2008).

References

Michel A.: 1988, *ASP Conf. Ser.*, **100**, 1423.
Lister et al.: 2013, *AJ,* **146**, 120.
Aller M.F. et al.: 2001, *BAAS*, **33**, 1516.
Gaydyshev I. *Data analysis and processing,* St. Petersburg, 2001.
Voskoboynikov Y. *Filtering of signals and images: Fourier and wavelet algorithms (with examples in Mathcad)*, Novosibirsk Architectural University, 2010.
Davidov A.V. *Digital processing of signals: Thematic lectures*, Yekaterinburg, 2007.
Smolentsev N. *Wavelet-analysis in MATLAB*. DMK-Press, 2010.
Astaf'eva N.M.: 1996, *UFN*, **166**, № 11.
Rosenberg G.S. et al. *Ecology Prediction*, Tolyatti, 1994.
Ryabov M.I. et al.: 2012, *Odessa Astron. Publ.*, **25/2**, 132.
Lister et al.: 2009, *AJ*, **137**, 3718.
Scargle J.: 1982, *AJ*, **263**, 835.
Dibay E.A., *Active nuclei and stellar cosmogony*, Moscow University Press, 1987, p. 6-19.
Cowperthwaite P.S. et al.: 2012, *arXiv:1205.3175v1*.
Caproni A. et al.: 2004, *Mon. Not. R. Astron. Soc.*, **349**, 1218.
Marscher A.P.: 2008, *ASP Conf. Ser.*, **386**.
Meyer F. et al.: 2002, *arXiv:astro-ph/0207573*.
Hiroki Nagakura et al.: 2008, *AJ,* **689**, 391.

ON THE ADVANTAGES OF PHOTOMETRIC OBSERVATIONS OF THE GEOSTATIONARY SATELLITES AT SMALL PHASE ANGLES

P. P. Sukhov [1], G. F. Karpenko [1], K. P. Sukhov [1], V. P. Epishev [2], I. I. Motrunych [2], I. Kudzej [3], P. A. Dubovsky [3]

[1] Astronomical Observatory, Odessa National University, Odessa, Ukraine, *psukhov@ukr.net*
[2] Laboratory of Space Research at Uzhgorod National University, Ukraine, *lkd.uzhgorod@gmail.com*
[3] Vihorlat Observatory, Humenne, Slovakia, *vihorlatobs1@stonline.sk*

ABSTRACT. As a rule, to determine photometric and dynamic characteristics of geostationary satellites required for their identification, long-lasting (from a half of the year to one year) photometric observations are needed at GSS different positions relative to the observer. The authors suggest conducting photometric measurements of GSS when they enter and exit the Earth's shadow near equinoxes. On these dates the GSS brightness increases by several magnitudes, so the use of telescopes with a mirror diameter of 50-70 cm can be effective. For shorter periods it is possible to get more information about the reflective properties of the object than during long-term observations at large phase angles. Several examples of photometric and dynamic characteristics of several GSS obtained near equinoxes are presented here.

Key words: multicolour photometry, geostationary satellite, satellite identification, phase angle, equinox, the Earth's shadow.

1. Introduction

The Geostationary Earth Orbit (GEO) is overcrowded with space objects (SO) and space debris. There are more than 20 groups of geostationary satellites (GSS) in the GEO that form a compact cluster of several satellites with inclination to the equator and eccentricity close to zero. When re-deploying and manoeuvring geostationary satellites, it is necessary to determine their nationalities, functionalities and types. The highly elliptical orbit (HEO) is poorly monitored. There is no information available for hundreds of objects in that orbit, or they are not reliably determined in catalogues.

In such cases, the SO identification by their orbital parameters is ineffective. This paper describes the advantages of photometric observations of the indicated SO at small phase angles. The SO brightness increases manifold when it enters and exits the Earth's shadow near equinoxes. At a certain time many GSS can be seen with the naked eye.

2. Theory

Simultaneous analysis of coordinate and photometric data allows to determine the object's type and its hardware platform, payload, dominant shape and behaviour in orbit (in normal mode and non-standard operation mode) within certain accuracy. It is possible to determine characteristics of the object's failure when it is out-of-order as it was done, for instance, for GSS "Yamal-1" [1], sample return mission "Phobos-Grunt" [2], "DSP F23" [3], "Cosmos 2397" [4], etc.

As a result of the change in geometrical configuration of the "Sun-Earth–GEO" system, the geostationary orbit usually passes outside the Earth's shadow cone throughout a year, except the interims near the vernal and autumnal equinoxes. The longest eclipses of GSS by the Earth's shadow occur on the days when the Sun is close to the vernal and autumnal equinoctial points. The polar regions of the Earth's shadow cross the GSS orbit before and after equinoxes, so duration of its stay in the Earth's shadow gradually shortens down to several minutes. The sunlight reflected off the GSS surface falls on the Earth's surface as a light spot of 350 km in diameter and slowly moves southward in spring and northward in autumn. For the GSS entry into the Earth's shadow two conditions must be met:

$$|\delta_s - \delta_t| < \rho_s, \quad \text{and} \quad |\alpha_s - \alpha_t| < r_t,$$

where δ_s, δ_t – inclination of the GSS orbit and the Earth's shadow axis, respectively; ρ_s – the diameter of the Earth's shadow cone; α_s, α_t – the right ascension of SO and the Earth's shadow axis, respectively; r_t – the length of the chord traversed by a satellite in the shadow.

$$\delta_t = -\delta_\odot, \quad \alpha_t = \alpha_\odot - 12^{\text{h}}$$

The most favourable period to record peak-amplitude flares depends on the observer's geographical position. This period lasts about 1.5 days. At around 45^0 N latitude the dates of GSS flares with maximum amplitudes near the equinoxes fall on the 3rd of March and the 12th of October [5].

Active GSS with orbital inclination and eccentricity close to zero get regularly eclipsed by the Earth's shadow during 22 days around the equinoxes. The duration of such GSS eclipses by the Earth's shadow depends on the observation date in relation to the equinox and varies from 10 minutes to 72 minutes. And the phase angles can vary from $13^0.6$ to $16^0.1$ at that [5].

The main photometric, optical, geometrical and dynamic characteristics of GSS, which are used to identify and interpret the SO behaviour in orbit, are as follows:

Photometric characteristics: the effective reflective area – $S\gamma_\lambda$; spectral reflectance γ_λ; phase coefficient β – change in magnitude if ψ fluctuates by 1^0; colour index (B-V, V-R, etc.); magnitude calculated at the phase angle $\psi = 0^0$ and reduced to a distance of 36,000 km.

Optical & geometrical characteristics: the SO linear dimensions and dominant shape.

Dynamic characteristics: the period of rotation around the centre of mass or one of axes; the SO orientation in space determined by the normal vector to the SO glinting surface (Xn, Yn, Zn – the vector's components).

Because of the applied character the satellite's characteristics, not all of them are available to the public. Each of these characteristics does not always unambiguously reply to the question which type an unknown SO belongs to. But the analysis of those characteristics along with orbital data, as well as additional and a priori information allows finding an acceptable solution to identify GSS.

To determine the GSS reflectance characteristics, continuous photometric observations are usually carried out during the whole night. The following problems can arise in the course of those observations:

1. Geostationary satellites are very faint with brightness of about 12^m-15^m at the phase angles $\psi > 30^o$. To photometrical such GSS, it is necessary to use telescopes with primary mirror diameter of approximately 1 m and larger.

2. When conducting simultaneous basic observations with reference distance of hundreds or thousands of kilometres at $\psi > 30^o$, each observer can see the SO at a different angle. It is not quite correct to compare or combine the light curves obtained at different observation sites to interpret the SO behaviour over time in the orbit at a certain moment of observation. Simultaneous basic observations also often restricted by weather conditions at the observation sites.

The experience gained by the authors of this paper shows that the photometry of GSS at small phase angles near equinoxes considerably saves time required to obtain the GSS characteristics and allows to improve the content and quality of the target information. The GSS brightness can increase by 10^m during these days, so it can be effective to use telescopes with a mirror diameter of 50-70 cm in diameter. The analysis of light curves at small ψ for objects with diffuse and specular components also enables to obtain more reliable reflectance characteristics of the satellite's surface.

The observed magnitude m of a satellite depends mainly on three parameters: the reflective area GSS – S, reflectance characteristics his surface - γ_λ, and the phase angle – ψ.

$$m = F\{\psi, S\gamma_\lambda\}.$$

It is possible to determine m from the observation data and calculate the phase angle ψ. The computation of the spectral reflectance – γ_λ and apparent effective reflective area – S is quite probabilistic and depends on many reasons listed below.

The GSS brightness in terms of magnitude is calculated by famous Pogson's formula: $m_\lambda = -2.5lg\ E_1/E_2$. As per McCue et al. [6], the GSS brightness in the target wavelength range can be expressed as the following formula:

$$m_\lambda = m_\lambda^c - 2.5\lg\left[\frac{S\gamma_\lambda F(\psi)}{d^2}\right]. \qquad (1)$$

where m_λ^c – the Sun's magnitude in the wavelength range, S – the area of the GSS surface illuminated by the Sun and thus visible to an observer, γ_λ – spectral reflectance, $S\gamma_\lambda$ – effective reflective area, ψ – satellite-centric phase angle, $F(\psi)$ – phase function, d – topocentric distance to the object. The Moon's illumination, light reflection and scattering by the Earth are left out of formula (1). At an altitude of 36,000 km the interference of the Earth's background illumination, including absorption and Rayleigh scattering, is negligible and makes up hundredths of magnitude [7, 8]. The Moon's background illumination can be neglected as the GSS photometry is feasible at large angular distances to the Moon and at small lunar phases.

The shape of the GSS light curve on its entering (exiting) the Earth's shadow is primarily related to the effective reflective area $S\gamma_\lambda$. Its value depends on the optical characteristics of the SO surface, under-satellite point longitude, satellite's orientation, geographical position of an observer, season and the satellite's orbit life (ageing of the materials used in the satellite's construction), etc.

At small phase angles ($cos\ \psi \approx 1$) when the reflective area is maximum, values $S\gamma_\lambda$ and γ_λ for objects of known dimensions can be calculated using the observation data. As follows from formula (1):

$$S\gamma_\lambda = d^2 \cdot 10^{\frac{m_\lambda^\ominus - m_\lambda}{2.512}} \cdot \sec\psi.$$

The value γ_λ is determined in a similar manner:

$$\gamma_\lambda = \frac{d^2}{S} 10^{\frac{m_\lambda^\ominus - m_\lambda}{2.5}}.$$

Thus, with known GSS dimensions, it is possible to determine its near-real effective reflective area – $S\gamma_\lambda$ and spectral reflectance γ_λ. With known dominant geometric configuration, it is possible to use corresponding scattering phase functions, particularly for sphere, cylinder, plate, etc.

The phase function of a satellite, except spherical one, assumes that its space orientation is known. The satellite's orientation in space is determined by the normal vector to the visible part of the SO surface that generates a flare at the time of observation in the satellite-centric coordinate system. The normal vector components are Xn, Yn and Zn. The X-axis is parallel to the celestial equator and oriented to the vernal equinox point. The Y-axis is oriented to the Earth's centre. The Z-axis is oriented to the celestial pole parallely to the Earth's rotational axis. The satellite identification by the photometric observations can be conducted in two ways.

<u>Direct problem.</u> The apparent brightness of an object at any specific time is computed and further analysed by the GSS estimated (known) shape, lighting conditions and optical properties of its surface, as well as by known SO orientation relative to an observer. This problem is practically solvable with rather high probability.

<u>Reverse problem.</u> In this case the non-uniqueness in determination of the SO shape by its light curve is associated with the following fundamental principle. The algorithm input is a function dependent on a single argument as phase angel - brightness (or m (t)). In mathematics such a problem is classified as incorrect, and the obtained solutions are generally unstable or have no physical meaning.

However, the problem can be simplified if the object's dominant shape is known. The phase curve of the defined shape of the object is described by the scattering function $F(\psi)$ for basic geometrical figures (plate, cylinder, sphere, etc.). They are analytically determined in the studies by E.R.Lanczi, W.R.Rambauske, G.A.McCue, J.G.Williams, J.M.Morford [6, 9, 10]. The GSS orientation in space can be determined by mirror flares using the method described by V.Epishev in [11].

3. Results

The computation of some photometric and dynamic characteristics of several GSS at small ψ was preformed.

About 50 multicolour light curves in B, V, R filters (Johnson's system) for the GSS "Intelsat 10-02" entering and exiting the Earth's shadow have been obtained in Odessa Astronomical Observatory (Ukraine) and Vihorlat Observatory (Slovakia) during 2005-2014. A photomultiplier FEU-79 operated in the photon-counting mode was used to measure the satellites' brightness. The in-depth study of the mentioned GSS behaviour in orbit on the basis of multicolour observations is reported in [12].

"Intelsat 10-02" is based on the *"Eurostar 3000"* platform; its solar panel (SP) span is 45 metres. The GSS light curves is best approximated by the phase functions for a flat plate with Lambertian reflectance, which takes the form:

$$F(\psi) = cos\ \varepsilon \cdot cos\ \theta),$$

where ε and θ correspond to the angles of incidence and reflection of the light to plane of the SP, respectively.

The "short" light curve (obtained with 50-cm telescope in Odessa, Ukraine) is shown in Figure 1a; and the "long" light curve (obtained with 1-m telescope in Humenne, Slovakia) is presented in Figure 1b.
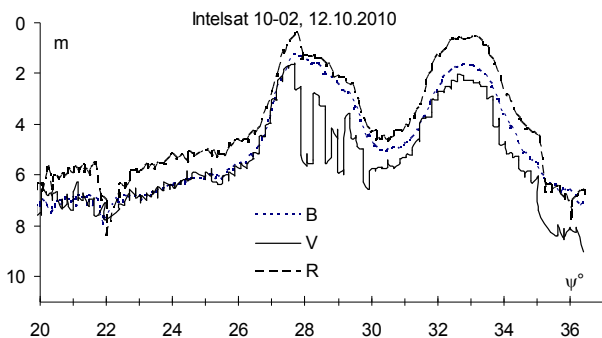

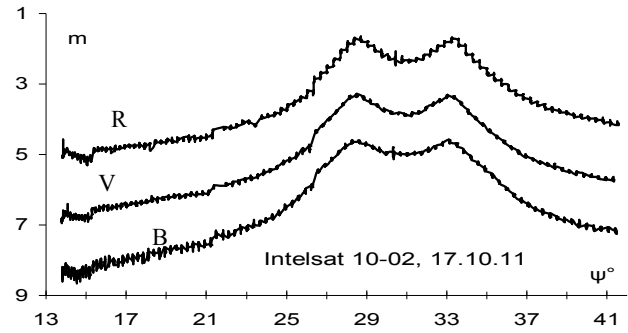Figure 1a: Odessa – "Short" phase light curve at the time of exit from the Earth's shadow

Figure 1b: Slovakia – "Long" phase light curve at the time of exit from the Earth's shadow

In the opinion of the authors of [12], the presence of two brightness peaks on the light curve is attributed to the contribution in the total quasi-mirror reflected light of the first panel SP, and then by that of the second panel SP. The brightness decrease between the two peaks can be explained by the movement of the solar image on the payload platform. The analysis of the data presented in Table 1 reports that the SO functioned normally during the periods of observations.

Table 1: The results of the solar panels' orientation determination at the time of the GSS peak brightness

Observation date	UT	$\alpha_{\odot}$, °	$\delta_{\odot}$, °	α_{obs}, °	δ_{obs}, °	α_n, °	δ_n, °
06.10.2010	$1^h43^m54^s$	191.56	-5.02	216.37	6.82	204.01	0.92
	$2^h08^m13^s$	191.71	-5.03	222.44	6.82	207.05	0.92
07.10.2010	$1^h43^m22^s$	192.48	-5.40	217.21	6.82	204.89	0.72
	$2^h06^m00^s$	192.62	-5.40	222.81	6.82	207.72	0.72
12.10.2010	$1^h37^m55^s$	197.05	-7.30	220.76	6.82	208.97	-0.23
	$2^h02^m24^s$	197.20	-7.31	226.88	6.82	212.03	-0.23
14.10.2010	$1^h59^m58^s$	199.05	-8.05	228.28	6.82	213.68	-0.63

The first two columns of the Table are clear. The following data are presented in the next columns: satellite-centric equatorial coordinates of the Sun ($\alpha_{\odot}$, $\delta_{\odot}$), observer (α_{obs}, δ_{obs}) and normal orientation towards the solar panel (α_n, δ_n). All angles are measured in degrees.

Values γ_λ and $(S\gamma_\lambda)$ reduced to a distance of 36,000 km and $\psi = 0°$ for "Intelsat 10-02" are given in Table 2; the values were computed by the "short" light curve with the variation range $\psi \approx 13°$ and by the "long" light curve with the variation range $\psi \approx 28°$ (marked with symbol *).

Table 2: The $(S\gamma_\lambda)$, and spectral reflection coefficient γ_λ, computed by the "short" and "long" light curves

Sp	γ_λ ±0.02	$^*\gamma_\lambda$ ±0.02	$(S\gamma_\lambda)$, m^2 ±1.0	$^*(S\gamma_\lambda)$, m^2 ±0.60
B	0.18	0.18	17.58	16.25
V	0.34	0.38	32.44	34.11
R	0.22	0.21	20.26	19.15

As is seen, the values γ_λ and $(S\gamma_\lambda)$ computed by the "short" and "long" light curves are similar.

The values $S\gamma_\lambda$ and γ_λ for GSS of two types with *"Euro-star 3000S"* ("Skynet-5B", "Skynet-5A", "Skynet-5D") and *"GeoBus"* ("Sicral-1" and "Sicral-1B") platforms were computed by the "short" light curves in a similar way (see Table 3). There were at least three light curves obtained for each object on its entry and exit from the Earth's shadow.

Table 3: The effective reflective area $S\gamma_\lambda$ and spectral reflectance γ_λ for GSS with platforms of different types computed by the "short" light curves

Platform types	SP	γ_λ	$S\gamma_\lambda$, m^2, $\psi = 0°$
Eurostar 3000	B	0.18 ±0.02	17.58 ± 1.00
	V	0.34 ±0.02	32.44 ± 1.00
	R	0.22 ±0.02	20.26 ± 1.00
Eurostar 3000S	B	0.14 ± 0.02	11.86 ± 0.50
	V	0.11 ± 0.02	9.74 ± 0.50
	R	0.12 ± 0.02	10.80 ± 0.50
GeoBus (Italsat-3000)	B	0.12 ± 0.05	5.41 ± 1.60
	V	0.12 ± 0.05	5.17 ± 1.60
	R	0.14 ± 0.05	6.22 ± 1.60

The "short" phase light curves for GSS of two types, "Sky-net-5B" and "Sicral-1B" are shown in Figures 2a and 2b.
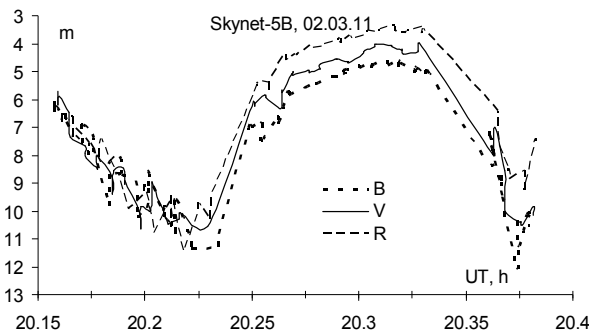
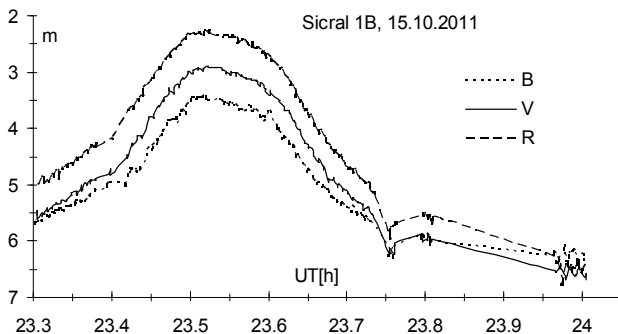Figure 2a: The "short" phase light curve after satellite's exit from the shadow

Figure 2b: The "short" phase light curve after satellite's exit from the shadow

The Table 3 shows; the values $S\gamma_\lambda$ and γ_λ for the "Skynet" (with "Eurostar 3000S platform) and «Sicral» (GeoBus Italsat-3000) military satellites are several times less than those for communication satellites with "Euro-star 3000" platform; that corresponds to reality.

Three light curves at small ψ were obtained for the emergency GSS *"Cosmos 2397"*. The most meaningful phase light curve with diffuse and specular components for that SO after its exit from the Earth's shadow is given in Figure 3. The presence of four peaks in Figure 3b appears to indicate the presence of four segments of SP. The solar panels rotate with maximum speed of one rotation per 18 minutes. At the time of the first flare the solar panels' tilt towards the Sun was 6.5 degrees, and at the time of the second flare – 8.7°. The minimum inclination of the panels towards the Sun was ~5.0°. That is classical inclination of the active GSS solar panels towards the Sun. The solar panels' orientation remains unaltered relative to the Sun, although the satellite slowly drifts along the orbit (~1° per day). The components of unit normal vector to the SP surface in the light curve segment corresponding to the second peak in brightness at ψ from 19.13° to 23.65° are given in Table 4. As can be seen from Table 4, the Yn component is practically oriented to the observer. The SP orientation by two mirror flares in Figure 3a demonstrates that they were moving practically in the ecliptic plane. Thus, the normal orientation for the first flare was a = 176.96°, δ = 4.94°, and for the second flare a = 179.22°, δ = 4.96°.
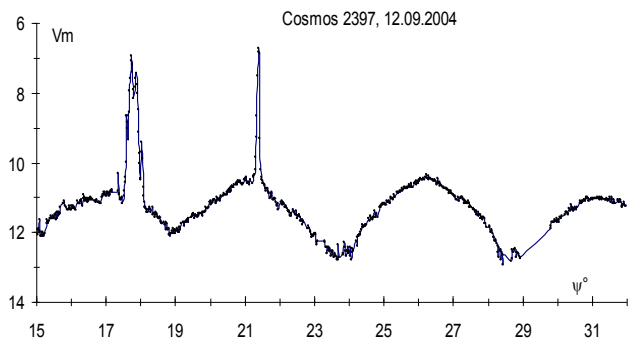

Figure 3a: The phase light curve after satellite's exit from the shadow
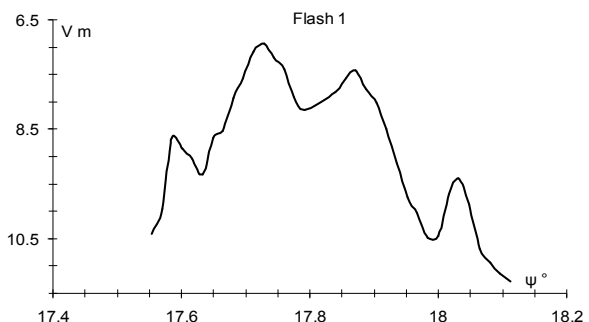

Figure 3b: A segment of the first flare

Table 4: The normal vector orientation towards SP related to the observer at the phase angles from $19^o.13$ to $23^o.65$ as of 12.09.2004.

Ψ °	Xn	Yn	Zn
19.130	0.023	0.994	-0.104
20.196	0.013	0.995	-0.096
21.044	0.004	0.996	-0.090
21.413	0.001	0.996	-0.088
21.766	-0.003	0.996	-0.086
22.855	-0.014	0.997	-0.081
23.652	-0.021	0.997	-0.077

With $\Psi°$ – the satellite-centric phase angle; Xn, Yn, Zn – components of the normal vector to the reflective surface. The effective reflective area for the solar panels at the given SO angle for the time of the first flare (see Figure 3b) were computed: $S\gamma_1 = 0.87$ m^2, $S\gamma_2 = 4.18$ m^2, $S\gamma_3 = 2.67$ m^2, $S\gamma_4 = 0.66$ m^2, where $S\gamma_i$ – the number of the panel, for which the effective reflective area were determined.

Possible cause of non-standard operation mode. The period of the object's rotation around the Z component is 18 minutes whilst making a cone with an angle close to 5° and causing a change in the measured brightness (mainly reflected off the solar panels) with amplitude of about 2.0^m. The most likely is that the GSS stabilization is upset, and that resulted in its rotation around the axis with orientation close to that one of the Z-axis [4].

On the basis of the photometric observations, the authors of study [3] identified the breakdown of satellite *"DSP F23".* "The analysis of the light curves and behaviour of the normal orientation to the specular reflecting elements, first of all to Zn, indicates that the satellite practically maintains its orientation to the Earth's centre, but there is no spin around that axis with a period close to 10 seconds. That resulted in inability to scan the Earth's surface that was the main purpose of the SO and caused its change-over to the librational mode".

4. Advantages and Conclusions

In the authors' opinion, the main advantages of the GSS photometry the near equinoxes are the following:

1. It is possible to get a few tens of light curves enter and out from of the Earth's shadow during the night.

2. It is possible to determine almost all reflectance and dynamic characteristics, except the phase coefficient *β*.

3. More reliable photometric and dynamic data for objects of known dimensions can be computed.

4. The GSS behaviour in orbit, either in normal mode or non-standard operation mode, can be estimated by its mirror flares.

5. It is possible to considerably save time to obtain data characteristics of GSS, which are necessary to identify an unknown GSS.

The photometric database (Johnson's system) of the Astronomical Observatory of I.I.Mechnikov Odessa National University includes about 500 light curves for more than 100 GSS of different types: "Intelsat", "DSP", "SBIRS", "Eutelsat", "Mentor", "Express", "Skynet","Yamal","Sicral", "Mercury", "PAN", etc.

References

Bagrov A.V., Vygon V.G., Rykhlova L.V., Shargorodskiy V.D.: 2000, in: *The Near-Earth Astronomy and Issues in the Study of Small Solar System Bodies* (in Russian). M.: Kosmosinform, 276 p.

Yepishev V.P., Barna I.V., Bilinskiy A.I., Koshkin N.I., Kudak V.I., Lopachenko V.N., Martynyuk-Lototskiy K.P., Motrunich I.I., Naybauer I.F., Rykhal'skiy V.V.: 2013, in *International Scientific Conference the Near-Earth Astronomy* (in Russian), Krasnodar, Kuban State Univ. Press, 129.

Didenko A.V., Usol'tseva L.A.: 2010, in *Proc. of the National Academy of Sciences of the Republic of Kazakhstan. The Physical and Mathematical Series* (in Russian), **No. 4**, 81.

Sukhov P.P., Movchan A.I., Kochkin N.I., Korniychuk L.V., Strakhova S.L., Epishev V.P.: 2004, *Odessa Astron. Publ.*, **17**, 99.

Karpenko G.F., Murnikov Б.А., Sukhov P.P.: 2009/2010, *Odessa Astron. Publ.,* **22,** 25.

McCue G.A., Williams J.G., Morford J.M.: 1971, *Planet. and Space. Sci*., **19**, 851.

Severnyy S.A., Smirnov M.A., Bagrov A.V.: 1986, *Scientific Inform. of the Astr. Council of the Academy of Sciences of USSR*, (in Russian), **58,** 103.

Smirnov M.A.: 1994, *Photometric Observations of Artificial Celestial Bodies*. Thesis of the Doctor of Phys. and Mathemat. Sci., Institute of Astronomy of the Academy of Sciences of Russian Federation (in Russian), 164 pp.

Lanczi E.R.: 1966, *J. Opt. Soc. Am.*, **56**, 873.

Rambauske W.R., Gruenzel R.R.: 1965, *J. Opt. Soc. Am.,* 1965, **55**, 315.

Yepishev V.P.: 1983, *Astrometry and Astrophysics*, Academy of Sci. of USSR (in Russain), 89.

Sukhov P.P, Karpenko G.F., Epishev V.P., Motrunych I.I.: 2009/2010, *Odessa Astron. Publ.*, **22,** 55.

METHOD FOR CALCULATING ORBITS OF NEAR–EARTH ASTEROIDS OBSERVED WITH TELESCOPE OMT-800

V.V.Troianskyi [1], A.A.Bazyey [2], V.I.Kashuba [3], V.V.Zhukov [4], S.A.Korzhavin [5]

Astronomical Observatory, Odesa National University
Shevchenko Park, 65014, Odesa, Ukraine
[1] v.troyanskyi@onu.edu.ua, [2] o.bazyey@onu.edu.ua, [3] v.kashuba@onu.edu.ua,
[4] v.zhukov@onu.edu.ua, [5] s.korzhavin@onu.edu.ua

ABSTRACT. One of the frame processing techniques, as well as an example of further use of the obtained results to calculate an asteroid's orbit are given in the present paper. The application of frame combination method to improve the telescope's limiting magnitude is described.

Key words: orbits, asteroids.

1. Introduction

Since a new telescope OMT-800 (0.8 m primary mirror, f/2.67 reflector with corrector + CCD) was installed at the observation station of the Astronomical Observatory of Odesa National University in Mayaki village, it became possible to obtain high-precision differential astrometric observations of geostationary objects, asteroids and comets with total magnitude brighter than 21.

The telescope's design features and capabilities are described in detail in the article by Andrievsky et al. (2013).

So far the positional observations of faint objects in the Solar System are of great importance as the ground-based support of space observations of these objects, as well as search and registration of space debris are required indeed.

2. Method for surveying and software for frame processing

It is not feasible to use long exposures for OMT-800 as due to its significant light-gathering power faint objects are overshone by the stellar background for exposures of longer than 30 sec. The optimum exposure of 10-20 sec (depending on the Moon's presence and atmospheric conditions) was experimentally chosen. Observations of faint objects are conducted by series of 5-15 consecutive exposures. A single observation results in a monochrome 16-bit 3056 x 3056 pixels image saved as FITS-file. A typical example of such image is shown in Fig. 1.

To increase the limiting magnitude for the observed objects, as well as to carry out astrometric reduction of images and obtain differential equatorial coordinates of the observed objects, we used OLDAS programme module, which is a component of CoLiTec software package (Savanevich et al., 2012), provided by courtesy of
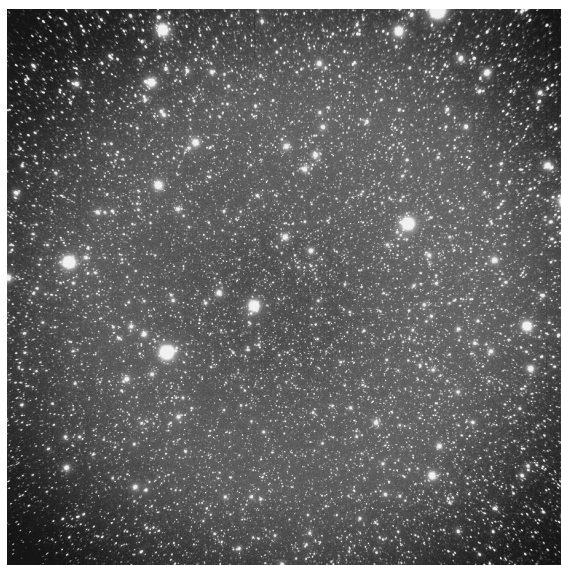

Figure 1: A frame before processing. The exposure time is 10 sec.

its developers. The indicated module enables to adjust frames of any size by brightness using median filter and the Fourier analysis, as well as to conduct auto-calibration and correction by eliminating dead and hot pixels. At this stage the vignetting of field of view, comatic aberration, any possible failures of daily tracking; ambient light which interferes with telescope viewing, as well as diffracted rays can be corrected. A typical result of a single frame processing using the mentioned software package is presented in Fig. 2. The frame shown in Fig. 1 is taken as the initial frame.

Application of the frame combination functional implemented in the CoLiTec software package enabled us to increase the telescope's limiting magnitude from 19 to 21, which is shown in Fig. 2 and Fig. 3.

A super-frame obtained by combining eight frames with 10 sec exposure is demonstrated in Fig. 3.

Experimental test of a number of observational techniques showed that at least three series of eight frames in each should be recorded to receive the best quality astrometric observations. Combination of eight frames allows of

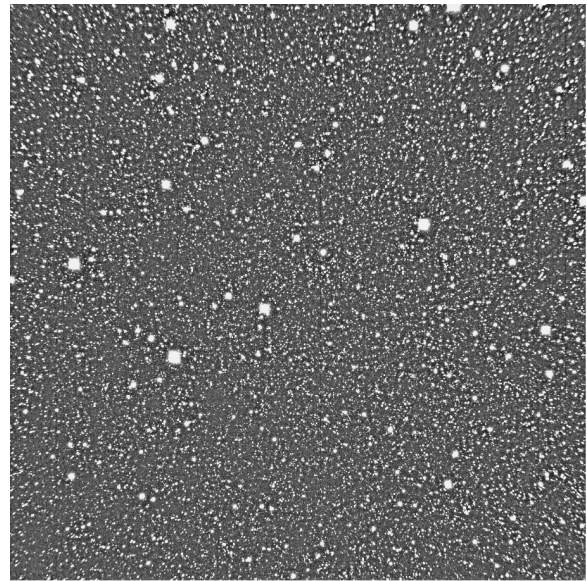Figure 2: A frame after processing. The exposure time is 10 sec.

Figure 3: A super-frame made up of 8 individual frames with exposure time of 10 sec.

obtaining good signal-to-noise ratio while three super-frames are required to determine the target object's orbit.

Having got super-frames made up with OLDAS programme, we automatically search for known asteroids, as well as for new ones, in the frame. Such capability increases the value of this programme which can be applied for object search and sky survey.

3. Angular surveying reports and computation of asteroid orbits

The frame processing technique is still to be approved, but the first results have been already received. 90% of our reports on observations and results of primary processing for asteroids and comets (Williams et al., 2014) with magnitude up to 21 meet the Minor Planet Centre Orbit (MPCORB) database (www.minorplanet center.net) requirements.

The Keplerian elements of an asteroid are computed using the Gauss method by three observed positions (Montenbruck et al., 2002).

In questionable cases the fourth observation can be used to choose the correct orbit from several alternative solutions.

Orbital elements of an asteroid are refined using all observations by the method of differential correction of orbits (Bazyey et al., 2005).

4. Conclusion

The refined orbital elements are concordant with the corresponding asteroid's orbital elements from the Minor Planet Centre Orbit (MPCORB) database.

Our results of asteroid observations' processing will be further improved by advancing the algorithm of frame processing technique, upgrading OMT-800 and extension of computational method for orbit calculations. That in turn will enable to use the obtained orbital state vectors to solve the asteroid ephemerides problem (Bazyey et al., 2009).

References

Andrievsky S.M., Molotov I.E., Fashchevsky N.N., Podlesnyak S.V., Zhukov V.V., Kouprianov V.V., Kashuba S.G., Kashuba V.I., Mel'nichenko V.F., Gorbanev Yu.M.: 2013, *Odessa Astron. Publ.*, **26/1**, 6.

Savanevich V., Bryukhovetskiy A., Kozhuhov A., Dickov E., Vlasenko V.: 2012, *Space Science and Technology*, **18**, 39.

Williams G. et al.: 2014, *Minor Planet Circ. Suppl.*, 544817-545650, 545651-547654, 558681-560008.

Williams G. et al.: 2014, *Minor Planet Electronic Circ.*, 2014-Y44.

Montenbruck O., Pfleger T.: 2012, *Astronomy on the Personal Computer*.

Bazyey O.A., Sibiryakova E.S., Shulga A.V.: 2005, *Odessa Astron. Publ.*, **18**, 8.

Bazyey A.A., Kara I.V.: 2009, *Visnyk Astronomichnoyi shkoly,* **6/2**, 155 (in Ukrainian).

RE-CLASSIFICATION OF THE NEGLECTED VARIABLE V480 AQL

N.A. Virnina[1], N. Maslova[2], T. Krajci[3]

[1] Odessa National Maritime University, Mechnikova str., 34, 65029, Odessa, Ukraine,
virnina@gmail.com

[2] Mariinskaya High School, L. Tolstogo str., 9, 65023, Odessa, Ukraine

[3] Astrokolkhoz Observatory, Center for Backyard Astrophysics, New Mexico,
PO Box 1351 Cloudcroft, NM 83117, USA

ABSTRACT. We present the results of multi-coloured photometric study of previously neglected variable star V480 Aql. Our VRI observations prove that this star belongs to classical Cepheids with the period of $P = 19^d.0016$. We also propose an empirical dependence between colour indices and temperature of supergiants, which, according to the nature of Cepheids, enabled us to determine minimum and maximum temperatures of V480 Aql.

Key words: Stars: variable: Cepheids; stars: individual: V480 Aql.

1. Introduction

V480 Aql = GSC 0460-0382 ($R.A._{J2000} = 18^h50^m34.885^s$, $Dec._{J2000} = +07°07'33.70''$) is a poorly studied variable star, discovered by C. Hoffmeister (1949) who classified it as a typical RW Aurigae variable. Then this star was mentioned in the list of coordinates and identifications for Sonneberg variables (Kinnunen & Skiff, 2000). But no photometric data have been published up till now. At present different types of variability are indicated for V480 Aql in various catalogues: Hoffman, Harrison and McNamara (2009) classified it as a rapid irregular variable; the variability type LB is indicated in GCVS (Kazarovets et al., 2013); in ASAS (Pojmanski, 2002) it is classified as a star of DCEP-FU type; and in AAVSO catalogue the variability type DCEP is indicated.

In order to clarify the classification of V480 Aql, we observed it in V, R and I bands.

2. Observations

We observed V480 Aql using two telescopes for over two years. One of them, BSM Takahashi FS-60CB, equipped with SBIG ST-8XME camera and photometric B, V, R_c, I_c filters, we used from February till May 2012. Another one, namely T5 Takahashi Epsilon ($D = 250mm$) of iTelescope.net observatory in New Mexico, USA, was used from July 2013 till June 2014. It was equipped with SBIG ST-10XME together with BVR or BVI photometric filters. As V480 Aql is rather faint in B-band, we observed it only with V, R and I filters for this study. Three constant stars were chosen as reference stars for ensemble photometry. The list of reference stars, their coordinates and magnitudes are given in Table 1. The BSM telescope was designed for rather bright stars; thus the photometric data, collected with that telescope, demonstrate a wide scattering. To improve the quality of phase curves, we binned the BSM data with bin size of 0.1 d. We applied the Lafler-Kinman method to combined light curves and determined the period $P = 19^d.0016(\pm 0^d.0851)$, which is in good agreement with the AAVSO period $P = 19^d.001597$. The initial epoch is $HJD_{\max} = 2456608.01 \pm 0.19$. The resulting curves from both telescopes in $V-$, $R-$ and $I-$bands are shown in Fig. 1. The amplitudes and phase curves are typical for classical Cepheids.

3. Classification

Multicoloured observations made it possible to evaluate the temperature variations of V480 Aql by analysing colour indices. Taking into account that V480 Aql is faint in B-band and rather bright in I-band, and assuming that this star is a supergiant that is typical for Cepheids, we used the dependence between colour indices $(V-R)$ and $(R-I)$ and temperature T, given in Allen's Astrophysical Quantities (Cox, 2000). We propose two empirical formulae, whose domain of validity extends from $2800K$ to $10000K$:

$$lg(T) = (-0.56 \pm 0.01) \cdot lg(V-R+0.2) + (3.654 \pm 0.003);$$

$$lg(T) = (-0.50 \pm 0.02) \cdot lg(R-I+0.1) + (3.573 \pm 0.009).$$

Table 1: Reference stars

USNO-B1.0	R.A.	Dec.	V	R	I
0971-0471757	$18^h51^m32.645^s$	$07°08'15.73''$	$11^m.279$	$10^m.797$	$10^m.347$
0972-0471843	$18^h50^m03.570^s$	$07°13'17.15''$	$11^m.591$	$10^m.750$	$9^m.970$
0971-0469055	$18^h49^m31.477^s$	$07°08'01.45''$	$11^m.033$	$10^m.481$	$9^m.967$
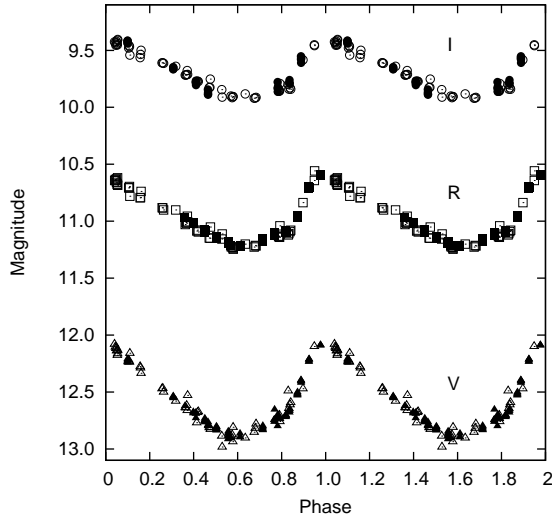
Figure 1: VRI phase curves of V480 Aql. Filled symbols correspond to T5 observations, while empty ones correspond to BSM data

Figure 2: $(V\text{-}R)^0$ and temperature variations of V480 Aql.

We found that V480 Aql belongs to the Galactic thin disc; thus, to determine the real temperature we should take reddening into account. To calculate the intrinsic $(B - V)^0$, we adopted the empiric formula suggested by Tammann, Sandage and Reindl (2003):

$$(B - V)^0 = (0.366 \pm 0.015) \cdot lgP + (0.361 \pm 0.013).$$

By applying it to V480 Aql, we obtained the mean value $(B - V)^0 = 0^m.829$. To find the following dependence between colour indices: $(V - R) = 0.504 \cdot (B - V) + 0.085$, we also analysed the results of processing the photometric data given by Fouque et al. (2007) Thus, for V480 Aql the expected mean colour index is $(V - R)^0 = 0^m.503$. Adopting this value, we calculated the $V - R$ variability, which gave the minimum and maximum temperatures for V480 Aql: $(V - R)_{max} = 0^m.382(9)$ yields $T_{max} = 6120(\pm64)K$, $(V - R)_{min} = 0^m.573(5)$ corresponds to $T_{min} = 5216(\pm18)K$ (Fig. 2). The maximal temperature is reached near the phase $\varphi = 0$, together with maximal luminosity, which is typical for DCEP-type variables.

4. Conclusion

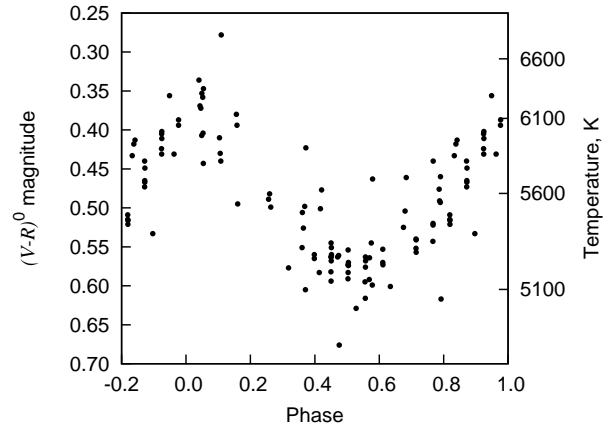Due to the fact that the period, shape, phase curve amplitudes, temperature variation and position in the Galaxy are typical for those ones of DCEP-type variables, we may conclude that V480 Aql is a classical Cepheid indeed.

References

Cox A.N.: Allen's Astrophysical Quantities, Athlone Press, London, UK, 4th ed. 2000, 721 p.

Fouque P., Arriagada P., Storm J. et al.: 2007, *A&A*, **476**, 73.

Hoffman D.I.; Harrison T.E.; McNamara B.J.: 2009, *Astron. J.*, **138**, 466.

Hoffmeister C.: 1949, *Astron. Nach.*, **278**, 24.

Kazarovets E.V., Samus N.N., Durlevich O.V. et al: 2013, *IBVS*, **6052**, 1.

Kinnunen T., Skiff B.A.: 2000, *IBVS*, **4864**, 1.

Lafler J., and Kinman T.D.: 1965, *ApJ. Suppl.*, **11**, 216.

Pojmanski G.: 2002, *Acta Astron.*, **52**, 397.

Tammann G.A., Sandage A., Reindl B.: 2003, *A&A*, **404**, 423.

Watson C.L.: 2006, *SASS*, **25**, 47.